Ioannis N. Remediakis

First-Principles Studies of Solid Surfaces

Pure and C-alloyed Si(100) and NO chemisorption on $MoO_3(010)$

A Dissertation
submitted to the Physics Department, University of Crete
in partial fulfillment of the requirements for the Degree of
Doctor of Philosophy in Physics

Heraklion, Greece, 2002

First-Principles Studies of Solid Surfaces:
Pure and C-alloyed Si(100) and NO chemisorption on $MoO_3(010)$

Thesis author:	Ioannis N. Remediakis
Thesis supervisors:	Prof. Efthimios Kaxiras Prof. Pantelis C. Kelires
Thesis committee:	P. C. Kelires E. Kaxiras E. N. Economou N. Papanikolaou S. Anastasiadis P. Tzanetakis N. Flitzanis

Physics Department, University of Crete
Heraklion, Greece

January 2002

Thesis Abstract

The present Dissertation deals with modeling of representative solid surfaces and surface processes using first-principles methods.

We first present a generalization of Density Functional Theory (DFT) to include excited states, as the original formulation is based on ground-state properties of the electron gas. This allows us to give a detailed review of DFT, which is used throughout the Thesis for exploring properties of the surfaces, and to demonstrate a simple but efficient method for calculating band gaps of semiconductors.

The first surface under consideration is Si(100), a simple system of enormous technological interest. Our study includes detailed analysis of the chemical bonding, energetics and electronic structure; this system is used as a framework to present in detail theoretical tools used in studies of surface phenomena, the most important among them being simulation of Scanning Tunneling Microscope (STM), which allows direct comparison to experimental observations.

We next study C-alloyed Si(100), a surface used in many cases as an initial stage for growth of complicated structures, such as SiGe quantum dots and B-doped SiGe superlattices, used in various microelectronic applications. For the case of low C content, we reveal for the first time an impressive long-range order in the C distribution, a prediction that has not yet been tested experimentally. For high C content of the system, we find the structures that can account for the observed STM images, and discuss their nature.

The Dissertation concludes by a study related to catalysis. We study various geometries of NO adsorption on $MoO_3(010)$, a widely used surface for the catalytic reduction of NO. We propose that the reduction is a non-dissociative process, and that it happens through formation of a dinitrosyl ($(NO)_2$) on an exposed Mo atom of the surface.

Περίληψη Εργασίας

Στην παρούσα Διατριβή μελετάμε αντιπροσωπευτικές επιφάνειες στερεών και επιφανειακές διεργασίες, έχοντας ως αφετηρία μεθόδους Πρώτων Αρχών.

Κατ'αρχάς παρουσιάζουμε μια γενίκευση της Θεωρίας του Συναρτησιακού της Πυκνότητας (Density Functional Theory, DFT) η οποία περιλαμβάνει και διεγερμένες καταστάσεις, μια που η αρχική θεμελίωση της Θεωρίας περιελάμβανε μόνο ιδιότητες σχετικές με τη θεμελιώδη κατάσταση του ηλεκτρονικού αερίου. Με την ευκαιρία αυτή, δίνουμε μια σύντομη ανασκόπηση της DFT, η οποία χρησιμοποιείται ευρέως σε όλη την Διατριβή για τη μελέτη των ιδιοτήτων των επιφανειών. Επίσης παρουσιάζουμε μια γρήγορη και αποτελεσματική μέθοδο υπολογισμού των ενεργειακών χασμάτων σε ημιαγωγούς.

Η πρώτη επιφάνεια που μελετάμε είναι η (100) επιφάνεια του Πυριτίου, η οποία είναι μια από τις απλούστερες στερεές επιφάνειες και ταυτόχρονα αποτελεί ένα σύστημα με τεράστιο τεχνολογικό ενδιαφέρον, λόγω της χρήσης της στην ανάπτυξη τρανσίστορ και άλλων ημιαγωγικών διατάξεων. Μελετάμε λεπτομερώς τους χημικούς δεσμούς των ατόμων της επιφάνειας, τις ενέργειες των διαφόρων φάσεών της και την ηλεκτρονική δομή της, παρουσιάζοντας εκτενώς τις σύγχρονες θεωρητικές μεθόδους ανάλυσης επιφανειακών διεργασιών. Παρουσιάζουμε προσομοιώσεις του Σαρωτικού Μικροσκοπίου Σήραγγας (Scanning Tunnenling Microscope, STM), οι οποίες επιτρέπουν απευθείας σύγκριση των θεωρητικών μοντέλων με τις πειραματικές παρατηρήσεις.

Στη συνέχεια μελετάμε την εμπλουτισμένη με 'Ανθρακα Si(100), μια επιφάνεια που έχει γίνει αντικείμενο εντατικής έρευνας τα τελευταία χρόνια καθώς αποτελεί το αρχικό στάδιο κατασκευής κραμμάτων Πυριτίου-'Ανθρακα τα οποία χρησιμοποιούνται για κατασκευή γρήγορων τρανσίστορ, καθώς και σαν υπόβαθρο για ανάπτυξη κβαντικών δομών (SiGe quantum dots). Για μικρό ποσοστό 'Ανθρακα στο σύστημα, αποκαλύπτουμε για πρώτη φορά μια εντυπωσιακή τάξη μακράς εμβέλειας στην κατανομή των ατόμων C. Η πρόβλεψη αυτή δεν έχει δυστυχώς ακόμη ελεγχθεί πειραματικά. Για μεγαλύτερο ποσοστό 'Ανθρακα στο σύστημα, όπου υπάρχουν πειραματικά δεδομένα, βρίσκουμε τις δομές που σχηματίζονται και οι οποίες ευθύνονται για τις μοναδικές εικόνες που φαίνονται στο μικροσκόπιο STM.

Η Διατριβή καταλήγει με μια καταλυτική διεργασία, και συγκεκριμένα την αναγωγή του Μονοξειδίου του Αζώτου (NO) παρουσία επιφάνειας Τριοξειδίου του Μολυβδενίου (MoO_3(010)). Μελετούμε διάφορες δομές προσροφημένου NO στην επιφάνεια, θεωρώντας ότι αυτό δεν διασπάται, όπως συμβαίνει σε άλλους καταλύτες, και προτείνουμε τη δημιουργία δινιτροσυλίου ($(NO)_2$) σαν το ενδιάμεσο στάδιο της κατάλυσης.

Contents

Preface

Surface Science is today a growing area of Condensed Matter and Materials Physics. Knowledge of the structure and properties of solid surfaces is essential both for the growth of materials through deposition or epitaxial techniques and for its use as a catalyst. Semiconductor surfaces in particular are useful for device fabrication, as technology today reaches the nanoscale. Molecular transistors and quantum-dot based circuits have already been presented as the next generation of microelectronics; in this era, surface rather than bulk properties of materials are expected to characterize them.

In addition to the applications, Surface Science is an outstanding framework where most concepts of modern physics and chemistry can be applied. Macroscopically, the two-dimensional character of the electronic surface states gives rise to novel phenomena, such as the quantum Hall effect. Surface properties, such as surface energy and tension, are those that characterize the shape of objects surrounding us. Formation and mobility of cracks are responsible for the brittle or ductile behavior of materials, while properties of a crack can be explained in terms of properties of the surface.

In the atomistic level, atoms on solid surfaces are under-coordinated compared to atoms in the bulk; this accounts for the chemical activity of surfaces and their use in heterogeneous catalysis. Surface atoms usually rearrange themselves in patterns different than those appearing in the bulk, an effect called surface reconstruction. In many solids, reconstruction is accompanied by a change in the electronic structure of surface atoms. A surface is perhaps the only solid system, apart from amorphous materials, where atoms of the same element can co-exist in different states. For example, sp^3, sp^2, and unhybridized Si atoms can be found on pure Si(100).

In this framework, the need for theoretical tools capable of precise, atomistic-level prediction of surface properties is essential. The presence of dangling bonds on the surface, the charge transfer associated with surface relaxation and reconstruction, and the stretched interatomic distances which are present in any solid surface, demand for a quantum mechanical treatment of the geometrical and electronic properties of the surface. Density Functional Theory, which allows the reduction of the many-body Schrödinger equation to the single-electron Kohn-Sham equation, is the theoretical method used today in the vast majority of theoretical investigations of solid surfaces.

Physics of solid surfaces is the subject of several books and review articles. Those used mostly by the author are the books of Dąbrowski and Müssig [22], Mönch [83], Lüth [76], and Venables [137]. Among the many computational physics books, the most useful for the author where the books of Thijssen [131] and Jensen [49].

In the present Dissertation, DFT is applied to several characteristic surfaces and surface properties: Pure Si(100) is a prototype for both theoretical and experimental surface physics; although there are hundreds of published studies on the subject, there still exist several open questions on the structure. C-alloyed Si(100) is a system with several microelectronics applications, as C-enriched Si seems a promising material where the band structure and he fundamental gap can be tuned by changing the C content or the positions of C atoms in the alloy. Moreover, it can be used as a substrate for growth of SiGe quantum dots ands high-frequency transistors. The Dissertation concludes with a study of NO adsorption on $MoO_3(010)$, which gives a flavor of catalysis from the atomistic point of view, and attempts to bridge the gap between basic science and industrial applications.

The valuable advise and choice of surface Physics as the topic of my PhD from my supervisor, Prof. Efthimios Kaxiras, is gratefully acknowledged. His ability to choose a promising problem to deal with, and more important, to choose the most efficient method to solve a particular problem will always be an example in my career. His pioneering research in many different subjects guided me to obtain a deeper and interdisciplinary knowledge of Physics. I also thank Prof. Kaxiras for inviting me to spend two years (1999-2001) as a research assistant at the Division of Engineering and Applied Sciences of Harvard University. In the environment of one of the leading academic institutions of the world, I was able to interact with prominent scientists, attend high-level colloquia and seminars, and participate into outstanding conferences.

Continuous support and guidance from the co-advisor of this Thesis, Prof. Pantelis Kelires throughout the years of our collaboration were inestimable. I am grateful to him for sharing his deep knowledge of Statistical and Semiconductor Physics, and for stimulating my work in these subjects. Our collaboration is extended well beyond the topic of this Dissertation.

I especially thank my collaborators in projects relevant or irrelevant to the present thesis: Prof. Cynthia Friend from Harvard (NO on $MoO_3(010)$), Dr. Paul

Maragakis from Harvard (diffusion of adatoms and ad-dimers on Si(100)), Helen Eisenberg from Weizmann Institute, Israel (SiGe alloys growth on Si(100)), Cyril Guedj from PSI, Switzerland (C incorporation on Si(100)), Alina Pascale from Luminy, Marseille (SiGe quantum dots) and Maria Fyta from the University of Crete (nanostructures in amorphous Carbon).

Being at Harvard, I was lucky to share my office with Dr. Umesh Waghmare; his deep knowledge of Theoretical Materials Science and his approach to Science and Life have deeply affected my way of thinking. All members of the Kaxiras' group have helped me with one or the other way to improve my understanding of Physics: N. Choly, Dr. H. Kim, Dr. D. Orlikowski, Dr. I. J. Park, Dr. O. Politano and Dr. G. Smith. Dr. Leeor Kronik (from Minessota) has helped me a lot to understand many technical issues on the implementation of DFT to complex systems. I thank Dr. P. Maragakis for his help on computers at the beginning of my PhD, and for critical reading of the thesis manuscript. All-night long discussions on Physics and Life with my cordial friend, Dr. Dionisios Margetis, are unforgettable, as are Dionisios' passion for Physics and Mathematics.

My office-mates and co-workers at the Kelires group, George Hadjisavvas, Christos Mathioudakis and Maria Fyta, have helped a lot during the process of writing the present text, and have supplied useful comments on the manuscript of the thesis. I thank Dr. G. Kopidakis for inspiring discussions. Some of the calculations for this thesis were performed at the Computational Center of the University of Crete; the director, Hara Tomara, and the staff were of important assistance to me.

I am obliged for their excellent teaching, inspiring discussions and support, to the Faculty of the Physics Department, University of Crete, including E. Economou, S. Trahanas, A. Andriotis, P. Ditsas, D. Charalambidis and S. Anastasiadis. Scientific discussions and many recreational moments spent with intimate friends Michael Makris, Nick Voulgarakis, Tasia Rissanou and Panayotis Benetatos are gratefully acknowledged. I also thank M. Eleftheriou, J. Karadamoglou, M. Voultsidou, D. Counalakis, R. Penciu and D. Kehagiadaki for their close friendship and understanding.

My deepest gratitude is expressed to my parents, Nikos and Irene Remediakis, and my sister, Ioanna; this dissertation would have never been completed without their unlimited love, support and encouragement.

Chapter 1

Introduction

In this Chapter a scetch of the theoretical steps and approximations leading to the first-principles calculation of the total energy in realistic molecular or solid systems is presented. We present the core computer programs used in this Dissertetion to calculate properties of solid materials and discuss important technical issues.

A theory providing a method for the accurate calculation of material properties has always been the focus of Solid State Physics, both to explain the observations and to predict new structures with tailored electronic, optical, magnetic or elastic properties. The gap between technology and basic science closes every year, as improved hardware and software allows theoretical treatment for larger systems, and the need for low-power consumptive and small sized devices has led technology to the nano-scale.

Although more rigorous quantum chemical methods such as Hartree-Fock and configuration interaction (CI) were developed shortly after the discovery of Quantum Mechanics, the theory that revolutionized Materials Science was Density Functional Theory (DFT), which was developed in the sixties. As we discuss in the next section, DFT made it possible to obtain equilibrium geometries and total energies of complex systems at a very high degree of accuracy. For the majority of studied materials, calculated bond lengths agree within 3% to experiment. Elastic constants can be calculated today with an error of 10%. In the last three decades, qualitative explanation of the observed chemical bonding in solids has been replaced by accurate predictions.

In the following, we review the major steps in the solution of the many body Schrödinger equation for a system of electrons and nuclei. They are the Born-Oppenheimer theory, that allows the separate study of electrons and nuclei, DFT, that transforms the many-electron into single-particle problem, the pseudopotential, allowing the elimination of core electrons and significantly simplifying the calculation, and Bloch's theorem, that allows study of a periodic system only inside the primitive unit cell. All four steps are in principle *exact*; approximations are involved either to simplify the equations, as in the classical treatment of nucleic motion, or to account for terms that cannot be calculated, like the correlation energy in DFT.

1.1 The main approximations

The general non-relativistic Hamiltonian for a system of N electrons and N_I ions (or nuclei) is

$$\begin{aligned}\mathcal{H}_{tot} = \sum_{I=1}^{N_I} \frac{-\hbar^2}{2m_I}\nabla_I^2 + \sum_{i=1}^{N} \frac{-\hbar^2}{2m}\nabla_i^2 + \\ +\frac{1}{2}\sum_{\substack{i,j=1\\ i\neq j}}^{N} \frac{e^2}{|\mathbf{r}_i-\mathbf{r}_j|} + \frac{1}{2}\sum_{\substack{I,J=1\\ I\neq J}}^{N_I} \frac{Z_I Z_J e^2}{|\mathbf{R}_I-\mathbf{R}_J|} + \sum_{i=1}^{N}\sum_{I=1}^{N_I} \frac{Z_I e^2}{|\mathbf{r}_i-\mathbf{R}_I|} + \hat{V}_{ext}.\end{aligned} \tag{1.1}$$

Here, $\mathbf{r}_i$ and $\mathbf{R}_I$ are the positions of electron i and nucleus I, respectively. m_I denotes the mass of nucleus I and Z_I its atomic number; N is the total number of electrons and N_I the total number of nuclei. The Laplacian with respect to the position of electron i is defined as

$$\nabla_i^2 = \frac{\partial^2}{\partial x_i^2} + \frac{\partial^2}{\partial y_i^2} + \frac{\partial^2}{\partial z_i^2}, \quad \text{where} \quad \mathbf{r}_i = (x_i, y_i, z_i);$$

the definition of the Laplacian ∇_I^2 associated with nucleus I is analogous. $\hat{V}_{ext}$ is the external potential (for example an applied electric field), which is in general a function of the positions of electrons, nuclei, and time.

The first two terms in Eq. (1.1) represent the kinetic energy of the particles, while the last three the potential energy. The latter can be decomposed into three parts: electron-electron, nucleus-nucleus and electron-nucleus interaction. All the potential energy terms are described by Coulomb's law.

The evolution of the system will be governed by the Schrödinger equation,

$$\mathcal{H}_{tot}\Psi = \mathrm{i}\hbar\frac{\partial\Psi}{\partial t} \tag{1.2}$$

In the case where the external potential does not have an explicit time dependence, the energy of the system will be a solution of the time-independent Schrödinger equation,

$$\mathcal{H}_{tot}\Psi(\mathbf{r}_1, \ldots, \mathbf{r}_N, \mathbf{R}_1, \ldots, \mathbf{R}_{N_I}) = E\Psi(\mathbf{r}_1, \ldots, \mathbf{r}_N, \mathbf{R}_1, \ldots, \mathbf{R}_{N_I}) \tag{1.3}$$

The ground state energy of the system will then be the lowest eigenvalue of the Hamiltonian operator (1.1).

1.1.1 Eliminating the ionic degrees of freedom: The Born-Oppenheimer theory

The Born-Oppenheimer theory [8] and the adiabatic approximation eliminates the ionic kinetic energy term from Eq. (1.1). This theory can be summarized into three equations:

$$\Psi(\mathbf{r}_1, \ldots, \mathbf{r}_N, \mathbf{R}_1, \ldots, \mathbf{R}_{N_I}) = \sum_l \Psi_l^I(\mathbf{R}_1, \ldots, \mathbf{R}_{N_I})\Psi_l(\mathbf{r}_1, \ldots, \mathbf{r}_N) \tag{1.4}$$

$$\mathcal{H}\Psi_l = E_l\Psi_l \tag{1.5}$$

$$(T_I + E_l + \mathcal{A})\Psi_l^I = E\Psi_l^I \tag{1.6}$$

The first equation, (1.4), decomposes the wave function into an ionic part Ψ_l^I and an electronic part Ψ_l. The electronic wave function is derived from the solution of the Schrödinger equation (1.5) for fixed positions of the nuclei, so Ψ_l depends only implicitly on the positions of atoms. T_I is the ionic kinetic energy operator, namely the first term in Eq. (1.1); H includes all the other terms, so that

$$\mathcal{H}_{tot} = T_I + \mathcal{H}. \tag{1.7}$$

Eq. (1.6) implies that the eigenenergies E_l of the electrons act as potential for the motion of ions. The operator $\mathcal{A}$ includes terms of the form $\langle \Psi_l | T_I | \Psi_m \rangle$, i.e matrix elements of T_I between eigenstates of H. The Born-Oppenheimer approximation consists of two steps:

i) The *adiabatic* approximation states that crossings between potential energy surfaces are not likely to happen, and thus the off-diagonal matrix elements included in $\mathcal{A}$ can be omitted. Thus the operator $\mathcal{A}$ can be substituted by a simple potential $U(R)$.

ii) The next step is to eliminate the term $U(R)$ since it is smaller than E_l by a factor of $\frac{m}{m_I}$.

Both approximations are based in the fact that the mass of the electron is much smaller than the mass of any nucleus. In most cases (except perhaps solid H and He), a classical treatment of the ionic motion is sufficient; in that case, the Schrödinger equation for the ions (1.6) can be replaced by a Newton equation of motion,

$$m_I \frac{\mathrm{d}}{\mathrm{d}t} \mathbf{U}_I = -\nabla_I E_l, \qquad \text{where} \qquad \mathbf{U}_I = \frac{\mathrm{d}}{\mathrm{d}t} \mathbf{R}_I, \tag{1.8}$$

and the total energy will be

$$E_{tot} = E_l + \sum_{I=1}^{N_I} \frac{1}{2} m_I u_I^2. \tag{1.9}$$

1.1.2 The single electron picture: Density Functional Theory

The Density Functional Theory (DFT) was developed in the sixties and is based on the work of Hohenberg, Kohn and Sham [44, 66]. Detailed reviews of the DFT concepts and applications can be found in Refs. [32, 53, 97]. In Chapter 2, we give a brief review of a generalized DFT that includes excited states.

DFT is based on the two famous theorems of Hohenberg and Kohn:

i) The ground state wave function, Ψ_0 is a unique functional of the electron density $\rho(\mathbf{r})$.

Since $E_0 = \langle\Psi_0|\mathcal{H}|\Psi_0\rangle$, it follows that the ground state energy is also a unique functional of the electron density.

ii) The ground state energy functional $E[\rho]$ has a minimum when ρ equals the true density of the system; its minimum value is the ground state energy E_0.

The density is defined as

$$\rho(\mathbf{r}) = \int |\Psi_0(\mathbf{r}, \mathbf{r}_2, \ldots \mathbf{r}_N|^2 \mathrm{d}^3 r_2 \ldots \mathrm{d}^3 r_N. \qquad (1.10)$$

Taking $\hat{V}_{ext} = \sum_i V_{ext}(\mathbf{r}_i)$, the density functional of the total energy in the ground state is

$$E_{tot}[\rho] = T[\rho] + \frac{e^2}{2}\int\int \frac{\rho(\mathbf{r})\rho(\mathbf{r}')}{|\mathbf{r}-\mathbf{r}'|} d^3r d^3r' + E_{xc}[\rho] + \sum_{I=1}^{N_I} Z_I e^2 \int \frac{\rho(\mathbf{r})}{|\mathbf{r}-\mathbf{R}_I|} d^3r$$
$$+ \int \rho(\mathbf{r}) V_{ext}(r) \mathrm{d}^3 r + \frac{1}{2}\sum_{\substack{I,J=1\\ I\neq J}}^{N_I} \frac{Z_I Z_J e^2}{|\mathbf{R}_I - \mathbf{R}_J|}. \qquad (1.11)$$

The electronic kinetic energy, $T[\rho]$ equals

$$T[\rho] = \langle\Psi_0|\sum_{i=1}^{N} \frac{-\hbar^2}{2m}\nabla_i^2|\Psi_0\rangle \qquad (1.12)$$

and the exchange and correlation energy is defined from

$$\langle\Psi_0|\frac{1}{2}\sum_{\substack{i,j=1\\ i\neq j}}^{N} \frac{e^2}{|\mathbf{r}_i - \mathbf{r}_j|}|\Psi_0\rangle = \frac{e^2}{2}\int\int \frac{\rho(\mathbf{r})\rho(\mathbf{r}')}{|\mathbf{r}-\mathbf{r}'|} d^3r d^3r' + E_{xc}[\rho]. \qquad (1.13)$$

Usually one deals with the exchange-correlation energy density, ϵ_{xc}, defined from

$$E_{xc}[\rho] = \int \epsilon_{xc}[\rho] d^3 r. \qquad (1.14)$$

The exchange and correlation energy can be thought as a correction to the electrostatic integral in Eq. (1.13) due to the fact that the average electron-electron distance is larger than what it would be if the electron was a classical point charge. The exchange interaction is a result of the Pauli principle, which does not allow two electrons to come very close. It can be calculated *exactly* for the homogeneous electron gas by solving the Hartree-Fock equations. The result is usually expressed in terms of r_s, where $\frac{4}{3}\pi r_s^3 = \rho^{-1}$:

$$\epsilon_x^{hom}(\rho) = -\frac{3}{4\pi}\left(\frac{9\pi}{4}\right)^{\frac{1}{3}} \frac{1}{r_s}. \qquad (1.15)$$

The usual definition of correlation energy is that it includes all corrections in the electron-electron interaction beyond the Hartree-Fock approximation. Correlation can be seen as a many body effect arising from the nature of the Coulomb potential. In this picture, each electron carries a "Coulomb hole" or "correlation hole" as it moves around, not allowing other electrons to approach it very closely. To date, there is no analytic expression for the correlation energy; there exist several approximations, the most popular in materials science being the following:

i) **Local Density Approximation (LDA)**: This is by far the most popular approximation in the electronic structure community, introduced in the original papers of DFT [66]. In the context of Eq. (1.14), it consists of approximating $\epsilon_{xc}[\rho] \approx \epsilon_{xc}^{hom}(\rho(\mathbf{r}))$, where $\epsilon_{xc}^{hom}(\rho)$ is the exchange and correlation energy density of the homogeneous electron gas of density ρ, which can be calculated numerically, for example by using Quantum Monte Carlo techniques. Although LDA is expected to be valid for slowly varying densities only, it gives reasonably well results for the total energy of even polar covalent and ionic systems.

ii) **Generalized Gradient Approximation (GGA)**: This approximation was introduced by Perdew and Wang [100]. In the context of Eq. (1.14), it consists of approximating $\epsilon_{xc}[\rho] \approx \epsilon_{xc}^{hom}(\rho(\mathbf{r}))F[\rho]$. The functional F is expressed in a semiempirical way as a polynomial of the variable $s = |\nabla\rho(r)|/\rho(r)^{4/3}$. For a detailed description of GGA, see Ref. [98].

The second theorem of Hohenberg and Kohn together with Eq. (1.11) and LDA or GGA give a method for calculating the total energy of a molecular or solid system, provided we have an approximation for the functional of the kinetic energy, $T[\rho]$. Instead of dealing with the many-body wavefunction, we only need to find a function $\rho(\mathbf{r})$ which minimizes $E[\rho]$.

In realistic systems, the kinetic energy represents the larger part of the total energy, so its approximation is crucial. In the context of Thomas-Fermi approximation, $T[\rho]$ equals the kinetic energy of a homogeneous electron gas, while recently more and more elaborate kinetic energy functionals are presented [18].

An exact method for calculating the total energy, $E[\rho]$, which gives insight to the physical properties of the system, was proposed by Kohn and Sham [66]. In this picture, electrons are replaced by non-interacting quasiparticles moving under the influence of the same potential as the electrons. The quasiparticle energies and wavefunctions are the N lowest eigenvalues and the corresponding wave functions of the Kohn-Sham Hamiltonian

$$H = -\frac{\hbar^2}{2m}\nabla^2 + \int \frac{e^2\rho(\mathbf{r}')}{|\mathbf{r}-\mathbf{r}'|}\mathrm{d}^3r' + V_{xc}(\mathbf{r}) + \sum_{I=1}^{N_I} \frac{Z_I e^2}{|\mathbf{r}-\mathbf{R}_I|} + V_{ext}(\mathbf{r}), \tag{1.16}$$

and

$$H\psi_i(\mathbf{r}) = \epsilon_i \psi_i(\mathbf{r}). \tag{1.17}$$

The second term in Eq. (1.16) is known as the Hartree potential. The last term equals the functional derivative of E_{xc},

$$V_{xc}(\mathbf{r}) = \frac{\delta E_{xc}}{\delta \rho(\mathbf{r})}. \tag{1.18}$$

The density is calculated from the wavefunctions through the standard formula for N non-interacting particles,

$$\rho(\mathbf{r}) = \sum_{i=1}^{N} |\psi_i(\mathbf{r})|^2. \tag{1.19}$$

Eqs. (1.16), (1.17) and (1.19) give an exact method for the calculation of the density $\rho(\mathbf{r})$, introducing no approximations beyond the approximation for the correlation potential. The total energy in Eq. (1.11) will be:

$$E_{tot} = \sum_{j=1}^{N} \epsilon_j - \frac{e^2}{2} \int \frac{\rho(\mathbf{r})\rho(\mathbf{r}')}{|\mathbf{r}-\mathbf{r}'|} d^3r\, d^3r' + \int [\epsilon_{xc}(\mathbf{r}) - V_{xc}(\mathbf{r})]\rho(\mathbf{r}) d^3r$$
$$+ \frac{1}{2} \sum_{\substack{I,J=1 \\ I \neq J}}^{N_I} \frac{Z_I Z_J e^2}{|\mathbf{R}_I - \mathbf{R}_J|}. \tag{1.20}$$

The solution of Eq. (1.17) is done self-consistently, as the Hamiltonian depends on the density, which in terms depends on the eigenfunctions. Mathematically, the problem is to find the solution to the equation

$$\mathcal{K}\rho = \rho, \tag{1.21}$$

where $\mathcal{K}$ is the operator that acts to a given charge density and produces a new one, via the construction of the Kohn-Sham Hamiltonian, the solution of the Kohn-Sham equations and the calculation of the new density from Eq. (1.19). This class of problems is usually solved numerically by applying variations of Newton's method [9], where one assumes a starting density ρ_{in}, calculates the new density ρ_{out}, and find the starting density for the next step by mixing ρ_{in} and ρ_{out}. The procedure is repeated until the new density equals the old density.

The development of DFT and the need for calculations in complex systems has yielded several efficient algorithms for the solution of the generalized Newton problem described in Eq. (1.21). The difference of the present problem compared to traditional minimization problems is that the derivative of the operator $\mathcal{K}$ cannot be calculated. The most popular self-consistency algorithms used today are the so-called Pulay [102] and modified Broyden [136, 51, 54]. Recently, a storage-saving method for the quick achievement of self-consistency was developed by Jain, Kronik and Chelikowsky [48].

1.1.3 Eliminating the core electrons: the pseudopotential

The pseudopotential concept is based on the well-known observation that most properties of solid or molecular systems depend solely on the valence electrons. Moreover, the tight-binding description of the chemical bond requires that only the tail of the valence wave function outside the core radius of the ion is needed for the calculation of the Hamiltonian matrix elements.

The pseudopotential approximation consists of two steps: First, we consider only the valence electrons for the given atom. Second, we construct a *pseudopotential* operator V such that the calculated atomic ionization energies and the electronic wave functions outside the core radius r_C are exactly equal to those obtained from solving the all-electron Schrödinger equation for the atom.

The so-called *norm conserving* pseudopotentials, like the Bachelet-Hamann-Schlütter [3] are usually constructed by the following algorithm:

1. Find the electronic wave functions and energies for the free atom (for example by solving the Kohn-Sham or Hartree-Fock equations)
2. Construct a *pseudo*-wavefunction ϕ which equals the actual valence wavefunction for $r > r_C$ and is a smooth function for $r < r_C$; both ϕ and ϕ' are continuous at $r = r_C$, and ϕ is normalized.
3. Find the pseudopotential operator by inverting the Schrödinger equation

$$(\frac{-\hbar^2}{2m}\nabla^2 + V_e + V_{pseudo})\phi = \epsilon\phi, \tag{1.22}$$

   where ϵ is the energy of the state of interest as calculated in step (1), and V_e is the term describing the electron-electron interaction. In the DFT picture, V_e is the sum of the Hartree and exchange-correlation potentials.

Usually the pseudopotential operator is written in the form

$$V_{pseudo} = \sum_{l=0}^{\infty} V_l(r) \sum_{m=-l}^{l} |ml\rangle\langle ml|, \tag{1.23}$$

where $|ml\rangle$ is the spherical harmonic characterized by m and l, and $V_l(r)$ is an analytical function, typically a polynomial multiplied by a gaussian, containing several parameters that are fitted to reproduce Eq. (1.22). For details on construction of pseudopotentials, see [38],[3] and [106].

1.1.4 From the infinite to finite: Bloch theorem

The Bloch theorem [7] states that if the Hamiltonian is periodical, $H(\mathbf{r}+\mathbf{R}) = H(\mathbf{r})$, then its eigenvalues and eigenfunctions will be characterized by a wave vector $\mathbf{k}$ (which is the analog of the quantum number in one-dimensional problems) and the following relation will hold:

$$\psi_{\mathbf{k}}(\mathbf{r}+\mathbf{R}) = e^{i\mathbf{k}\cdot\mathbf{R}}\psi_{\mathbf{k}}(\mathbf{r}). \tag{1.24}$$

Eq. (1.24) allows a huge simplification of the calculations in periodic systems. The main alternatives for studying solid systems are either to consider a large enough cluster, or to take a large portion of the solid and apply periodic boundary conditions. On the other hand, Bloch theorem states that a perfect crystalline solid can be studied within the primitive unit cell by applying the boundary condition (1.24). The single-particle Hamiltonian always has the Bravais lattice periodicity, since in DFT it depends only on the positions of ions and the electronic charge density, which has to follow the underlying atomic periodicity in the absence of external applied fields.

The sums over all electrons required to calculate the density and the total energy are transformed into sums over $\mathbf{k}$ points of the first Brillouin zone. Only a small portion of the Brillouin zone needs to be used, as the eigenvalues $\epsilon_{\mathbf{k}}$ follow the symmetries of the lattice; this portion is called *irreducible* Brillouin zone. We then choose a grid of $\mathbf{k}$ points in the irreducible Brillouin zone, which is dense enough to give converged sums. The number of differnt $\mathbf{k}$ points required for converged energies is usually of the order of ten. A smart method to choose $\mathbf{k}$ points, which is widely used in electronic structure calculations, is that of Monkhorst and Pack [85].

The contribution of the approximations discussed before in the reduction of the computational cost of a quantum-mechanical calculation are summarized in Fig. 1.1. Without any approximation, the solution of the $2N-$body Schrödinger equation requires $\mathcal{O}(e^{2\alpha N})$ operations more than those needed to solve an one-particle Schrödinger equation (α is an arbitrary constant). The Born-Oppenheimer approximation reduces the exponent to its one half, as the electronic and ionic wavefunctions are calculated separately. The single-particle approximation reduces dramatically

Approximation	Wave function to find	Operations required
No approximation:	$\Psi(\mathbf{r}_1,\ldots,\mathbf{r}_N,\mathbf{R}_1,\ldots,\mathbf{R}_N)$	$\mathcal{O}(e^{2\alpha N})$
Born-Oppenheimer:	$\Psi(\mathbf{r}_1,\ldots,\mathbf{r}_N)$	$\mathcal{O}(2e^{\alpha N})$
Single-electron:	$\psi_i(\mathbf{r})$	$\mathcal{O}(N)$
Pseudopotential:	$\psi_i(\mathbf{r})$	$\mathcal{O}(0.1N)$
Bloch:	$\psi_{\mathbf{k}}(\mathbf{r})$	$\mathcal{O}(10)$

Figure 1.1: Reduction of the computational cost by the approximations discussed in the text, for a solid with N atoms. The solution of a single particle Schrödinger equation is counted as one operation.

the computational cost, as it makes it possible to deal only with single-particle equations and include the many-body effects in a mean-field theory manner. For DFT, the cost is even smaller, as we solve only once the Kohn-Sham equation and populate the resulting spectrum with two electrons of opposite spin in each level. The pseudopotential approach limits the study to valence electrons only, which are typically one tenth of the total number of electrons. Bloch's theorem is *not* an approximation, but it also simplifies the situation as it makes it possible to consider only a few **k** points in place of N electrons.

1.2 The software

The choice of the appropriate software package for the study of a particular system or process is crucial. One has to choose *a priori* the level of approximation willing to employ. For given hardware and available CPU time, use of a more elaborate method results in restricting the time and length scales spanned by the simulations. To date, first-principles methods can give accurate total energy differences, elastic constants, stable and metastable geometries, but they are not capable of finding thermodynamical equilibrium of systems larger than a few tenths of atoms. On the other hand, empirical potentials have a limited success in describing situations where bond breaking and bond formation occurs, but offer greater statistical precision. The tight-binding method is an intermediate between quantum mechanical and classical description of the interatomic interactions.

In the following, we give a brief description of the software packages used in this Thesis, in descending order of accuracy and ascending order of length scale or statistical accuracy that can be addressed. The ordering is according to my experience with those packages in their present distributions; it is possible that newer versions of those programs may be faster, as the development of electronic structure methods is perhaps the most active area of research in computational physics. Quantum chemical methods more accurate than DFT, like Configuration Interaction (CI) or the GW method, where not used by the author; this is the case as well for the recently developed so-called Order-N DFT methods.

1.2.1 HARES

High-performance fortran Adaptive Real-space Electronic Structure (HARES) [138] is a package designed for electronic structure calculations of large and complex systems. It is an improved version of the older ACRES package (Adaptive Coordinate Real-space Electronic Structure) [82]. The package is developed and constantly upgraded by the Kaxiras' group at Harvard University, Cambridge, MA.

In this electronic structure approach a finite (curvilinear, in general) grid is used for representing the charge density and the Kohn-Sham wave-functions, and a real-space integration of the quasi-particle Schrödinger equation is performed. The package includes many features beyond a conventional DFT/LDA total energy calculation such as GGA, many choices for charge density mixers, use of symmetries and automatic generation of $\mathbf{k}$ points.

The main code is written in High Performance Fortran (HPF) and is one of the best parallelizable codes in the electronic structure community. It is accompanied by various utilities, among them programs to calculate simulated STM images, densities of states, and GDFT-corrected excitation energies and band structures, as described in Chapter 2. HARES package is available for free upon request to Prof. E. Kaxiras.

1.2.2 Car-Parrinello code

Harvard University Car Parrinello package is a DFT/LDA electronic structure and molecular dynamics code which is a modification by Kaxiras' group of the fhi93md package, developed by the M. Scheffler group at Fritz-Haber Institute, Berlin [115].

In this program the electronic wave functions are expanded in a plane-wave basis set and the Hamiltonian matrix is diagonalized by a modified Car-Parrinello algorithm [12]. The ionic degrees of freedom are relaxed simultaneously with the electronic ones, while there exists a choice for molecular dynamics simulations. This code is very simple and efficient for semiconductors and insulators, but calculations for metallic systems can become very tricky. Although it is faster than HARES for small systems, it is less efficient for larger systems, mainly due to the very simple ionic relaxation algorithm it contains. In addition, the version I used could not run in parallel mode.

The newer version of the code, fhi98md, is said to have overcome those difficulties, and is widely used by many groups around the world.

1.2.3 VASP

The commercial Vienna *Ab initio* Simulation Package (VASP) [69, 67, 68] is also based on Density Functional Theory, and is, together with CASTEP, the best-selling electronic structure package. It is provided by the Haffner-Kresse group at the Universität Wien, Austria.

As a commercial product, it includes by far more features than any public domain electronic structure package. Its efficiency is based on the use of the ultrasoft Vanderbilt-type pseudopotentials [135], as supplied by G. Kresse and J. Hafner [70]. Because of the smooth pseudopotentials, the required energy cut-offs are very low, and thus the electronic relaxation is fastest. The disadvantage in the use of the Vanderbilt pseudopotentials is based on their *not* norm-conserving character. It is very difficult to have a programm using both ultrasoft and norm-conserving pseudopotentials, so VASP cannot be used with other pseudopotentials.

1.2.4 DYLAX

The Density-Functional Based Tight-Binding Molecular **Dy**namics & Re**lax**ation Package is developed by the T. Frauenheim group at the Technische Universität Chemnitz, Germany. It includes routines for molecular dynamics and relaxation for both open and periodic boundary conditions. The method used for the calculation of total energy and forces is a self-consistent tight-binding scheme [25] where the matrix elements of the tight-binding Hamiltonian depend on the charge density. Recently, DYLAX was extended to include calculation of the response function, which is related to the conductivity and other optical properties, via a realization of the time-dependent density functional theory [86].

DYLAX is a fast and efficient program for calculating properties of complex materials, as the Slater-Coster parameters it contains are fitted to state-of-the-art *ab initio* calculations. Calculated total energy differences agree very well with results of more elaborate calculations, and the agreement is excellent for configurations involving small deformations. As any other tight binding program, it cannot reproduce correctly large deformations, like over-coordinated atoms or processes involving bond breaking. However, it is very fast compared to *ab initio* methods and only slightly slower than empirical tight-binding; it is very powerful for simulations of complex systems, where general properties of the structure are of importance and not the details of all individual bonds, as it is the case in biomolecules [24].

1.2.5 MCMULT

The Monte Carlo program for multi-component semiconductor systems is developed by P. C. Kelires at the University of Crete, Greece. It utilizes a continuous-space Monte Carlo algorithm, where the total energy of the system is calculated by using empirical potentials. The program is capable of simulating various statistical ensembles, including the semi-grand canonical ensemble introduced by Kelires [58].

The package supports a variety of different potentials and calculations of many thermodynamical properties including radial distribution functions, atomic stresses and elastic constants, and works very well for a wide range of temperatures, being capable of simulating crystalline, amorphous and liquid materials.

Chapter 2

Generalized DFT

We review a generalization of the Hohenberg-Kohn-Sham theory to include excited states of the electron gas. The so-called Generalized Density Functional Theory (GDFT), introduced in the mid-80s by L. Fritsche, results in a simple correction formula for the lowest excited states. Although the method is not a substitue for more rigorous theoretical approaches such as the GW method, it gives results in reasonable agreement with experiment. Thus, it makes possible the calculation of semiconductor band structures and band gaps with the computational effort of an ordinary DFT/LDA calculation.

We discuss in detail the approximations leading to the GDFT correction formula, and apply it to examine typical elemental (C,Si,Ge), compound group-IV (SiC, SiGe, GeC) and compound III-IV semiconductors (AlN, AlP, AlAs, AlSb, GaN, GaP, GaAs, GaSb, InP, InAs, InSb). The calculated band gaps are in very good agreement to experiment for elements in 3rd/4th line of the Periodic Table, and they are within 10% off the experimental values in most cases.

In the last two decades, remarkable progress has been made toward accurate calculations of the total energy, using Density Functional theory in the Local Density Approximation (DFT/LDA) [44, 66] and more recently in the Generalized Gradient Approximation [98]. In contrast, the problem of accurate band gap calculations for semiconductors and insulators remains an important theoretical challenge. The quasiparticle spectrum and the electronic excitation properties are much more difficult to compute accurately than the total energy, and DFT/LDA gives unacceptable results for these quantities (often more than 50% off from experimental values). The electronic excitation problem has been addressed by Hedin's GW approximation [42]. Applications of this theory, beginning with the work of Hybertsen and Louie [45, 46], Godby, Schlüter and Sham [33, 34], and other workers [36, 147] have proven very successful: this scheme works essentially perfectly for a wide range of materials, including perfect crystals, surfaces, point defects, etc. However, the GW method requires significant additional computational effort over DFT/LDA because it involves the computation of the dielectric function and the Green's function, and relies on the solution of the Dyson equation, which is more demanding than the single-particle Kohn-Sham equations due to the energy dependence of the self-energy operator.

From a practical point of view, it would be very desirable to have a simple, efficient and reasonably accurate scheme for the calculation of band gaps without extensive computational effort beyond that required for a DFT/LDA calculation. For example, a fast but reasonably reliable method for calculating electronic excitations would be very useful as a guide for the design of new materials which have not yet been produced in the laboratory, for optical and electronic device applications.

Several attempts have been made towards such a simplified scheme. Interesting examples are the theory of Sham and Schlütter [119] which is based on the discontinuity of the exchange and correlation potential, and the work of Gygi and Baldereschi [36] which gives a correction to the LDA band structure based on GW theory. A correction of the band structure, using the framework of the so-called Generalized Density Functional Theory (GDFT), was also proposed by L. Fritsche and co-workers [27, 28, 29, 31, 20]. Fritsche's approach has the added advantage of relying entirely on quantities obtained in a DFT/LDA calculation, so that it is both inherently consistent and computationally efficient. In the present chapter we examine the ability of this approach to give reasonably accurate results for the minimum band gap of semiconductors. In section 2.1 we review the basic ideas of GDFT, including the correction to the DFT/LDA eigenvalues, and give a detailed discussion of the approximations which lead to it. In section 2.2 we present an application of the method to elemental and compound semiconductors and discuss the results we obtained. We conclude in section 2.3 with some remarks on the usefulness of this theory.

2.1 Review of GDFT

The main idea of both the GDFT and the DFT approach is to map the real system of interacting electrons to one of fictitious, non-interacting particles. A theory of this kind should prove that such a mapping is not only possible but unique, and additionally, it should give a recipe for calculating the properties of the real system from those of the fictitious one. The theorem of Hohenberg and Kohn [44] states that all ground state properties can be expressed uniquely using functionals of the density; this implies that if the ground state density of the fictitious system equals that of the real one, then, at least for the ground state, all properties of the two systems are identical.

The GDFT approach is based on the observation that knowledge of the pair density $\rho_2(\mathbf{r}, \mathbf{r}')$ allows the determination of the exchange and correlation effects, whether the state under consideration is the ground state or an excited one. There exists a relationship between the infinitesimal change of the density $\delta\rho$ and the corresponding change in $\delta\rho_2$, which gives again a central role to the density. Based on this theoretical framework, Fritsche derived a simple formula for correcting the excitation energies of the single-particle spectrum, which, as is well known, are incorrect within DFT. The question whether or not GDFT can describe in a practical way all excited states is still open, but the method seems to work reasonably well when applied to the first few conduction bands of semiconductors, as the results presented below indicate.

In the following we give a brief description of GDFT and the correction to the eigenvalues of excited states, for two reasons: first so that we provide the reader with a complete description of the calculations presented, and second, and more importantly, so that we can identify in detail all the approximations involved, which has not been done explicitly elsewhere. We only include here the steps that are absolutely necessary to make the approximations evident, and refer the reader to the original work for more detailed derivations. For simplicity, in the present work we will omit spin indices and deal with an unpolarized electron gas. The extension to spin-polarized formulae is straightforward.

2.1.1 The GDFT concept

The basic statement of GDFT is that any eigenstate Ψ_n of the real-system hamiltonian (in atomic units),

$$H = \sum_{j=1}^{N} \left[-\frac{\nabla_j^2}{2} + V_{ext}(\mathbf{r}_j) \right] + \frac{1}{2} \sum_{i \neq j} \frac{1}{|\mathbf{r}_i - \mathbf{r}_j|}, \tag{2.1}$$

can be uniquely mapped to a single Slater determinant Φ_n, built from N orbitals which satisfy the Kohn-Sham equations [66]:

$$\left[-\frac{\nabla^2}{2}+V_{ext}(\mathbf{r})+V_H^{(n)}(\mathbf{r})+V_{xc}^{(n)}(\mathbf{r})\right]\psi_j^{(n)}(\mathbf{r})=\varepsilon_j^{(n)}\psi_j^{(n)}(\mathbf{r}), \tag{2.2}$$

where $V_H^{(n)}(\mathbf{r})$ is the Hartree potential, and $V_{xc}^{(n)}(\mathbf{r})$ is the function that connects the infinitesimal change of the density with the corresponding change in the exchange and correlation energy:

$$\delta E_{xc}^{(n)}=\int V_{xc}^{(n)}(\mathbf{r})\delta\rho_n(\mathbf{r})d^3r+\int W_{xc}^{(n)}(\mathbf{r})\delta\sigma_n(\mathbf{r})d^3r. \tag{2.3}$$

For details about the meaning of σ and W see the original work of Fritsche [27, 20, 28, 31, 29]. Here we note only that for the ground state $\sigma_0(\mathbf{r})=0$. $E_{xc}^{(n)}$ is defined by:

$$\langle V_{e-e}\rangle^{(n)}\equiv\frac{1}{2}\int\frac{\rho_n(\mathbf{r})\rho_n(\mathbf{r}')}{|\mathbf{r}-\mathbf{r}'|}d^3rd^3r'+E_{xc}^{(n)}, \tag{2.4}$$

where $\langle V_{e-e}\rangle^{(n)}$ denotes the total electron-electron interaction energy in the eigenstate Ψ_n. If one defines the exchange and correlation energy per particle $\varepsilon_{xc}^{(n)}$ by:

$$E_{xc}^{(n)}\equiv\int\varepsilon_{xc}^{(n)}(\mathbf{r})\rho_n(\mathbf{r})d^3r, \tag{2.5}$$

it is easy to find that

$$\varepsilon_{xc}^{(n)}(\mathbf{r})=-\frac{1}{2}\int\frac{\rho_n(\mathbf{r}')f^{(n)}(\mathbf{r},\mathbf{r}')}{|\mathbf{r}-\mathbf{r}'|}d^3r', \tag{2.6}$$

where $f^{(n)}(\mathbf{r},\mathbf{r}')$ is the correlation factor. The $E_{xc}^{(n)}$ defined here is clearly different from the DFT one as already pointed out by Biagini [5], but E_{xc}^{DFT} and $E_{xc}^{(0)}$ change in the same way when the density changes, that is $V_{xc}^{(0)}(\mathbf{r})=V_{xc}^{DFT}(\mathbf{r})$ as argued by Fritsche [30]. Thus, GDFT coincides with DFT when the ground state is considered.

The N orbitals which are contained in Φ_n have to be selected so that the density equals that derived directly from Ψ_n, and therefore the following relation holds:

$$\begin{aligned}\rho_n(\mathbf{r})\ &\equiv N\textstyle\int|\Psi_n(\mathbf{r},\mathbf{r}_2,...,\mathbf{r}_N)|^2d^3r_2...d^3r_N\\ &=N\textstyle\int|\Phi_n(\mathbf{r},\mathbf{r}_2,...,\mathbf{r}_N)|^2d^3r_2...d^3r_N\\ &=\sum_j|\psi_j^{(n)}(\mathbf{r})|^2.\end{aligned} \tag{2.7}$$

The energy $E_n=\langle\Psi_n|H|\Psi_n\rangle$ can be calculated in terms of the ψ_j's and ε_j's [29]. The result is:

$$\begin{aligned}E_n=\sum_j\varepsilon_j^{(n)}-\frac{1}{2}\int\frac{\rho_n(\mathbf{r})\rho_n(\mathbf{r}')}{|\mathbf{r}-\mathbf{r}'|}d^3rd^3r'&\\ +\int[\overline{\varepsilon}_{xc}^{(n)}(\mathbf{r})-V_{xc}^{(n)}(\mathbf{r})]\rho_n(\mathbf{r})d^3r,&\end{aligned} \tag{2.8}$$

with

$$\bar{\varepsilon}_{xc}^{(n)}(\mathbf{r}) = \int_0^1 \varepsilon_{xc}^{(n)}(\mathbf{r}, \lambda) d\lambda, \tag{2.9}$$

where $\varepsilon_{xc}^{(n)}(\mathbf{r}, \lambda)$ is the the exchange and correlation energy per particle in a system of electrons whose interaction is $V_{e-e}(\mathbf{r}, \mathbf{r}') = \frac{\lambda}{|\mathbf{r}-\mathbf{r}'|}$. By analogy, all quantities denoted by a symbol with a bar imply a similar integral over λ as in (2.9).

2.1.2 Elementary excitations

The preceding discussion would be useful if one could find Ψ_n and construct from it the density ρ_n and the potentials, which in general is not feasible. However, when considering the ground state the situation is much better because the energy has to have a minimum: this leads to the choice of the N lowest-energy orbitals ψ_j for the sum in Eq. (2.7). This is a physically clear choice, although there is no rigorous proof of its validity. The next step is to find an approximation for V_{xc} and solve Eq. (2.2) self-consistently.

An elementary excitation of the system, Ψ_1, can be approximately mapped to a determinant Φ_1 similar to Φ_0 except that it has an orbital ψ_f where Φ_0 has ψ_i. The other orbitals in Φ_1 will be slightly different from the initial ones due to the change of the density and the corresponding change of the potential. The correct excitation energy is

$$\Delta E = E_1 - E_0 = \varepsilon_f - \varepsilon_i + \Delta_{fi}. \tag{2.10}$$

The above equation can be interpreted as meaning that the eigenvalues of the Kohn-Sham hamiltonian (2.2) for the unoccupied states (denoted by the subscript f), which are not included in forming the Slater determinant from the N-lowest ones (denoted by the subscript i), have to be corrected and the correction is:

$$\varepsilon_f^{corr} = \varepsilon_f + \Delta_{fi}. \tag{2.11}$$

Using Eq.s (2.10) and (2.8) we have

$$\Delta_{fi} = \sum_{j \neq i} \Delta\varepsilon_j - \Delta E_H + \Delta\overline{E}_{xc} - \Delta E'_{xc}, \tag{2.12}$$

with the definitions

$$E_H = \frac{1}{2} \int \frac{\rho(\mathbf{r})\rho(\mathbf{r}')}{|\mathbf{r}-\mathbf{r}'|} d^3r d^3r', \tag{2.13}$$

$$\overline{E}_{xc} = \int \bar{\varepsilon}_{xc}(\mathbf{r})\rho(\mathbf{r}) d^3r, \tag{2.14}$$

$$E'_{xc} = \int V_{xc}(\mathbf{r})\rho(\mathbf{r}) d^3r. \tag{2.15}$$

The change of the density can be divided into two parts:

$$\Delta\rho = \Delta\rho_0 + \Delta\rho_R, \tag{2.16}$$

where

$$\Delta\rho_0 = |\psi_f(\mathbf{r})|^2 - |\psi_i(\mathbf{r})|^2, \tag{2.17}$$

and $\Delta\rho_R$ is the response (hence the subscript R) in the density due to the slight change of the orbitals not involved in the transition.

We can treat the difference between the Kohn-Sham potential for the excited state and that for the ground state as a perturbation to the latter, and obtain for the eigenvalue difference:

$$\Delta\varepsilon_j = \int |\psi_j(\mathbf{r})|^2[\Delta V_H(\mathbf{r}) + \Delta V_{xc}(\mathbf{r})]d^3r, \tag{2.18}$$

so that

$$\begin{aligned}\sum_{j\neq i}\Delta\varepsilon_j = &\int \rho_0(\mathbf{r})\Delta V_H(\mathbf{r})d^3r + \int \rho_0(\mathbf{r})\Delta V_{xc}(\mathbf{r})d^3r \\ &- \int |\psi_i(\mathbf{r})|^2[\Delta V_H(\mathbf{r}) + \Delta V_{xc}(\mathbf{r})]d^3r.\end{aligned} \tag{2.19}$$

The last term of the above expression is expected to be small.

The terms involving the Hartree potential can be written in the form

$$\Delta E_H \;\; = \textstyle\int \rho_0(\mathbf{r})\Delta V_H(\mathbf{r})d^3r + \frac{1}{2}\int \Delta\rho(\mathbf{r})\Delta V_H(\mathbf{r})d^3r. \tag{2.20}$$

The last term is quadratic in the density change and thus it can be omitted. As for the term in Eq. (2.15) we have:

$$\begin{aligned}\Delta E'_{xc} = &\int \rho_0(\mathbf{r})\Delta V_{xc}(\mathbf{r})d^3r + \int \Delta\rho_0(\mathbf{r})V_{xc}^{(0)}(\mathbf{r})d^3r \\ +&\int \Delta\rho_R(\mathbf{r})V_{xc}^{(0)}(\mathbf{r})d^3r + \int \Delta\rho(\mathbf{r})\Delta V_{xc}(\mathbf{r})d^3r.\end{aligned} \tag{2.21}$$

The last term is almost zero, as we will show below.

To calculate $\Delta\overline{E}_{xc}$ we use the definition (2.5) and Eq. (2.6), omiting terms which are higher order than linear in changes of the density.

We can divide the change of the correlation factor into two parts, Δf_0 and Δf_R. These two terms do not have an obvious definition, but they do have a clear physical meaning by analogy to the partition of $\Delta\rho$ into $\Delta\rho_0$ and $\Delta\rho_R$. These quantities can be calculated in the case where Φ_n is the true wavefunction of the system:

$$f^{(n)}(\mathbf{r},\mathbf{r}') = -\frac{|\sum_j \psi_j^{(n)^*}(\mathbf{r}')\psi_j^{(n)}(\mathbf{r})|^2}{\rho_n(\mathbf{r})\rho_n(\mathbf{r}')}. \tag{2.22}$$

Using the above division for Δf, keeping terms only linear in changes of the density, and using the symmetry $f(\mathbf{r},\mathbf{r}') = f(\mathbf{r}',\mathbf{r})$ we have:

$$\Delta\overline{E}_{xc} = \int 2\overline{\varepsilon}^{(0)}_{xc}(\mathbf{r})\Delta\rho_0(\mathbf{r})d^3r + \Delta\overline{E}_{xc_0} + \Delta\overline{E}^R_{xc}, \tag{2.23}$$

$$\Delta\overline{E}_{xc_0} = -\frac{1}{2}\int \frac{\rho_0(\mathbf{r})\rho_0(\mathbf{r}')\Delta\overline{f}_0(\mathbf{r},\mathbf{r}')}{|\mathbf{r}-\mathbf{r}'|}d^3rd^3r'. \tag{2.24}$$

For the response term $\Delta\overline{E}^R_{xc}$ we can make use of Eq. (2.3), since $\Delta\rho_R << \Delta\rho$ and for the ground state $\sigma_0 = 0$:

$$\Delta\overline{E}^R_{xc} = \int \Delta\rho_R(\mathbf{r})V^{(0)}_{xc}(\mathbf{r})d^3r. \tag{2.25}$$

Using Eq.s (2.12, 2.17, 2.19, 2.20, 2.21, 2.23) and omitting the small terms we obtain the desired result

$$\Delta_{fi} = \int [2\overline{\varepsilon}^{(0)}_{xc}(\mathbf{r}) - V^{(0)}_{xc}(\mathbf{r})][|\psi_f(\mathbf{r})|^2 - |\psi_i(\mathbf{r})|^2]d^3r, \tag{2.26}$$

which is the formula that Fritsche [29] gives.

Fritsche and Gu [31] noted that this expression is similar to the correction of the DFT quasiparticle spectrum obtained by Godby *et al.* [34], although a rigorous identification of the terms in the two expressions is lacking.

2.1.3 The approximations

The previous derivation is exact, as we will show below, in the case of a transition where the energy difference between the final and the initial state is small compared to the Fermi energy. This condition is satisfied in the cases we study, that is, the lowest conduction bands of semiconductors.

In perturbation theory the change of an eigenvalue depends linearly on the mean of the perturbation. This can be viewed from the opposite side: the difference between the effective potentials, $\tilde{V}^{(1)} - \tilde{V}^{(0)}$ is indeed small, as it was assumed in Eq. (2.18), if $\varepsilon_f - \varepsilon_i$ is small compared to ε_f or alternatively with the Fermi energy. Thus, the perturbative approach is correct for the lowest conduction bands of the semiconductors we study, since in these materials the energy gap is about one tenth of the Fermi energy. This small change of the potential shows that the density should also not change much, since in principle the potential depends solely on it. This is the reason why the terms quadratic in $\Delta\rho$ can be neglected.

Under the same conditions one expects that the response of the states not involved in the transition should be of less importance. The excitation energy is very small compared with the ground state energy and it is not expected to induce large rearrangements to the low energy occupied states; thus, the change in the density due to the transition is dominated by the portion $\Delta\rho_0$ when such an elementary excitation is considered.

Similar arguments justify the neglect of the last term of Eq. (2.19). Having in mind the Hartree-Fock equations, where each particle moves in the potential created by the others, the change of the eigenvalue due to a perturbational change of the remaining states (the portion $\Delta\rho_R$) should be infinitesimal.

Sham and Schlütter [119] proved that for a semiconducting system, where the one-particle energies form almost continuous bands with a gap between ε_N and ε_{N+1}, the exchange and correlation potential has a discontinuity when the number of particles changes from $N-1$ to $N+1$, or equivalently when the number of quasiparticles changes from -1 to +1 (hole or particle excitation). This discontinuity, which they write as $V_{xc}^{(+)} - V_{xc}^{(-)}$, is independent of $\mathbf{r}$. They use the approximation $V_{xc}^{(-)} = V_{xc}^{(0)}$ which is reasonable because ε_{N-1} is very close to ε_N. $V_{xc}^{(+)}$ and $V_{xc}^{(-)}$ have the physical meaning of the effective potentials which govern the motion of a particle or hole excitation respectively. Thus $V_{xc}^{(+)}$ can be identified with our $V_{xc}^{(1)}$; then the difference $V_{xc}^{(1)} - V_{xc}^{(0)}$ must be a constant, so the last term in Eq. (2.21) is proportional to the integral of $\Delta\rho$ which is zero, since both ρ_0 and ρ_1 integrate to the total number of electrons, N.

Since there is a linear relation between $\delta\rho_2$ and $\delta\rho$ (it is this relation that leads to Eq. (2.3)) there is also a similar relation between δf and $\delta\rho$. It is then a reasonable approximation to omit the terms which are higher order than linear in changes of the density in (2.23).

A less clear approximation is that the second term in the right side of Eq. (2.23) is small. The idea is that the change of the density is more important than the change of the correlation factor, that is

$$\int \frac{\rho_0(\mathbf{r})\rho_0(\mathbf{r}')\Delta\overline{f}_0(\mathbf{r},\mathbf{r}')}{|\mathbf{r}-\mathbf{r}'|} d^3r d^3r' << \int \frac{\Delta\rho_0(\mathbf{r})\rho_0(\mathbf{r}')\overline{f}^{(0)}(\mathbf{r},\mathbf{r}')}{|\mathbf{r}-\mathbf{r}'|} d^3r d^3r'. \tag{2.27}$$

$\Delta\overline{f}_0$ is the change in $\overline{f}$ when the states other than f and i are taken to be "frozen". Fritsche [29] argues by analogy to the exchange-only case that this term is indeed small, but a more thorough justification for omitting this term is lacking.

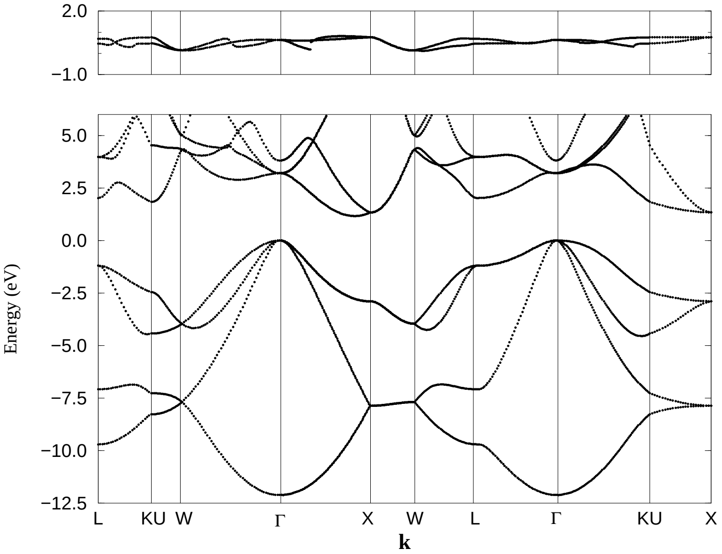

Figure 2.1: Band structure of Si (lower panel) and Δ_{fi} correction for the two lowest conduction levels (upper panel). The apparent cusps in Δ_{fi} correspond to band crossings.

2.2 Implementation and results

We used the familiar LDA expression for the exchange-correlation energy:

$$\bar{\varepsilon}_{xc}^{(n)}(\mathbf{r}) \approx \varepsilon_{xc}^{LDA}(\mathbf{r}) = \varepsilon_{xc}^{hom}(\rho_n(\mathbf{r})), \tag{2.28}$$

where $\varepsilon_{xc}^{hom}(\rho)$ is the exchange-correlation energy per particle of a homogeneous electron gas of density ρ. For the latter we use the results of Ceperley and Alder as they have been parametrized by Perdew and Zunger [13, 99]. The interaction between valence electrons and ionic cores is described by the non-local norm-conserving pseudopotentials of Bachelet *et al.* [3]. The conduction band structure was corrected using Eq. (2.11) while Eq. (2.26) was used with $\bar{\varepsilon}_{xc}^{(0)}(\mathbf{r}) = \varepsilon_{xc}^{LDA}(\mathbf{r})$ and $V_{xc}^{(0)}(\mathbf{r}) = V_{xc}^{LDA}(\mathbf{r})$. The highest valence band played the role of the initial state ψ_i at each k-point in the Brillouin Zone.

In Table 2.1 we present band gaps at both the experimental lattice constant and that derived from total energy minimization (we refer to this as the theoretical lattice constant). We use the latter lattice constant in the figures displaying the band structures. For GeC and SiGe which do not occur in the zinc-blende structure the lattice constant labeled "experimental" is the average of a_1 and a_2, the experimental lattice constants of the elemental crystals. We used a plane wave basis with a cut-off

Table 2.1: Minimum band gaps as obtained from the present GDFT/LDA calculations, compared to experiment and GW theory. For each material we give the experimental lattice constant and the theoretical one, derived from minimization of the total energy, followed by the calculated minimum band gaps at both lattice constants. Experimental and GW values are taken from Ref. [77] and Ref. [147], respectively, except where other references are given.

Material	Latt. const. (Å)		Gap (eV)			
	α_{exp}	α_{theor}	$E_g(\alpha_{exp})$	$E_g(\alpha_{theor})$	Exp.	(GW)
Si	5.43	5.38	1.223	1.168	1.17	1.21[a]
C	3.57	3.55	4.718	4.748	5.48	5.43[a]
Ge	5.66	5.57	0.000	0.494	0.74	0.65[a]
SiC	4.36[d]	4.32	2.646	2.624	2.39	2.34[b]
SiGe	5.50	5.46	1.239	1.203		
GeC	4.45	4.50	2.808	2.818		
AlP	5.45	5.39	2.801	2.685	2.50	2.59
AlAs	5.62	5.59	2.573	2.543	2.32	2.18[c]
GaP	5.44	5.30	2.484	2.468	2.39	2.80[d]
GaAs	5.65	5.51	1.062	1.717	1.52	1.58[c]
AlN	4.37[e]	4.31	6.010	6.077		
GaN	4.69[e]	4.37	3.910	4.621	3.52[e]	
AlSb	6.13	6.06	1.956	2.009	1.68	1.64
GaSb	6.12	5.95	0.259	0.925	0.80	0.62
InP	5.87	5.66	1.804	2.550	1.42	1.44
InAs	6.04	5.85	0.259	1.396	0.41	0.31
InSb	6.48	6.28	0.000	0.996	0.23	0.08

[a]: Ref. [45, 46] [b]: Ref. [111] [c]: Ref. [33, 34] [d]: Ref. [36] [e]: Ref. [124]

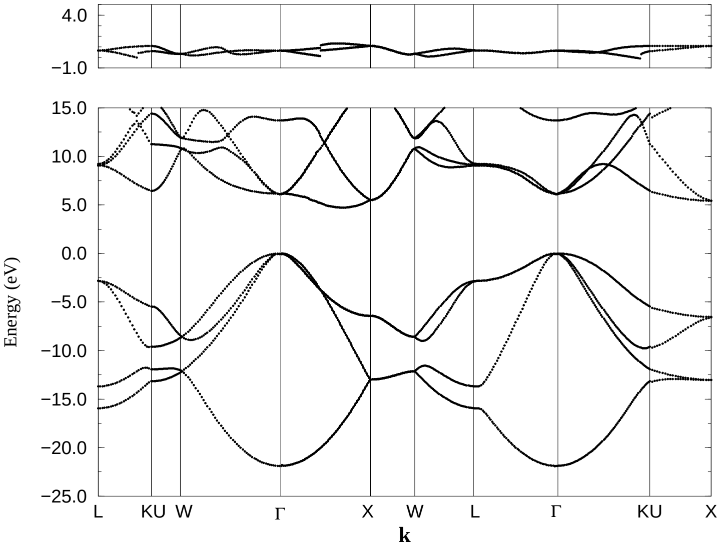

Figure 2.2: Same as figure 2.1 for C.

of 24 Ry, except for C, SiC and GeC (60 Ry) and AlN and GaN (70 Ry). A grid of $8 \times 8 \times 8$ **k** points was used in the full Brillouin zone, reduced to a smaller set according to the symmetry of the crystal.

We calculated the band structure of seventeen semiconductors and insulators in the zinc-blende or diamond lattice structure which we discuss in groups below.

Elemental group-IV semiconductors: The theory works essentially perfectly for Si, where the gap is the same with the experimental value for the theoretical lattice constant and is off by 4.5 % at the experimental lattice constant. For diamond the gap is off by 15%. For germanium, at the experimental lattice constant the method gives a zero gap, but the situation is better at the theoretical lattice constant, where the gap is off by 32%. We give the explicit band structures of Si and C in Figures 2.1 and 2.2 as examples.

For both Si and C the band gap is indirect, occurring between Γ, (the valence band maximum -VBM- as in all the semiconductors we considered) and a point along the ΓX line (the conduction band minimum -CBM). For Ge the gap is direct.

Comparing these results with those from the work of Fritsche and Gu [31], which use a model correlation factor for ε_{xc} rather than a local approximation, we see that these authors achieved a better result for the band gap of C; we believe this difference is due to the small size of the core in C which results in larger density

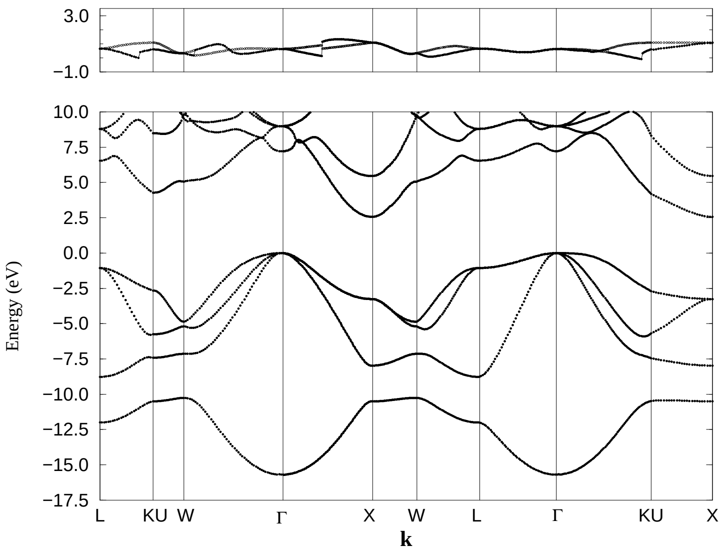

Figure 2.3: Same as figure 2.1 for SiC.

gradients, making the local approximation employed here less accurate.

Compound group-IV semiconductors: Results in good agreement with experiment are also obtained for SiC, where the gap is off by 9%. It is interesting that the error in SiC is close to the average of the percentage errors for Si and C. This leads us to believe that the gap values for the other two mixed group-IV materials (SiGe and GeC), if they could be synthesized in the zinc-blende structure, would be correct to about 20%. We give the explicit band structure of SiC in Fig. 2.3 as an example.

The minimum gap is indirect for SiC, SiGe and GeC with the CBM occurring at X for SiC and GeC, and along ΓX for SiGe.

Common Polar III-V semiconductors: We performed calculations for almost all polar III-V semiconductors which are shown in Table 2.1 in the order they have in the periodic table. For Al-compounds and GaAs we obtained good results within about 10 % of experiment. For GaP the error is only 3 % . We give the explicit band structure of GaAs in Fig. 2.4 as example.

For AlP and AlAs the gap is indirect with the CBM at X. GaAs has a direct gap. For GaP we found an indirect gap with CBM along ΓX at the theoretical lattice constant, while the same material at the experimental lattice constant has a direct gap.

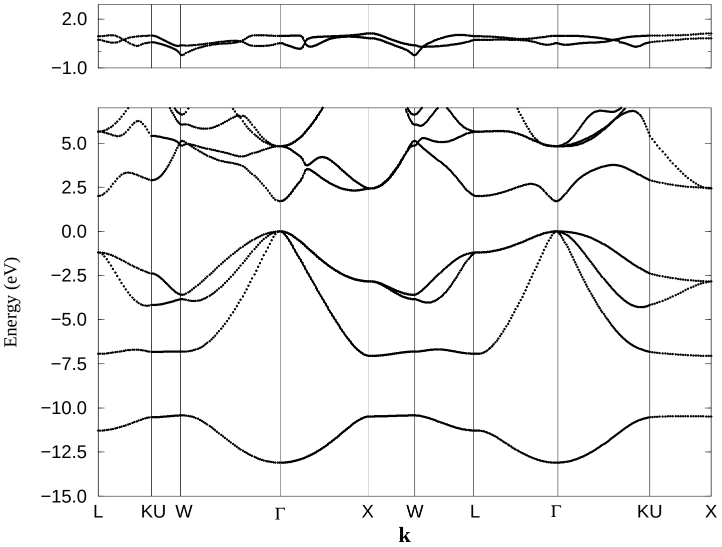

Figure 2.4: Same as figure 2.1 for GaAs.

Group III–nitride wide gap semiconductors: Recently much attention has been focused on III-V materials with N as the group-V element, which are wide gap semiconductors with possible applications in optoelectronics. These materials appear both in the wurtzite and the zincblende (metastable) structures. In Figs. 2.5 and 2.6 we give the band structures for AlN and GaN as obtained from the present calculations for the zincblende structure. For AlN, where we were not able to find experimental data for the zincblende structure, we estimate the band gap we calculated should off the experimental value by about 10 %.

GaN was found to have a direct gap at the theoretical lattice constant and an indirect gap at the experimental lattice constant whith the CBM occurring along ΓX but very close to Γ. AlN has an indirect minimum gap whith the CBM at X.

Compound III-V semiconductors with fifth row elements: The gap values we obtained for III-V semiconductors involving the fifth row elements In and Sb are not as satisfactory. We believe the neglect of spin-orbit effects is partially responsible for these poor results. Apparently, relativistic effects are important when studying the electronic behavior of heavier elements like In and Sb. The results are better for III-Sb 's because due to the polar bond, the Sb core is screened; for the same reason, results are particularly poor for compounds containing In.

All these materials were found to have a direct minimum gap, except AlSb

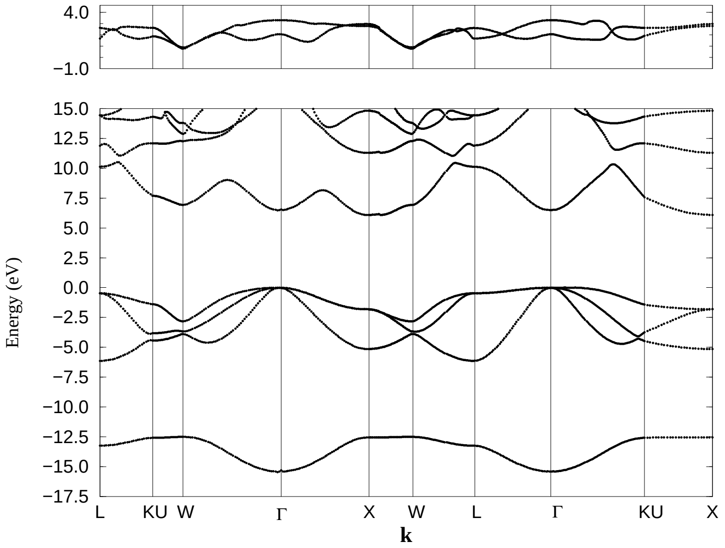

Figure 2.5: Same as figure 2.1 for AlN.

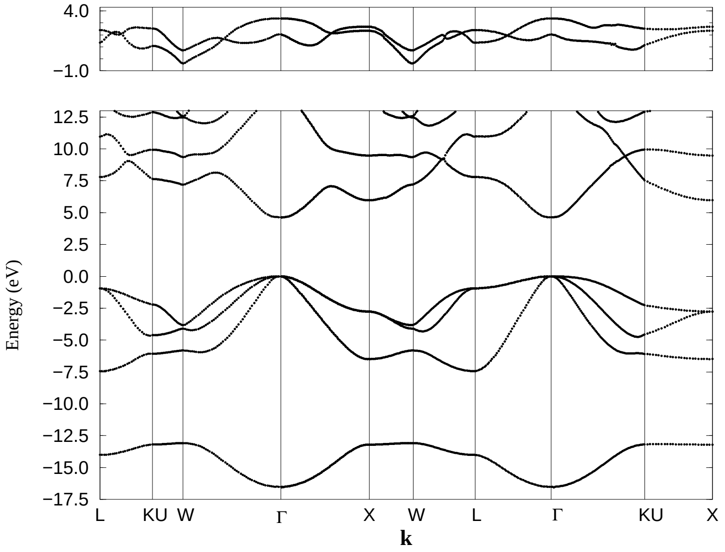

Figure 2.6: Same as figure 2.1 for GaN.

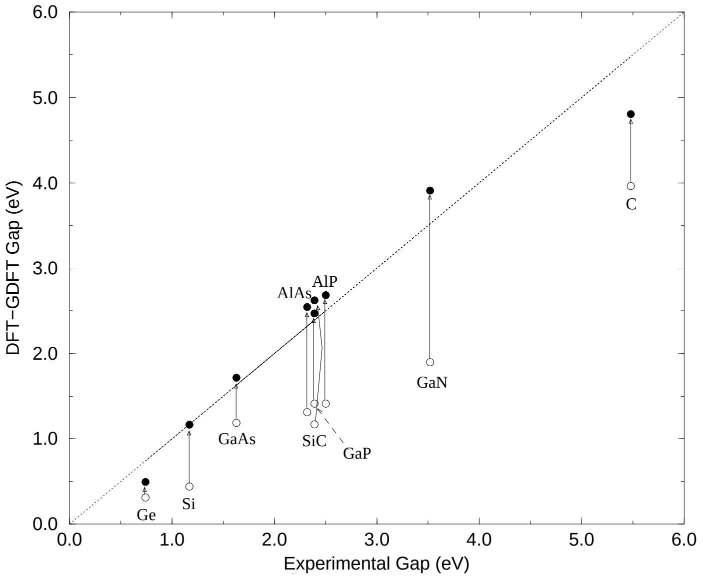

Figure 2.7: DFT (open circles) and GDFT (filled circles) band gap vs the experimental value for several semiconductors in the zinc-blende structure.

where the CBM occurs along the ΓX line.

Statistical data: For the six materials for which we give the band structures (Fig. 1 - 6), the correction shows similar behavior: The mean value, $\langle \Delta_{fi} \rangle$ is about 36% of the energy gap and has a fluctuation of about 33% around its mean value.

Δ_{fi} is positive for the first conduction band, except in some cases (C, GaN) around the point W. In particular, Δ_{fi} is positive for all materials in the region Γ to X, which determines the minimum band gap. Accordingly, the minimum DFT/LDA band gap is increased in all cases, by about 40% on average. This correction can not be treated as a constant, since it has large fluctuations (see Fig. 1 - 6), especially for the two nitrides (see Fig. 5 and 6).

2.3 Conclusions

In summary, GDFT/LDA/pseudopotential calculations can be used to derive reasonable band structures for elements in intermediate rows of the periodic table like Si, AlP, AlAs, GaAs etc. The success of the method is obvious from Fig. 2.7 where theoretical band gaps are plotted vs. the experimental values. The arrows show the correction to the DFT values and clearly most points move close to the "exact theory" line when the GDFT correction is applied. We excluded from this figure the case of compound III-V semiconductors which involve fifth row elements (In and Sb), since the neglect of spin-orbit coupling in the present work gives considerably poorer results for those materials. In the same figure the experimental lattice constant is used for GaN since the theoretical one is off by more than 10%, which is significantly worse than the rest.

We suggest that the simplicity of the method, which is based on the well-known DFT/LDA scheme, its physical clarity and the relatively small computational effort it requires, render it a useful tool for reasonably reliable band structure calculations. We believe this work demonstrates that the well studied DFT/LDA/pseudopotential scheme can give results comparable to more rigorous methods, at least for materials containing third and fourth row elements. For other cases, qualitative results can be obtained. Since the correction to the band structure is not constant as a function of $\mathbf{k}$, as the upper panels in Fig. 1 - 6 demonstrate, this theory appears to be more realistic than a "scissor operator" which is often used as an *ad hoc* fix of DFT/LDA band structure calculations. Nevertheless, the method does involve several approximations as discussed in Section 2.1.3, some of which cannot be rigorously justified. As such it cannot be considered a substitute for more rigorous exact treatments, like GW theory.

Chapter 3

The (100) surface of Silicon

We perform an extensive comparative study of known reconstructions of Si(100), a system of continuing technological and scientific interest. We focus on the atomistic features of the surface and discuss its microscopic properties, derived from a first-principles method, in terms of fundamental physical and chemical concepts. Our study includes a detailed analysis of the atomic geometries, the relative energies of the various structures, and the nature of the surface electronic states. The latter are explored through contour plots of the charge density and wave functions, simulated STM images and band structures. We compare our results to other ab initio *calculations and experiment, and discuss the nature of any discrepancies.*

The reconstruction of Si(100) is perhaps the most studied problem in surface physics. It is the surface mostly used in technological applications, a representative among them example being Metal-Oxide-Semiconductor (MOS) transistors, which are the structural units of most modern electronic devices [22]. The main reason for the wide success of Si(100) as a substrate for growth of such devices is the smooth (100) interface between Si and its oxide, SiO_2, as well as the intermediate lattice constant of Si (5.43 Å) which makes it possible to grow epitaxially a broad range of materials on top of it. Most modern integrated circuits, based on Complimentary-MOS (CMOS) technology, were p-MOS and n-MOS are grown on the same substrate, are built on a Si(100) wafer [125].

The simplicity of Si(100) surface structure compared to reconstructions of other solid surfaces, makes it ideal for studying many different, fundamental or applied, concepts of surface physics, chemistry and materials science. From nano- to micro-scale, the Si(100) surface exhibits a rich variety of interesting behavior: macroscopic strain fields result in surface roughening, step mobility and pattern formation, while all these effects are combined with microscopic rearrangements, charge transfer, re-hybridization and rebonding of atoms.

Almost half a century after the first experiment [117, 118] revealing the atomistic structure of Ge and Si(100), this system still challenges scientists coming from different disciplines to explore its unique characteristics. Experiments and theoretical models have been revealing new aspects and novel characteristics of this surface continuously over the years. This progress was revolutionized by a number of novel experimental techniques, such as the achievement of Ultra High Vacua (UHV) and the invention of Scanning Tunneling Microscope [6] (STM). Theory has also made significant contribution towards understanding the physics of this surface, especially through the use of Density Functional Theory [44, 66] (DFT), which, combined with efficient algorithms [12, 82], has made possible the *ab initio* treatment of extremely large systems.

In this work, we apply HARES (Harvard Adaptive Real-space Electronic Structure) in a comparative study of most known reconstructions of Si(100). In this electronic structure approach a finite (curvilinear, in general) grid is used for representing the charge density and the Kohn-Sham wave-functions, and a real-space integration of the quasi-particle Schrödinger equation is performed. This method has already proven successful for a wide variety of systems [138]. We performed calculations for almost all known surface reconstructions of the Si(100), including (2×1), (2×2), $p(2 \times 2)$, $c(2 \times 2)$, $c(4 \times 2)$, $c(4 \times 4)$, plus a missing dimer model with $c(4 \times 4)$ periodicity. We investigate geometrical properties, (bond lengths and angles) as well as electronic properties (surface band gaps and band structures), and we construct simulations of STM images for direct comparison to the experiment. Our study provides a detailed and comprehensive picture for this surface and reveals some new insights, different or complimentary to the results of previous investigations. We pay particular attention to these points and their role in interpreting the experimental results of Si(100).

3.1 The reconstructions of Si(100)

3.1.1 Reconstruction and its notation

Atoms near surfaces of solid materials usually change their positions compared to the corresponding atoms in the bulk in order to lower the energy of the system. The main reason for that is the dangling (broken) bonds of surface atoms; the coordination number of surface atoms on a bulk-terminated plane is always smaller than that of an atom in the bulk. This change usually affects not only the topmost layer, but also a few subsurface layers.

The usually more open-structured covalently bonded solids undergo in most cases a *surface reconstruction*: atoms near the surface move both perpendicular, and parallel to the surface plane, creating structures with lower symmetry than the crystal, thus enlarging the unit cell. The unit cell of the reconstructed surface is traditionally described by means of the relation of their lattice vectors to those of the bulk crystal plane. If the latter are $\mathbf{a}$ and $\mathbf{b}$, and the new vectors are $\alpha\mathbf{a}$ and $\beta\mathbf{b}$, the reconstruction is called $(\alpha \times \beta)$. A $R\phi$ in the end denotes that the new lattice vectors have an angle ϕ with the old ones. For the special case where ϕ equals half the angle of $\mathbf{a}$ and $\mathbf{b}$, the reconstruction is called "centered"; for example the $c(4 \times 4)$ periodicity is the same as the $(2\sqrt{2} \times 2\sqrt{2})R45^\circ$.

3.1.2 The dimer reconstruction of Si(100)

Fig. 3.1 shows top and side views of the ideal Si(100), i.e. the surface produced by an "ideal" cleavage of the Si crystal perpendicular to the [100] direction. Each surface atom is two-fold coordinated, possessing two dangling bonds. If one assumes that surface atoms remain in the bulk-like sp^3 hybridization, each of them will have two dangling orbitals, pointing diagonally up-left and up-right in the lower right panel of Fig. 3.1.

Another case, for which one can argue it lowers the total energy, arises if we consider unhybridized surface atoms, with one s and one p orbital, the latter pointing towards neighboring left and right atoms in the lower left panel of Fig. 3.1. In this

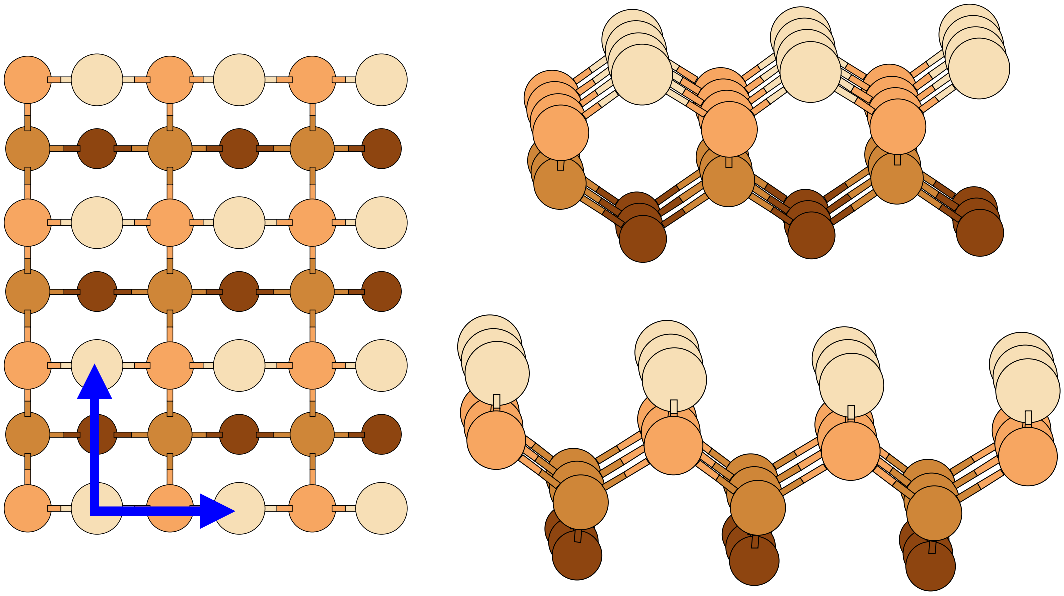

Figure 3.1: A diamond-structure crystal cut parallel to the (100) plane: Top view (left), side views (right). The lattice vectors vertical to [100] are shown.

case, a relaxation of the topmost layer is expected, so that the bonds of a surface atom with second-layer atoms form angles of 90°, appropriate for p orbitals. At the same time a weak bond will be formed between atoms lying in the same row and having their p orbitals pointing towards each other. But this bond will be very weak since its length is much larger than the bulk bond length.

In order to form bonds of the desired length, atoms have, in addition to the relaxation mentioned before, to come closer to each other. In the lower left panel of Fig. 3.1, pairing would happen between the two surface atoms on the left as well as the two on the right. These pairs of atoms are usually called surface *dimers*, and they were proposed by Schlier and Farnsworth [117], to explain their observation of a 2×1 periodicity on Ge(100).

The surface atoms have to come closer because their distance of 3.84 Å is significantly larger than the bulk bond length, which equals 2.35 Å . If this distance was closer to the bulk bond length, the atoms would maybe prefer not to move, in order to take advantage of several bonds (four in this case), one with each neighboring surface atom. If this was the case, a slight motion in the [100] direction would be sufficient to bring the bond angles and lengths close to the preferred values for the particular atomic electronic structure; this is usually the case in surfaces of metallic or ionic solids. This example demonstrates why *reconstruction* instead of *relaxation* is expected in the open, covalently-bonded, semiconducting structures. The only

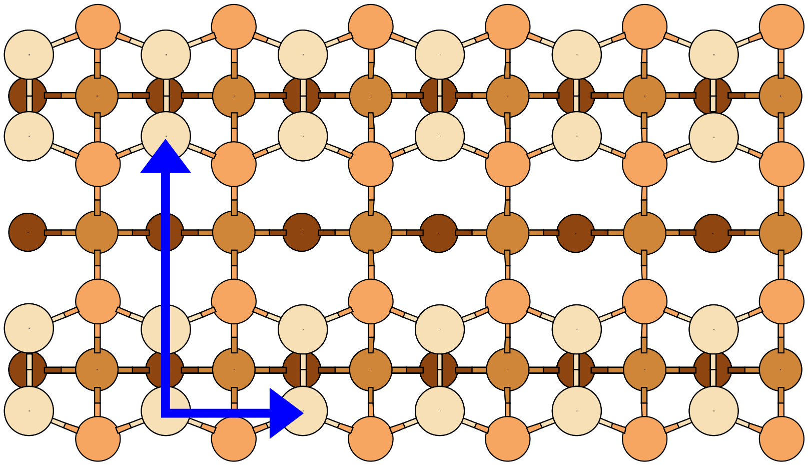

Figure 3.2: Relaxed geometry (top four layers) of the symmetric dimer (2 × 1). Higher atoms are plotted with larger spheres of lighter color. The arrows represent the lattice vectors.

mechanism to have a surface with bulk-like 1×1 reconstruction is via the adsorption of valence-mending adsorbates, which will cover the surface and bond to the topmost semiconductor atoms [57].

Although the dimer idea may sound simple, it was just one among a vast variety of models for Si(100). Simple tight-binding arguments suggested that other structures, most of them including vacancies and/or adatoms, would give lower energy. In his excellent classical textbook, Harrison [40] gives a detailed discussion of various models of Si(100), noting that "[dimer reconstruction] seems unlikely that is favorable".

The conflict was resolved in mid-80s in favor of the dimer models. This progress was pushed mainly by two factors: First, the invention of Scanning Tunneling Microscope [6] (STM), which produced real-space images of surfaces with atomic resolution. Second, the improvement of theoretical tools, as well as computer hardware and software, which made it possible to have *ab initio* energetics for systems as large as those under study.

We are not discussing any of these non-dimer models in this work; an excellent review of the pre-STM era of Si(100) modeling can be found in the book of Dąbrowski and Müssig [22].

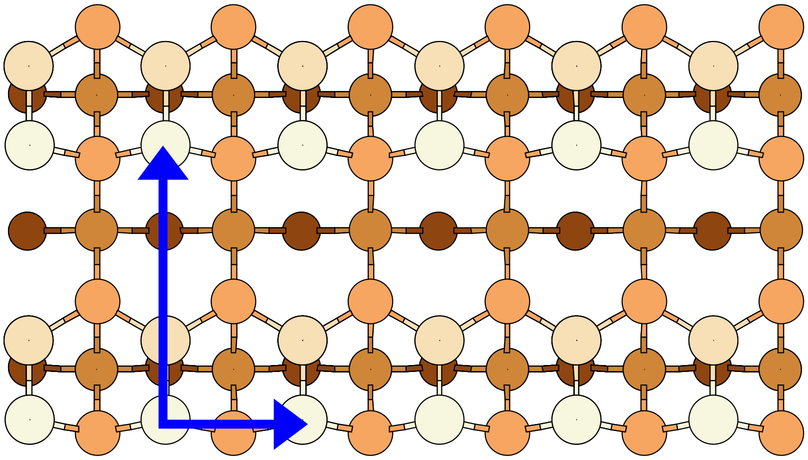

Figure 3.3: Same as Fig. 3.2 for the asymmetric (2×1).

3.1.3 The cases considered

We considered 7 different reconstructions for the system under consideration: (2×1) symmetric, (2×1) asymmetric, $p(2 \times 2)$, $c(4 \times 2)$, $c(2 \times 2)$, $c(4 \times 4)$, and a $c(4 \times 4)$ cell with a missing dimer.

The symmetric dimer (2×1) reconstruction of Si(100), mentioned in the previous section, is shown in Fig. 3.2. This is the fundamental starting point for studying all features of this surface. All other considered cases are constructed either by varying the position of the two dimer atoms or by assuming more complicated arrangements of dimers.

The tilted dimer, sometimes called also buckled dimer, was introduced to resolve the conflict between theory and experiment about the surface band-structure. Theoretical calculations on the symmetric (2×1) predict a metallic behavior (see Sec. 3.7), while experiments show that Si(100) is semiconducting [43]. A band gap opens up when tilted dimers are considered [15]. The periodic arrangement of tilted dimers in the (2×1) periodicity, is shown in Fig. 3.3. This model has the advantage of capturing the essential features of dimer tilting, within the (2×1) periodicity. We also relaxed this structure in a (2×2) supercell, to capture possible twisted-dimer effects. We did not find any significant difference between the two cases.

Once tilted dimers are considered as the building blocks of Si(100), there are many possibilities for their arrangement. Assuming correlations between neighboring dimers, we naturally arrive to the next two alternative-tilting-angle cases: In $p(2 \times 2)$, shown in Fig. 3.4, neighboring dimers of the same dimer row have opposite tilting directions, but dimers in neighboring dimer rows tilt towards the same direction. In

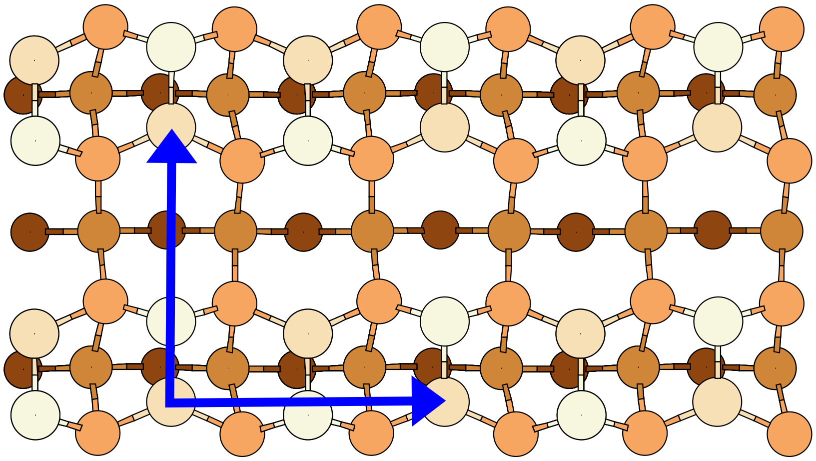

Figure 3.4: Same as Fig. 3.2 for $p(2 \times 2)$.

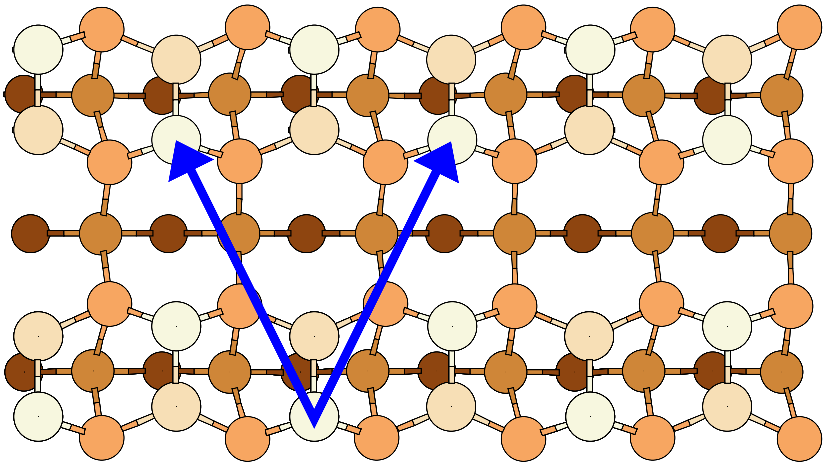

Figure 3.5: Same as Fig. 3.2 for $c(4 \times 2)$.

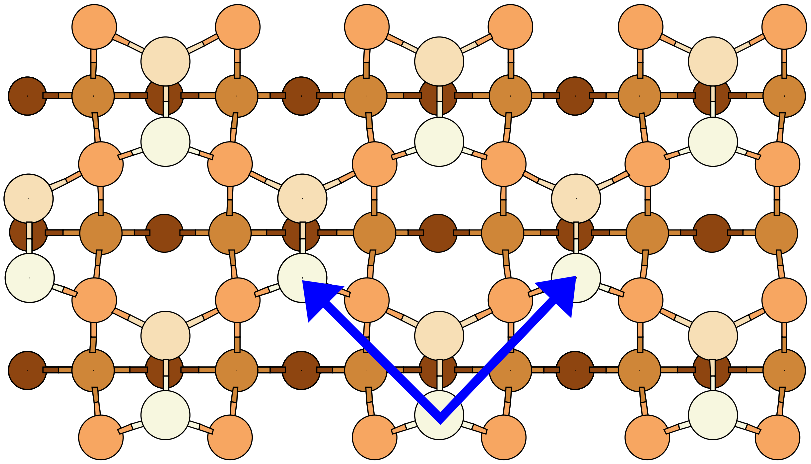

Figure 3.6: Same as Fig. 3.2 for $c(2 \times 2)$.

$c(4 \times 2)$, shown in Fig. 3.5, all four nearest-neighboring dimers of a given one are tilted in the opposite direction. As we will discuss in Section 3.4, this is the lowest energy structure for the system.

The $c(2 \times 2)$ structure, shown in Fig. 3.6, is probably the subject of a theoretical study for the first time. The idea for this pattern comes from the dimerization model, together with a trend to stretch the tetrahedral angles of the second layer atoms as little as possible. The cost of largely stretched torsion (3-bond or 4-atom) angles should not be neglected, but is less costly energetically. Similar local structures, with some dimers moving off the dimer row, has been observed in InSb(100) [4].

A possibility for a drastic local reduction of dangling bonds can be a missing dimer, as suggested by Pandey [95]. All four second-layer atoms around the defect are four-fold coordinated, thus locally there are two less dangling bonds. Since we are restricted to periodic structures, we choose to use a $c(4 \times 4)$ supercell to study the missing dimer defect. This supercell is shown in Fig. 3.7. In all supercell studies of defects, the main issue is to minimize interaction between a defect and its periodic image. In the periodicity we choose, there are three dimers separating subsequent vacancies in the same row. In addition, the supercell was chosen to be centered so that defects do not lie at the same column as it would be the case if we used any non-centered supercell. To obtain a reliable vacancy formation energy, we also studied a perfect $c(4 \times 4)$. In this case, the lattice vectors are those shown in Fig. 3.7, while the atomic arrangement looks the same as in $p(2 \times 2)$, shown in Fig. 3.4.

Structures with isolated large columns of missing dimers have been observed recently. They have been given the name $(2 \times n)$ reconstruction, with $n >> 1$

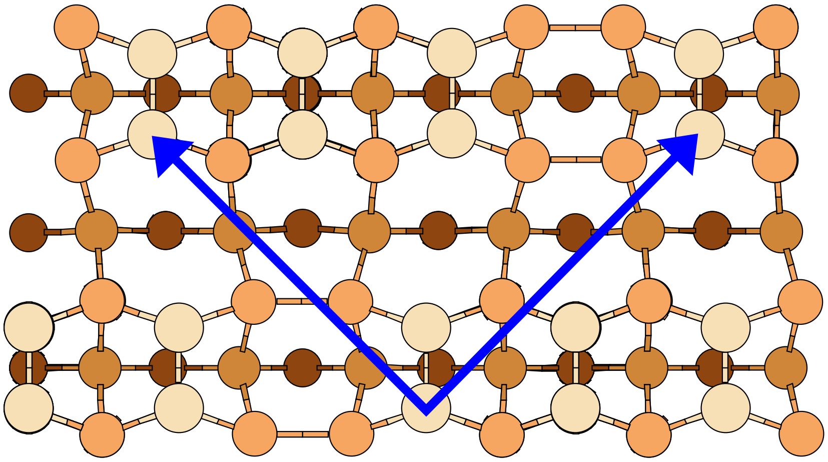

Figure 3.7: The supercell of $c(4 \times 4)$ periodicity used to study the missing dimer case. Notation as in Fig. 3.2.

being the distance between subsequent columns. It seems that those structures are important metastable states of Si(100) in the path to step formation and/or step evolution. We discuss neither such structures nor steps in the present work, as we focus on the microscopic aspects of the reconstruction.

Fig. 3.8 summarizes all the considered structures in a schematic plot. We use line segments and arrows to represent symmetric and tilted dimers, respectively.

3.2 The method

We use Density-Functional Theory (DFT) in the Local Density Approximation (LDA) [44, 66]. The Kohn-Sham valence electron wavefunctions are represented in a real-space orthogonal grid with a spacing of 0.22 Å, which is equivalent to a cut-off energy of 48Ry in a plane-wave basis calculation[1]. The ionic cores and their interaction with valence electrons were taken into account through the soft Troullier-Martins [134] pseudopotentials, in the separable Kleinman-Bylander form [65]. The Laplacian is expanded up to second order terms. For the exchange-correlation functional we use the results of Ceperley and Alder as they have been parametrized by Perdew and Zunger [13].

The system was modeled by a periodic slab geometry consisting of 7 layers of Si plus a terminating layer of H in one side. The bottom Si layer is kept frozen to

---

[1] The effective cut-off for each direction is calculated from $E_C = \frac{\hbar^2 \pi^2 n^2}{2 m_e L^2}$, where L is the length of the simulation cell and n the number of grid points.

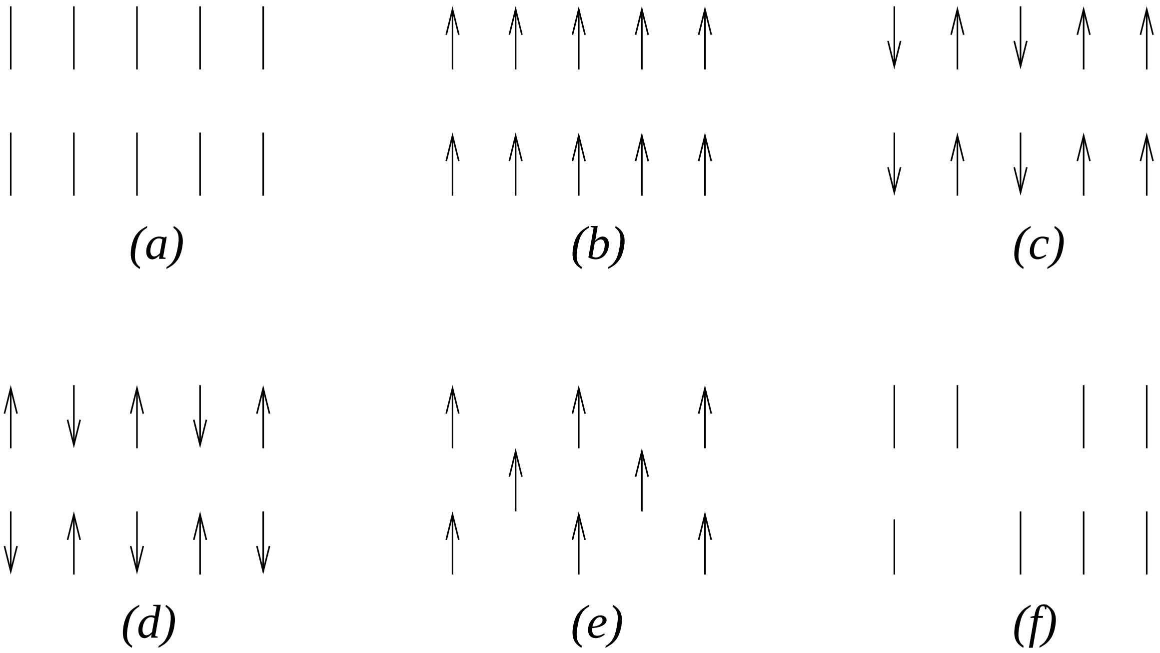

Figure 3.8: Schematic graph of the dimer reconstruction family. Each line represents a dimer; an arrow represents a tilted dimer, with its higher atom at the arrow head. a: (2×1) symmetric; b: (2×1) asymmetric; c: $p(2 \times 2)$ or $c(4 \times 4)$; d: $c(4 \times 2)$; e: $c(2 \times 2)$; f: $c(4 \times 4)$ with a dimer vacancy.

the bulk positions. Subsequent slabs are separated by roughly 8 Å of vacuum. The Brillouin Zone was sampled by a grid of 4×4 **k**-points of the Monkhorst-Pack type [85] for the (1×1) surface unit cell, reduced to a smaller set in bigger cells keeping the spacing of the grid constant. For example, a 2×4 grid was used for the 2×1 cell.

The atomic degrees of freedom are relaxed with the Broyden-Fletcher-Goldfarb-Shanno (BFGS) method [17, 120] until the Hellman-Feynman forces were smaller than 0.001 a.u.

All the previous parameters have been checked, within either the present or previous works [82, 138], to give well-converged results.

For our convenience, we used only orthogonal unit cells; in the case of $c(4 \times 2)$ a (4×2) cell was used with $c(4 \times 2)$ symmetry imposed on the ionic forces.

To account for the inadequacy of DFT to give reliable excitation spectra in semiconducting systems, we apply a correction formula to the energies of the excited states derived from the Generalized Density Functional Theory (GDFT) [27, 28, 29]. This method has proven very efficient for a variety of semiconducting systems [108]. For materials containing atoms in intermediate rows of the periodic table (like Si or

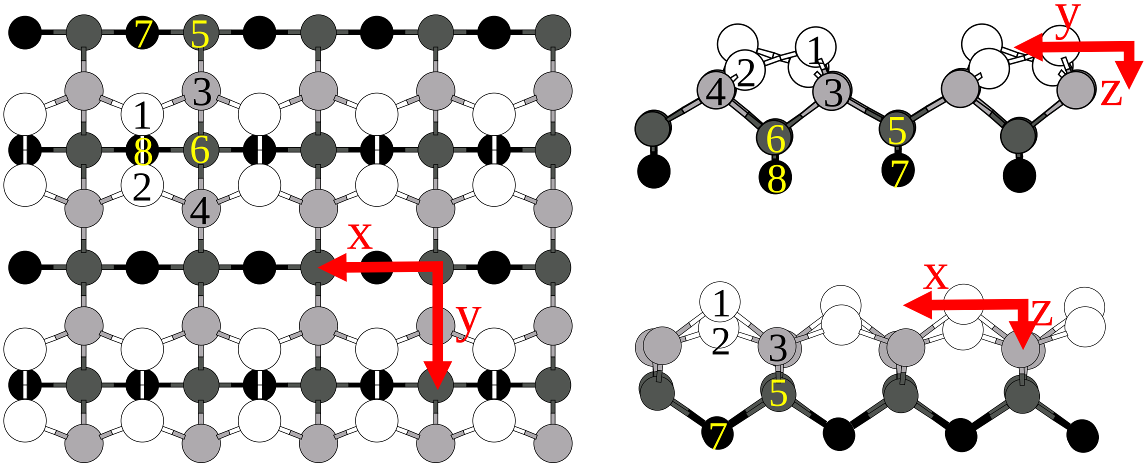

Figure 3.9: Definition of axes and atomic positions used in Table III. We used same notation as in Ref. [94]. The side views resemble the $p(2 \times 2)$ reconstruction.

GaAs), the agreement with experiment is excellent, while the band gaps for materials containing much smaller (like diamond) or larger (like InSb) agree with experiment within 10% or better.

As a first test to the method described before, we calculated the properties of bulk Si, using an orthogonal 12-atom cell, consisting of 12 (1×1) (100) atomic layers. We choose this particular cell because it compares directly to those used for studying the surface, so we could calculate bulk properties using exactly same **k**-points, real-space grid points, etc. We found a lattice constant of 5.40 Å, which is 0.6% off the experimental value (5.43 Å). Therefore we decided to use the experimental lattice constant in the following calculations. The minimum band gap was 1.03 eV, 10% smaller than the experimental value of 1.12 eV. The gap is indirect, with the valence band maximum (VBM) at Γ (0,0,0) and the conduction band minimum (CBM) at $K(\frac{1}{2}, \frac{1}{2}, 0)$, which corresponds to the X(1,0,0) point of the FCC Brillouin zone. The experimental position of the CBM is close to X, at 0.75 of the line ΓX.

3.3 Geometrical features

The coordinates of atoms around the dimer for the lowest energy reconstructions, $c(4 \times 2)$ and $p(2 \times 2)$, as well as for the proposed $c(2 \times 2)$ cell are listed in Table 3.1, compared to experiments and similar *ab initio* approaches based on a plane wave expansion of the wave function and solution of the corresponding secular equation. We followed the numbering of atoms and definition of the coordinate system used by Over *et al.* [94]. The notation is explained in Fig. 3.9.

Table 3.1: Coordinates of atoms in the present calculation (HARES) around a dimer compared to a plane-wave calculation (PW) and experiment (Exp.). In the PW and HARES columns, (a) is $c(4 \times 2)$, (b) is $p(2 \times 2)$, and (c) is $c(2 \times 2)$. In the experiment column, (a) is LEED [94] and (b) is XRD [126]. The numbering of atoms and the choice of axis is explained in Fig. 3.9. x and y are in units of $a\frac{\sqrt{2}}{2}$ while z in units of $\frac{a}{4}$, a=5.43 Å being the lattice constant.

#	x			y			z		
	PW	HARES	Exp.	PW	HARES	Exp.	PW	HARES	Exp.
1a	0.50	0.50	0.50	0.68	0.68	0.68	0.00	0.00	0.00
1b	0.50	0.50	0.50	0.68	0.66	0.66	0.00	0.00	0.00
1c		0.50			0.67			0.00	
2a	0.50	0.50	0.50	1.24	1.25	1.25	0.55	0.58	0.54
2b	0.50	0.50	0.50	1.24	1.25	1.24	0.55	0.56	0.64
2c		0.50			1.25			0.51	
3a	0.00	0.02	0.00	0.53	0.51	0.55	1.03	1.05	1.08
3b	0.03	0.02	0.00	0.53	0.51	0.50	1.02	1.06	1.52
3c		0.02			0.51			1.05	
4a	-0.03	-0.03	0.00	1.47	1.48	1.46	1.03	1.10	1.08
4b	-0.03	0.03	0.00	1.47	1.47	1.46	1.02	1.13	1.45
4c		-0.03			1.51			1.05	
5a	0.00	-0.10	0.00	1.00	1.00	1.00	2.13	2.17	2.25
5b	0.00	-0.08	0.00	1.00	1.00	1.00	2.12	2.22	2.55
5c		-0.03			1.00			2.09	
6a	0.01	-0.03	0.00	0.00	0.00	0.00	1.92	2.00	1.99
6b	0.00	-0.02	0.00	0.00	0.00	0.00	1.91	2.04	2.40
6c		0.02			0.00			2.09	
7a	0.50	0.40	0.50	1.00	1.00	1.00	3.08	3.17	3.22
7b	0.50	0.42	0.50	1.00	1.00	1.00	3.06	3.22	3.30
7c		0.50			1.00			3.03	
7a	0.50	0.46	0.50	0.00	0.00	0.00	2.95	3.04	3.03
7b	0.50	0.47	0.50	-0.01	-0.01	0.00	2.92	3.08	3.40
7c		0.50			0.00			3.18	
9a	0.50	0.45	0.50	0.49	0.49	0.46	4.00	4.10	4.13
9b	0.50	0.47	0.50	0.48	0.50	0.48	3.97	4.14	4.10
9c		0.50			0.51			4.12	
10a	0.50	0.45	0.50	1.51	1.51	1.54	3.99	4.08	4.16
10b	0.50	0.47		1.50	1.52		3.97	4.14	
10c		0.50			1.49			4.12	

The z axis points towards the $[\bar{1}00]$ direction, with its zero at the topmost atom of the system. The other two axis are parallel to the [110] and $[\bar{1}10]$. The position of origin for x and y is taken to coincide with one of the third layer atoms lying in the middle of two dimer rows (see Fig. 3.9). Finally, the orientation of x and y is taken such as the xyz is a left-rotated coordinate system. The natural units of the system are chosen; for x and y they are the lengths of the lattice vectors in the (1×1) cell, namely $a\frac{\sqrt{2}}{2}$, while for z it is the distance between two subsequent (100) planes in bulk Si, which is $\frac{a}{4}$. Thus in the absence of reconstruction, the x and y coordinates will be multiples of 0.5, while the z coordinates will be integers. The experimental values of the coordinates of atoms are usually obtained by fitting the structure factor of the system, which in turn is measured using diffraction, usually of either low-energy electrons (LEED) or X-Rays (XRD).

The results of Table 3.1 show that the reconstruction of the topmost layer causes atomic rearrangements even at the fourth layer below the surface. This is a consequence of the strong covalent bonds present in the system, which try to remain as close to the bulk values for lengths and angles as possible. In Table 3.1 we see that the fifth layer atoms are not close to the bulk positions, especially the z coordinates. This is a consequence of the particular choice of the origin (z=0 at the topmost atom of the system), which we made in order to direct compare our results with experiment.

The results for the geometrical characteristics are in excellent agreement with experiment. For instance, the z coordinates of all atoms in the $c(4 \times 2)$ reconstruction, which should compare to the experimental value since it is the lowest energy configuration, are described better by HARES than by previous plane wave calculations; the only exception is the z coordinate of atom 2. Overall, HARES gives better or equally good agreement with experimental values than plane wave methods in the $\frac{2}{3}$ of the values in Table 3.1.

The largest discrepancy between HARES and experiment is in the z coordinate of atom 2 (see also Fig. 3.9), which is found to be 7% higher than the XRD-measured value and 9% lower than the LEED-measured value. At the same time, our calculation agrees with both experiments for the x and y coordinates of the same atom. The z position of this atom is what determines the length of the dimer bond. The length of the dimer is one of the most important properties of Si(100), and will be discussed in detail below.

An interesting feature following the results of Table 3.1 is that the dimerization of the surface renders subsurface atoms to be nonequivalent. The third- and fourth-layer atoms that are below the dimer row (atoms 6 and 8 in Fig. 3.9) are slightly lower than the atoms lying between dimer rows (atoms 5 and 7 in Fig. 3.9). The height difference is 0.17 and 0.13 times $\frac{a}{4}$ =1.35 Å for third and fourth respectively. The effect is weaker for second and almost absent for fifth layer atoms.

The height difference has an important consequence in the bond lengths: The bonds formed by a third- or fourth- layer atom lying below a dimer row (atoms 6 or 8 in Fig. 3.9) are shorter compared to the bonds of an atom lying in the same layer but between dimer rows (atoms 5 and 7 in Fig. 3.9). The average difference between bond lengths is about 0.05 Å or 2%. This holds for all the reconstructions we considered, even for the symmetric dimer (2×1) reconstruction, and is thus a consequence of the dimerization of Si(100).

The existence of non-equivalent subsurface sites in Si(100) was first mentioned by Kelires and Tersoff [62]. It plays a very important role in alloyed-Si(100) as the sites under tensile stress (whose atoms form longer bonds) will be favored by the larger atoms of the alloy while sites under compressive stress will be favored by the smaller atoms of the alloy. This scheme explains the composition profile of $\mathrm{Si}_x\mathrm{Ge}_y\mathrm{C}_{1-x-y}$ alloy [60] and is responsible for the change of the reconstruction to $c(4 \times 4)$ and ordering phenomena in C-enriched Si(100) [109].

The dimer bond length and buckling angle, defined as the angle of the dimer line with the (100) plane, were found to have a weak dependence on the surface symmetry. These results are summarized in Table 3.2, compared with a plane wave calculation and various experiments. For the lowest energy structure, $c(4 \times 2)$, our calculation yields 2.38 Å and 20.8° for the dimer bond length and buckling angle, respectively, in excellent agreement with X-ray diffraction (XRD) measurements [126]. The experimental data agree about the buckling angle, but there is a broad range of values for the dimer length. Surface Core Level Spectroscopy (SCLS) [10] and Low Energy Electron Diffraction (LEED) [94] find this length to be around 2.25 Å, shorter than the bulk bond length, while XRD yields [126] that the dimer bond is slightly longer and identical to our result. Recently, in an XRD experiment, [26] an extra-long bond length of 2.64 Å was measured. Slab calculations based on plane wave-expansion yield lengths either shorter [105] or larger [122] than the bulk bond length of Si. We will come back to the dimer bond length in Section 3.5.

The lengths and angles of the back bonds between the dimer atoms and second layer atoms are shown in Table 3.3. The top atom of the dimer (atom 1 of Fig. 3.9) forms bonds ≈2% on average longer than the bulk bond length of Si (2.35 Å), these bonds forming an average angle of 94°. This value is clearly closer to 90° than to the tetrahedral angle (108.4°). In contrast, the lower dimer atom (atom 2 of Fig. 3.9) forms bonds slightly shorter than the bulk bond length, their angles being roughly 120°.

The characteristics of the bonds formed by the dimer atoms indicate a recon-

Table 3.2: Dimer bond lengths and buckling angles from HARES, plane wave calculations [105] (PW), and experiment. SCLS: Surface Core-Level Spectroscopy; LEED: Low Energy Electron Diffraction; XRD: X-ray Diffraction, LIS: Low-Energy Ion Scattering; TB: tight-binding, HF: Hartree-Fock.

cell	HARES		PW [105]	
	length	angle	length	angle
(2×1)	2.32 Å	0	2.23 Å	0
$(2 \times 1)a$	2.31 Å	17.3°	2.26 Å	18.3°
$p(2 \times 2)$	2.38 Å	18.7°	2.28 Å	19.1°
$c(2 \times 2)$	2.34 Å	17.2°		
$c(4 \times 2)$	2.38 Å	20.8°	2.29 Å	18.8°
$c(4 \times 4)$	2.36 Å	17.9°		
$c(4 \times 4)$v	2.27 Å	1.0°		

Exp., SCLS [10]	2.25 Å	19°
Exp., LEED [94]	2.24±0.08 Å	19±2°
Exp., LEED [143]	2.54±0.15 Å	XX±X°
Exp., XRD [126]	2.37±0.06 Å	20±3°
Exp., XRD [26]	2.64 Å	20°
Exp. LEIS [2]	2.41 Å	not measured
Theory, slab, PW [122]	2.38 Å	16.9°
Theory, slab, PW [88]	2.36 Å	
Theory, cluster, HF [123]	2.40 Å	0°
Theory, TB [75]	2.41 Å	9.1°

Table 3.3: Back-bond lengths (in Å) and angles (in °) for the lowest-energy reconstructions. For the dimer, see Table 3.2. Notation as in Fig. 3.9. c and p stand for $c(4 \times 2)$ and $p(2 \times 2)$, respectively.

bond lengths			bond angles		
1-3	c	2.41	3-1-3	c	97.5
	p	2.39,2.41		p	97.6
2-4	c	2.31,2.37	4-2-4	c	123.1
	p	2.32,2.34		p	121.1
			3-1-2	c	90.8, 92.4
				p	90.1, 91.45
			4-2-1	c	117.5, 116.3
				p	117.8, 117.2

struction driven re-hybridization of the surface-layer atoms. The bonds formed by the upper atom of the dimer indicate that it uses its p orbitals for bonding instead of the sp^3 hybrids used by bulk atoms, leading to the conclusion that it is in an unhybridized state. At the same time, the angles between the bonds formed by the lower atom of the dimer apparently show an sp^2 hybridized state for this atom.

Within the re-hybridization model, the two sp^3 dangling bonds per (2×1) cell of the ideal, bulk-terminated Si(100), discussed in Section 3.1.2, reduce to one p orbital (from the lowest atom) and one s orbital (from the topmost atom). It is then expected that the second will be occupied by two electrons and the first will be empty. Since dangling bonds have energies close to the Fermi level, we expect the highest occupied state to be a superposition of s orbitals centered at the higher dimer atoms. Similarly, we expect the lowest unoccupied state to be a superposition of p orbitals centered at the lowest dimer atom and pointing normally to the plane defined by the lower dimer atom and the second layer atoms connected to it, so that the axis of the p orbital makes an angle of about 20° with the [100] direction. We will explore this in the discussion of surface states in Section 3.6.

Considering the missing dimer case, we found almost flat dimers around the vacancy. The dimer bond length was found to be 2.27 Å. The back-bonds of a dimer atom with second-layer atoms were 2.42 Å, forming an angle of 123°, implying sp^2 hybridization and π-bonding for the dimer atoms. The back bond and the dimer bond form an almost tetrahedral angle of 108°. The second-layer atoms surrounding the missing dimer form three unstretched bonds with the neighboring dimer and their third-layer neighbors, and an elongated bond of 2.72 Å between themselves. All these bonds form angles close to the perfect tetrahedral angle (109.5°). In the calculation of Wang *et al.* [139], the re-bonded second-layer atoms were found to form a bond of 2.79 Å, in very good agreement with our calculation. In the same work, it is found that there are two types of dimer back bonds; the back-bonds with the exposed second-layer atoms have length 2.40 Å (which is in excellent agreement with our calculation), while the back-bonds with the other second layer atoms have length of 2.29 Å. Such a difference in bond lengths was not observed in our calculation. The discrepancy may be due to the different $((5 \times 2))$ supercell used in this work.

Finally, the results of Table 3.1 indicate that the different reconstructions, that is the different arrangements of dimers on the topmost layer, do not change much the displacements of atoms around each dimer. *The dominant effect of the Si(100) reconstruction is thus the dimerization of the surface layer.*

Table 3.4: Energy differences (in eV/dimer) for the considered reconstructions, compared with other calculations.

Energy difference	HARES	Other methods
$E_{(2\times1)a}$-$E_{(2\times1)s}$	-0.17	-0.12^a, -0.17^b
$E_{p(2\times2)}$-$E_{(2\times1)a}$	-0.05	-0.05^a, -0.09^b
$E_{c(4\times2)}$-$E_{p(2\times2)}$	-0.08	-0.003^a, -0.001^b
$E_{c(2\times2)}$-$E_{p(2\times2)}$	0.07	
$E_{c(4\times4),miss\ dimer}$-$E_{c(4\times4)}$	0.22	0.22^c

^{a}: Plane-wave calculation by Ramstad *et al.* [105]

^{b}: Plane-wave calculation by Inoue *et al.* [47].

^{c}: Plane-wave calculation by Wang *et al.* [139].

3.4 Energetics

There have been numerous experiments and theoretical models trying to answer the question weather the 2 × 1 reconstruction of Si(100) comes from symmetric or tilted dimers. An excellent review of this survey can be found in the book of Dąbrowski and Müssig [22]. Although a 2 × 1 periodicity of Si(100) was first observed 43 years ago [118], an undoubted proof that the ground state of Si(100) is an alternatively-tilted dimer state was given only a few years ago, when low-temperature STM experiments [140, 132] became possible.

Our results thus agree with the vast majority of recent experimental observations that the minimum energy structure is an antiferromagnetic-type arrangement of tilted dimers, namely a $c(4 \times 2)$ reconstruction. We find this case to be lower in energy by 0.30 eV/dimer compared to the symmetric-dimer (2×1) reconstruction. This number agrees well with 0.26 eV/dimer found by Inoue *et al.* [47] and 0.17 eV/dimer found by Ramstad *et al.* [105], both using a plane-wave expansion for the wave-functions.

The relative energies of the other considered structures are shown in Table 3.4. The present HARES calculation yields exactly the same ordering as the two other calculations mentioned before. We find the energy difference between the symmetric and asymmetric (2×1) to be 0.17 eV/dimer, identical to the result of Inoue *et al.* [47], and close to what the other calculation finds (0.12 eV/dimer). For the energy difference between asymmetric (2×1) and $p(2 \times 2)$ we find 0.05 eV/dimer, exactly the same value as Ramstad *et al.* [105]. The other plane-wave calculation [47] gives 0.09 eV/dimer.

The only discrepancy between this work and other *ab initio* calculations is in the difference between the energies of $c(4 \times 2)$ and $p(2 \times 2)$. In our calculation we find it to be 0.08 eV/dimer, which is an order of magnitude larger than what plane-wave calculations yield (0.001 [105] and 0.003 [47]). There are two factors that could account for the discussion for this discrepancy: First, we use a larger, orthogonal unit cell ((4×2)) to study the $c(4 \times 2)$ reconstruction, for the shake of convenience in the calculation as well as in the interpretation of our results. We imposed a $c(4 \times 2)$ periodicity in the atomic positions, but not in the wave functions, giving the system a chance to lower its total energy by a few meV's. Second, our method is different in nature than a plane-wave calculation, and the numerical wrap-around errors will be different. The numbers in Table 3.4 are differences of the total energies, which typically differ in their sixth digits.

Although there is no direct measurement of the energy difference between $c(4 \times 2)$ and $p(2 \times 2)$, we can derive an estimate for its order of magnitude from the STM experiments: The first low temperature STM experiment by Wolkow [140] took place at a temperature of 120K, where the thermal energy $k_B T \approx$0.01 eV. His observation that "$c(4 \times 2)$ ordering between the rows is more than five times more common than $p(2 \times 2)$" yields that the energy difference between the two phases should be greater than 0.016 eV, in agreement with our result of 0.08 eV. More recent experiments [146] show a complete absence of $p(2 \times 2)$ domains in defect-free Si(100) for temperatures between 6 and 80K, showing that the difference between the energy of $c(4 \times 2)$ and the energy of the next possible reconstruction cannot be less than 0.01 meV, as the plane wave calculations predict.

The vacancy formation energy was found to be 0.22 eV/(dimer vacancy), exactly the number reported by Wang *et al.* [139], although a different, 5×2, unit cell was used in that work. In Chapter 5, we calculate the dimer vacancy formation energy to be 0.25 eV/(dimer vacancy), using a completely different method. The surprisingly low formation energy of this defect was first predicted by Pandey [95]. Although the missing dimer causes long-range strain fields in the system, at the same time it reduces dramatically the number of dangling bonds from 2 to 0 at the missing dimer site and from 8 to 6 per $c(4 \times 4)$ cell. Because of this effect, missing dimers, also known as A-defects, are the most common imperfecture of Si(100).

We find the proposed $c(2 \times 2)$ structure to have a surprisingly low energy, only 0.07 eV/dimer above $p(2 \times 2)$ and 0.15 eV/dimer above $c(4 \times 2)$. This suggests that this structure should be observed at high temperatures. However, to our knowledge, there is no experiment reporting $c(2 \times 2)$ domains on Si(100); either long-range strain or kinetic processes forbid their appearance. The fact that the unoccupied dangling orbitals are equidistant gives this periodicity an easily recognizable pattern in e.g an

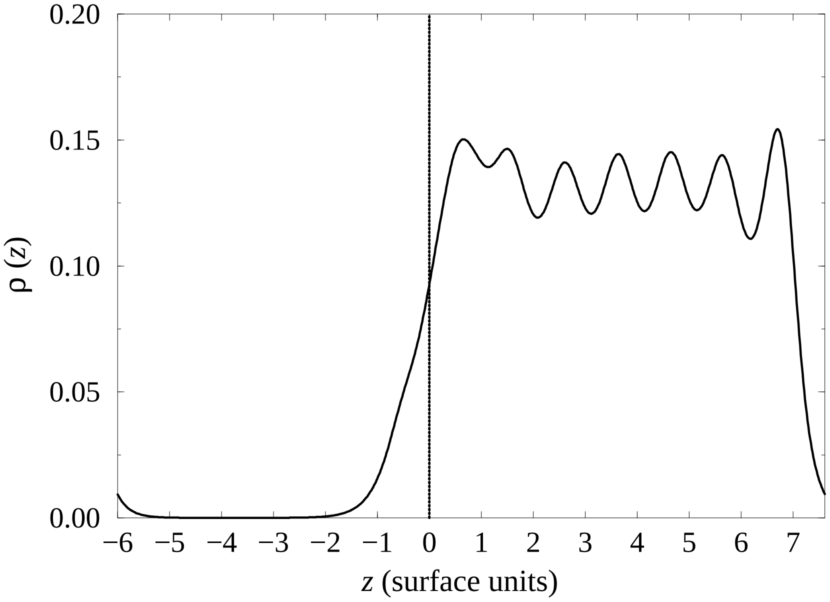

Figure 3.10: Average valence charge density as a function of height for the $c(4 \times 2)$ reconstruction. The vertical fainted lines denote average positions of ions in the first five layers. The fainted line corresponds to the z coordinate of the highest atom. The units for z are those used in Table 3.1, defined in Section 3.3.

STM or diffraction experiment or a chemisorption process.

3.5 Charge distribution

In Fig. 3.10 we plot the valence charge density for the $c(4 \times 2)$ reconstruction as a function of height. The height, z, is given in units of $\frac{a}{4}$, the spacing between (100) layers in bulk Si. The zero for z is taken as the position of the highest atom of the system, following the definitions of Section 3.3. A cubic spline was used to interpolate values of density between grid points (we use 5.7 grid points per layer on average).

The positions of the highest dimer atom is shown by a fainted line in Fig. 3.10. All (but the dimer) Si layers are located at the minima of ρ. This is characteristic of a valence charge density which can be thought as superposition of sp^3 atomic-like orbitals which are zero at the nuclei.

The last peak on the right comes from the $1s$ states of H atoms. In the framework of charge density, the H terminal layer is present in order to simulate the Si bond. We see the last minimum of $\rho(z)$ to be slightly deeper than the previous

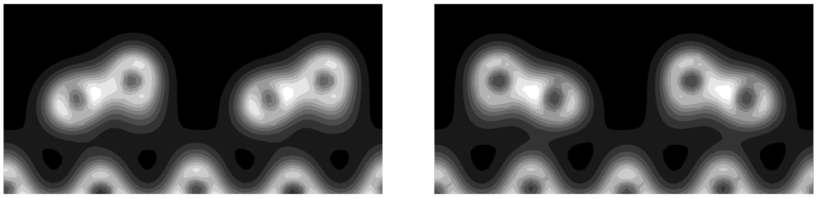

Figure 3.11: Representative charge density contour plots in a plane perpendicular to the surface, for $p(2 \times 2)$ (left) and $c(2 \times 2)$ (right).

two. Probably a H atom with atomic number slightly smaller than 1 would be more appropriate to simulate the bulk Si-Si bond, but this would destroy the *ab initio* character of the method.

This plot allows us to estimate the quality of the slab approximation we used. The vacuum we choose to separate subsequent slabs is thick enough, since there is a large area of zero charge above the surface. We take the vacuum to be about 6 layers thick; because of the tails of the surface wave functions, it turns out that the actual region of zero charge is roughly 3.5 layers thick. This amount is sufficient to ensure the absence of interaction between the surface under study and the H-terminated bottom of the slab. The 7 layers we chose for the slab thickness are also sufficient, since we observe the last two peaks to be identical. The presence of the surface affects the density up to $z \approx 3$, or the upper four layers. This result agrees to the conclusion of Section 3.3, that deviations from the bulk positions are important only for the first four layers.

In Fig. 3.11 we show two representative contour plots of the valence electronic charge density on a plane perpendicular to surface and containing the dimer. As was the case with geometrical features, the charge distribution around a dimer looks unaffected by the particular reconstruction, so the following discussion applies to all the considered cases.

As was mentioned in Section 3.3, the dimer reconstruction causes a re-hybridization of the dimer atoms. The upper dimer atom has a doubly occupied s orbital and three p orbitals used for bonding, resulting in the almost spherically symmetric distribution of charge around it shown in Fig. 3.11. The lower dimer atom is sp^2 hybridized, having an empty p orbital with its axis being perpendicular to the dimer; we indeed observe no charge near the lower dimer atom and along this axis in Fig.

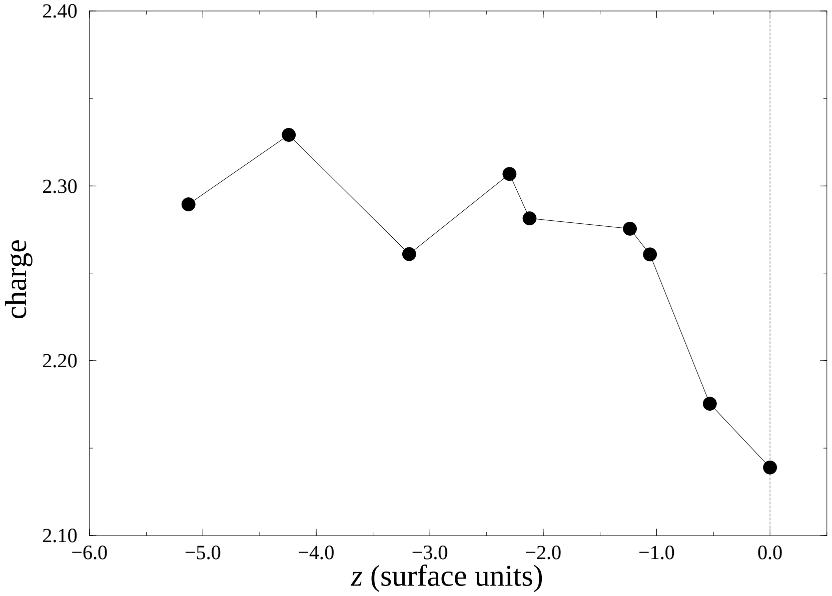

Figure 3.12: Charge density integrated around each atom on a sphere of radius half the average bond length, as a function of the atom height, for the $c(4 \times 2)$ reconstruction. Height z is defined in Table 3.1.

3.11.

In Fig. 3.11 the dimer bond appears to be polar, with the lower dimer atom attracting more charge around it. This seems to be in contrast with the model discussed before: The rehybridization discussed in Section 3.3 yields that the s orbital of the upper dimer atom is expected to be doubly occupied, and the p orbital of the lower atom is expected to be unoccupied. In this picture, the higher atom has 5 electrons around it and the lower atom 3, so the dimer bond should be polar, according to this hypothesis, with the bond charge maximum located near the upper atom. The reason for this discrepancy is energetical. The surface state has indeed the character of superposition of s orbitals centered at the highest atom, but this state is only one out of many (infinite for the real solid) which are bulk states with much lower energy. It is those states that are projected in the total density. The concentration of charge around the lowest atom forms a charged layer below the surface that ensures the long-range charge neutrality.

Insight in the charge distribution can be gained by looking into the total charge around each atom. It is defined as the integral of the charge density on the Wigner-Seitz cell around the atom of interest. In Fig. 3.12 we plot the charge around each atom averaged over atoms of the same height, as a function of height. In this figure, we approximate the Wigner-Seitz cell by a sphere of radius half the average bond length of each atom. This sphere is inscribed to the Wigner-Seitz cell, its volume being $\frac{\pi\sqrt{3}}{16}$ $\approx$0.34 of the available volume per atom in the ideal diamond crystal. We expect to capture the essential trends in the atomic charge by using this sphere, due to the directional character of the chemical bonds.

From the results of Fig. 3.12 we confirm the partially polar character of the dimer bond shown in the cross-section of the charge density shown in Fig. 3.11. The upper dimer atom has slightly less charge than the lower dimer atom, both of them having at the same time less charge around them than subsurface atoms. The second layer atoms have also a small difference in charge, the lower of the two, which is connected to the higher dimer atom, appearing to attract more electrons than the atom connected to the lower dimer atom. Comparing the third layer atoms, we observe that again the higher atom, lying under the dimer row, has more charge around it than the lower atom, lying between the dimer rows. The general result that is thus obtained from Fig. 3.12 is that if there is a difference in height between atoms lying in the same layer of the Si(100), then the lower atom will have more charge around it.

This difference in charge can be correlated with the difference in bond lengths. From the results of Section 3.3 we can derive a similar result for the average bond length: regardless of the particular type of reconstruction, the higher atoms of a given layer form bonds of larger average length than the lower atoms of the same layer. This correlation can be justified in terms of the electronegativity of the atoms. According to Pauling [96], "electronegativity is the power of an atom when in a molecule to attract electrons to itself". Recently, Allen [1] has provided a useful recipe for calculating electronegativities, by stating that "electronegativity is the average one-electron energy of the valence-shell electrons in ground-state free atoms". An atom forming longer bonds can be thought to raise its electronic energy levels, compared to a bulk atom, due to the spread of the wave function in a larger volume. Combining this with Allen's definition, we conclude that an atom forming longer bonds will be less electronegative, having less charge surrounding it.

This electronegativity argument can be used to explain the longer length of the dimer bond, compared to the distance between neighboring atoms in the bulk Si crystal. It seems that less electrons participate in the surface dimer bond than in a bulk bond; this could account for the observed elongation.

3.6 Surface states I: Simulated STM images

Scanning Tunneling Microscope (STM) has revolutionized the surface physics since his invention in 1982 [6], not only for being the first technique to probe surfaces

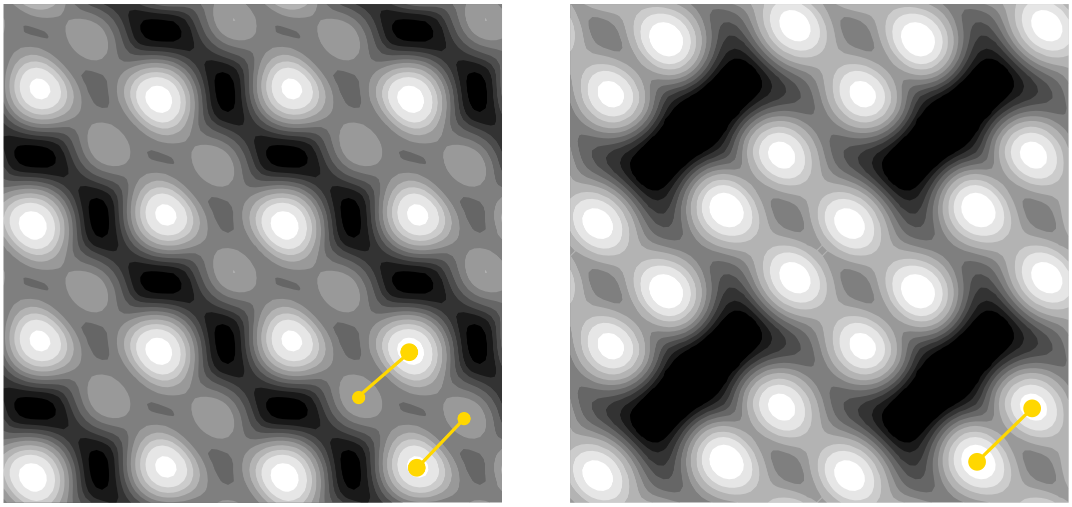

Figure 3.13: Unoccupied states simulated STM images for $c(4\times4)$, perfect (left) and with a missing dimer (right); (bias voltage 2.0 V, constant current mode). The underlying atomic arrangement is shown on top; bigger spheres represent higher dimer atoms.

on the atomic scale in real space, but also because it allows an *in situ* determination of the local density of states [130]. An STM image can thus either reveal an unknown atomic arrangement, or, for a known atomic geometry, give valuable information about the electronic structure.

Si(100) was one of the first surfaces seen with STM [133]. However, in early images most dimers looked symmetric; it was suggested [133] that due to thermal fluctuations, dimers may flipped faster than what STM could capture. Great improvements in the STM techniques of the last few years made it possible to obtain clear pictures of tilted dimers, and establish $c(4 \times 2)$ as the real ground state of Si(100).

In Figs. 3.13 and 3.14 we show representative constant-current simulated STM images for unoccupied and occupied states, respectively. Those were calculated using the theory of Tersoff and Hamann [130]. The bias voltage used is ±2.0 V for scanning the empty and occupied states, respectively. For each (x, y) position, the height of the STM "tip" is adjusted so that the tunneling current is kept constant. We then construct a contour plot of the height as a function of x and y. These plots are smoothened up to eliminate the finite grid effects in the pictures. In each picture the scale is relative, i.e white corresponds to the largest value and black to the smallest.

The $c(4 \times 4)$ reconstruction (left panel of Fig. 3.13) is characterized by alternately tilted dimers, as in the $p(2\times2)$ case. The large bright spots are centered above the higher atom of each dimer. The ellipsoidal grey spot above the lower dimer atom

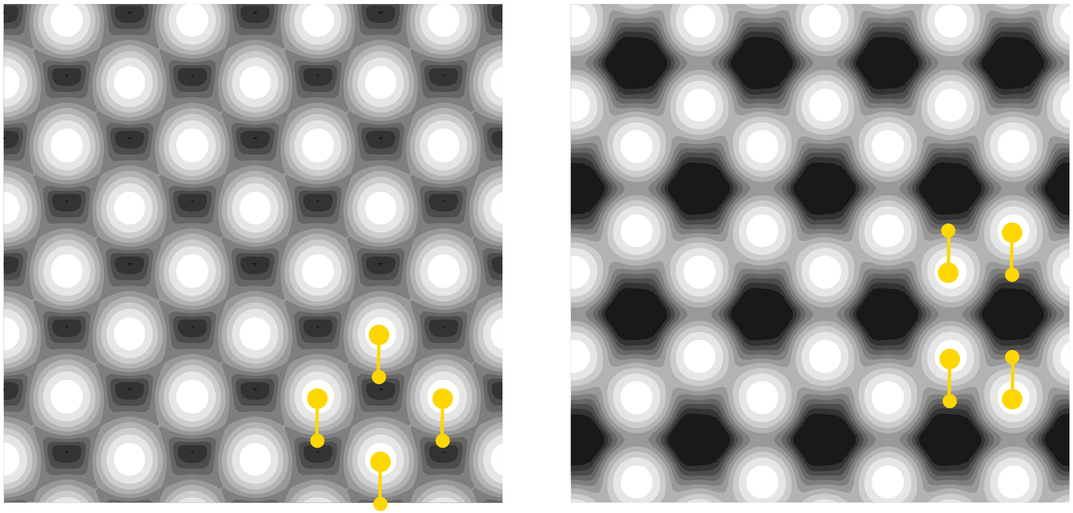

Figure 3.14: Occupied states simulated STM images for $c(2\times 2)$ (left) and $c(4\times 2)$ reconstructions, taken at a bias voltage of -2.0 V. Notation as in Fig. 3.13.

looks like the cross-section of a p orbital perpendicular to the dimer axis. It was mentioned in Section 3.3, that the antibonding dimer state is expected to look like a p orbital centered in the lower atom and pointing outwards, being normal to the dimer line. In fact, this state has also a contribution form the upper dimer atom, and because of the large height difference between the two (0.7 Å), the upper atom appears as a brighter spot in the STM image.

For the missing dimer model, in the right panel of Fig. 3.13, we observe the typical flat dimer pattern, observed in high-temperature STM experiments [133]. The two spots, roughly above the two atoms of the dimer, correspond approximately to two unoccupied sp^3 orbitals.

The occupied-states STM image of the $c(2\times 2)$ reconstruction, is shown in the left panel of Fig. 3.14. This image has a characteristic difference from all others, namely the square lattice periodicity of the bright spots. This feature renders this reconstruction unique and easy to be recognized in experimental STM images. To our knowledge, no such pattern has been reported for Si(100). It is possible, however, that such a pattern would be attributed to the presence of defects, like missing dimer atoms. Probably this structure could account for the C-defect of Si(100).

The ground state of the system, $c(4\times 2)$, gives the STM image shown in the right panel of Fig. 3.14. Each topmost dimer atom is represented by a circular bright spot above it. No other atom of the surface is visible. An STM image for this configuration is compared to experiment in Fig. 3.15. The calculated image looks identical with the experimental one found by Yokoyama *et al.* [146], except for a

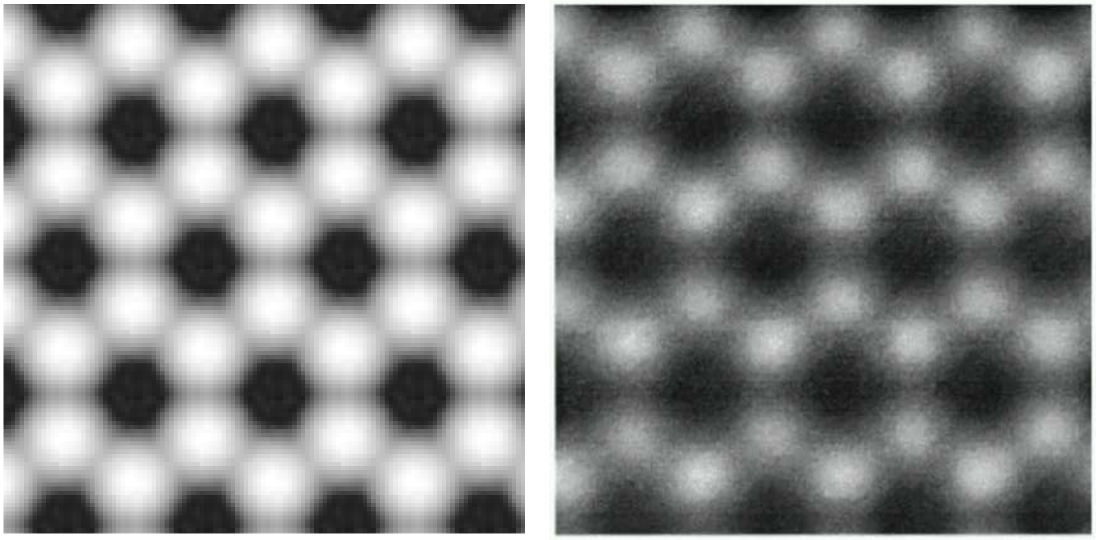

Figure 3.15: Theoretical (left) and experimental (right) STM images for occupied states of Si(100), taken at a bias voltage of -0.8 V. Theoretical image corresponds to the lowest energy configuration found ($c(4 \times 2)$). Experimental image is taken at 63 K with a tunneling current of 100 pA. The image is reproduced from Yokoyama *et al.* [146].

difference in the resolution, which of course can be much higher in a simulation.

This honeycomb-lattice-like pattern was observed in some regions of the first STM image [133] of Si(100) and is routinely reported in recent STM experiments below $\approx$ 200K since the first low-temperature STM experiment by Wolkow [140]. Recent STM experiments however, taking place in liquid He temperatures, doubt that $c(4 \times 2)$ is the ground state of Si(100) in favor of a symmetric dimer reconstruction [146]. Other low temperature STM images do not confirm this prediction [41].

3.6.1 Voltage dependence of the STM images

The STM images for Si(100) depend on the bias voltage, as was mentioned by Hata *et al.* [41]. Left panel of Fig. 3.16 shows a cross-section of the simulated STM image for a bias voltage of -0.8 V, shown in Fig. 3.15, along the dimers. The maxima B correspond to the position of the bright spots in the simulated image, while minima A and C correspond to the regions between the bright spots, short and long, respectively. The lower dimer atom lies between B and C and its existence is not evident in the simulated profile, in aggreement to experiment.

Increasing the absolute value of the bias voltage results in decreasing the height

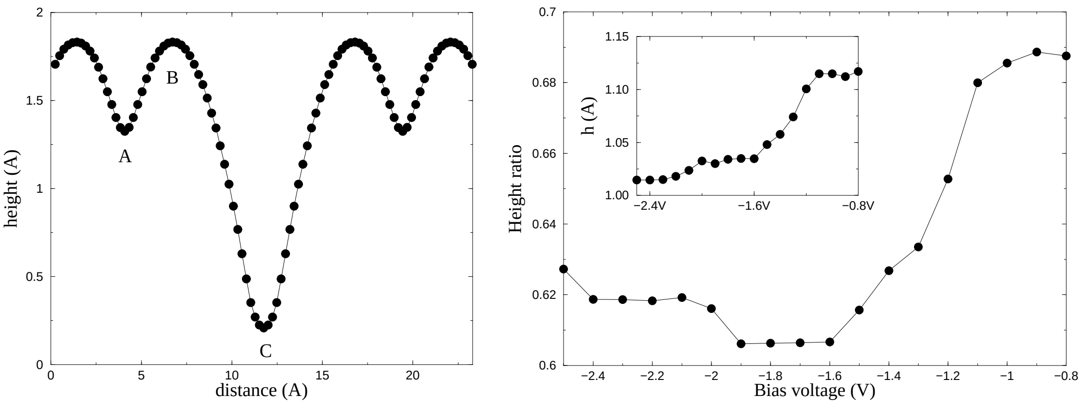

Figure 3.16: Left: Average cross-section of the simulated STM image for Si(100) along the dimers, from the top to the bottom of the theoretical image in Fig. 3.15. Right: Dependence of the ratio (height of A − height of C)/(height of B − height of C) of Fig. 3.16 on the bias voltage. Inset shows dependence of height of B − height of C on the bias voltage

difference between the maximum, B, and the minimum, C, of the STM image as shown in the inset of the right panel in Fig. 3.16. To keep the STM current constant, higher absolute value of the bias voltage results in higher average height difference between surface and STM tip, since the current depends exponentially on this difference. As the STM tip moves higher, details of the surface structure become less recognizable. The plateau of the height difference as for voltages greater than -1.1 V is probably correlated with the width of the surface states; for lower voltages bulk states contribute most to the observed image (see also the band structure in Fig. 3.17).

The increasing tip-smaple distance and the resulting lowering in resolution explains the decreased ratio of height difference between A and C over the height difference between B and A. This ratio decreases as absolute bias voltage increses from 0.8 V to 2.0 V, as shown in the right panel of Fig. 3.16. Up to this point, our results are in very good aggreement with the experimental results of Hata *et al.* [41]. Our theoretical curves have exactly the same shape as the experimental ones, and the plateaus are observed at exactly the same voltage range. There is a difference in the magnitudes of both height and height ratio, as our values are about double the experimental ones. This difference can be attributed to the uncertainty in the calulation of the tunneling current in theory and the neglect of tip-surface interraction in the Tersoff-Hamann theory.

For absolute bias voltage greater than 2 V, we observe a slight increase of the

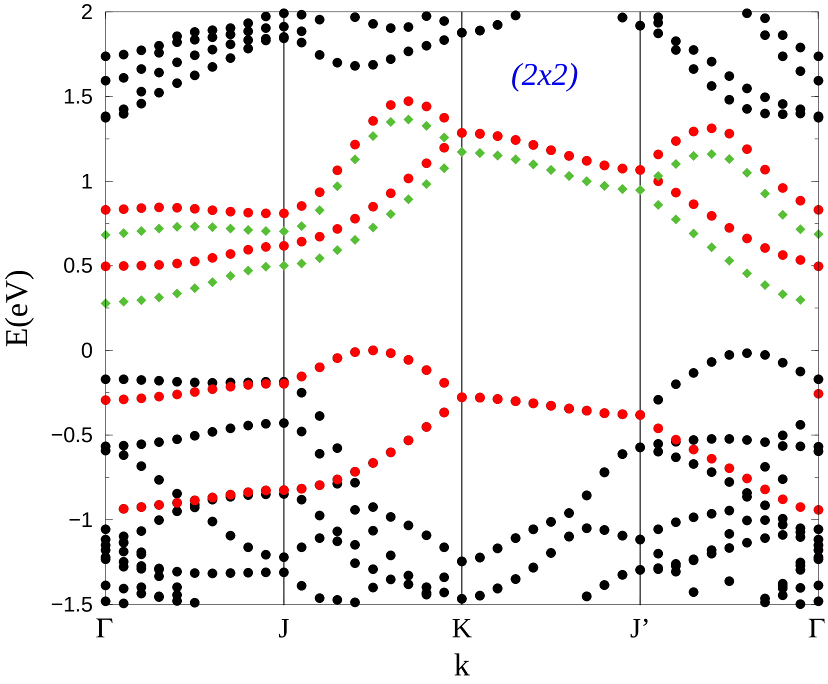

Figure 3.17: Dispersion of quasi-particle eigenvalues for (2 × 1) asymmetric dimer reconstruction. Dangling bond surface states are represented by dark gray circles. Light gray diamonds are DFT excited surface states without the GDFT correction.

ratio between the depths of the two minima. Unfortunately, Hata *et al.* [41] used voltages up to 2 V, so this effect cannot be compared to experiment. The calculated increase can be associated to the peak around 2.1 eV in the density of states for Si(100) [114].

3.7 Surface states II: Band structures

A representative band structure, for the (2 × 1) asymmetric reconstruction, is shown in Fig. 3.17. To find the surface states, we compared the integrals of the wavefunction norms in the vacuum region. The two occupied and unoccupied states extending more to the vacuum region are considered to be surface states. The most important directions in the Brillouin zone, connecting high symmetry points of the bulk structure, were considered. The definition of these points is the following: $\Gamma(0,0,0)$, $J(\frac{1}{2},0,0)$, $J'(0,\frac{1}{2},0)$, and $K(\frac{1}{2},\frac{1}{2},0)$ in units of $\frac{2\pi}{a_s}$, a_s being the surface lattice constant, which is related to the diamond structure lattice constant a by $a_s = a\frac{\sqrt{2}}{2}$.

The two occupied and unoccupied surface bands, shown by dark grey circles in Fig. 3.17, are related to the dimer bond. They are traditionally named π and π^*, the names coming from early tight-binding calculations for Si(100), where these two bands arise from the broadened bonding and antibonding states of the atomic orbitals belonging to the two atoms that form the dimer. In such a picture, the π bond energies lie near the Fermi level, while the σ bond energies are within the projected bulk band structure and appear as resonances (not shown here).

The correction to the DFT excitation spectra proposed by Fritsche in the framework of Generalized Density-Functional Theory [27, 28, 29] (GDFT) was applied to the conduction bands. This theory states that the excitation energy for an electron to move from occupied state i to unoccupied state f is $\epsilon_f - \epsilon_i + \Delta fi$, where ϵ_f, ϵ_i are the Kohn-Sham eigenvalues and Δfi the GDFT correction. In a bulk crystal, the natural choice for the "initial" orbital i is the highest occupied band for each $\mathbf{k}$, since inter-$\mathbf{k}$ transitions or excitation of an electron in a lower occupied state are much less likely to happen.

Extending this interpretation [108] to the surface band-structure, we used occupied surface states in the calculation of the correction integral for unoccupied surface states, and occupied bulk-projected states in the calculation of the bulk-projected unoccupied states. The states as given by Kohn-Sham eigenvalues are shown with light grey diamonds in Fig. 3.17. The correction of the DFT band structure has a weak wave-vector dependence, and can be approximated by a uniform shift of the conduction band. This is observed also in GW corrections of the DFT band structures [113, 112].

For the $p(2 \times 2)$ reconstruction, we find a weaker dispersion of both π and π^* bands in the $p(2 \times 2)$ reconstruction. This is a result of the broken symmetry and the doubling of the periodicity, and accounts also (in the occupied states) for the lowering of the energy. The same effects takes place in the transition from symmetric (2×1) to the asymmetric (2×1). In the symmetric dimer case, the Fermi level (E_F) crosses both π and π^* bands, giving a metallic density of states around E_F. This metallic nature, in contrast with experiment, guided Chadi [15] to propose the tilted dimer model for Si(100). The bands are found to have an even smaller dispersion in the $c(4 \times 2)$ reconstruction [87]. The overlap of neighboring π states, which is responsible for the opening of the bands, should be much more important among a dimer row, where the dimers have a distance of a_s, than between rows, where dimers have a distance of $2a_s$. This overlap is usually assumed to decay exponentially with distance [40].

The different arrangement of tilted dimers seem thus to change the bandwidths, but not the essential characteristics of the band structure. As it was the case in the geometrical features, the band structure changes dramatically from the symmetric to the asymmetric dimer models, but is roughly independent of the specific reconstruction.

This is quantitavely shown in the minimum band gaps. We find the minimum band gap to be 0.50 eV for asymmetric (2×1), 0.56 eV for $p(2 \times 2)$, and 0.62 eV for $c(4 \times 2)$. These values include the GDFT correction; the DFT/LDA values are about 0.1-0.2eV smaller. Our results agree very well with the much more sophisticated and computationally costly GW approximation, which gives 0.65 eV for $p(2 \times 2)$ [113] and 0.70eV for $c(4 \times 2)$. In particular, we agree in the ordering of the band gaps and our values differ by about 10%, which is very satisfactory, considering the simplicity of the GDFT approach.

There are not many experimental values for the surface fundamental band gap, and the existing ones show a broad dispersion. Presenting experiments in chronological order, surface photovoltage [84] gives 0.65 eV; optical absorption spectroscopy [14] gives 0.44 eV; scanning tunneling spectroscopy [39] gives 0.9 eV; finally, angle-resolved ultraviolet photoelectron spectroscopy [50] gives 0.7-0.8 eV, if we assume that E_F lies in the middle of the gap. Recent scanning tunneling spectroscopy results [88, 146] converge that the fundamental band gap is around 0.6 eV, in excellent agreement with our calculation (0.62eV).

The $c(2 \times 2)$ reconstruction was found to be semiconducting, with an energy gap of 0.51 eV, close to the band gaps that appear in the other structures, giving another evidence that the opening of a gap between occupied and unoccupied states is mainly a result of the tilted dimers, rather than of the periodicity. The missing dimer model was also found to be semiconducting, with a smaller band gap of 0.31 eV. This value however probably is only an estimate of the minimum gap, since we scanned only ΓJ and ΓJ′ directions.

3.8 Conclusions

Undergoing hundreds of studies each year, Si(100) has still a lot to reveal. In this study, we focused in its microscopic, atomic-scale structure, and the physics and chemistry of the dimer bond. Calculated bond lengths and angles, total energies, STM images and band gaps are in very good agreement to the observations. We used a real-space method (HARES), which, apart from its excellent parallelizability and precision, offers direct access to the charge density and wave functions.

The lowest energy structure for Si(100) is found to be an antiparallel arrangement of tilted dimers in the $c(4 \times 2)$ periodicity; this reconstruction is by far the lowest energy one. The dimer reconstruction causes a re-hybridization of the surface layer atoms. The highest atoms are unhybridized, while the lower are sp^2 hybridized. The dimer bond length is slightly longer than the bulk bond length, a result observed in several experiments.

The new structure we propose, $c(2\times2)$, is found to have very similar geometrical characteristics with the other reconstructions, and be only a tenth of an eV per 2×1 unit cell higher in energy than the ground state. This configuration could account for observed defects in Si(100) or for structures observed after adsorption. The missing dimer defect was found to have a low formation energy of 0.22 eV. The geometrical and electronical characteristics of a dimer and the atoms below it are insensitive in the periodicity of the system. The prefference of the system for the one or the other periodicity is a result of both electrostatic and elastic strain interactions.

The occupied surface state is similar to a superposition of s orbitals centered at the highest dimer atoms. The upper dimer atom has less total charge around it than the lower dimer atom, which in turn has lower charge than the average bulk atom. Atoms in the third and fourth layer are non-equivalent, with those below the dimer row forming shorter bonds and having more charge concentrated around them compared to atoms of the same layer lying between dimer rows.

In STM images only the topmost atoms of the system are visible. The simulated STM image for the lowest energy structure is almost identical to the observed one. Increasing the bias voltage of the STM results in decreased resolution until 2.0 V. This value is associated with the structure of the density of states.

All considered models were found to be semiconducting, with an energy gap of around 0.6 eVs, smaller than that of bulk Si. The only exception of the symmetric (2×1) reconstruction, which is significantly less favorable energetically than the others. The band structures show distinct surface-states valence bands, while the surface-states conduction bands are crossed by projections of bulk states. The bandwidth of the surface states is larger for $c(4\times2)$ than for $p(2\times2)$. For the asymmetric (2×1) the bandwidth is even smaller.

3.9 Appendix: The dipole approximation

In this Appendix, we attempt to find the electrostatic contribution to the choice of the particular arrangement of tilted dimers in Si(100). To estimate the contribution of electrostatics in the energies of the various reconstructions, we consider a phenomenological model for Si(100) in which each dimer is represented by a point dipole. The dipole points towards the higher dimer atom, where possitive charge is centered (see Sec. 3.5). We consider a 2D lattice, each of its points (i, j) associated with a point dipole moment $\mathbf{p}_{ij}$.

If $\mathbf{p}_{00}$ is the dipole moment at the origin, (0,0), we can write the total electrostatic energy per dipole (or per dimer) of the system as

$$E = \sum_{i,j=-\infty}^{\infty} \left\{ \frac{\mathbf{p}_{00} \cdot \mathbf{p}_{ij}}{|\mathbf{r}_{ij}|^3} - 3\frac{(\mathbf{r}_{ij} \cdot \mathbf{p}_{00})(\mathbf{r}_{ij} \cdot \mathbf{p}_{ij})}{|\mathbf{r}_{ij}|^5} \right\}, \tag{3.1}$$

where $\mathbf{r}_{ij}$ is the position of the (i, j) lattice point. The point $(0, 0)$ is excluded from the sum in Eq. (3.1).

We follow the convention of Fig. 3.9, where x axis is parallel to a dimer row, y axis is perpendicular to the dimer row and parallel to the projection of a dimer in the (100) plane, and z axis is normal to the (100) plane pointing towards the bulk. The lattice vectors are

$$\mathbf{r}_{ij} = a_s(i, lj, 0), \tag{3.2}$$

with l equal to 2 for (2×1), $p(2 \times 2)$ and $c(4 \times 2)$, and 1 for $c(2 \times 2)$. The dipole moments are taken to be of magnitude p and zero projection on the x axis. Dipole moments are taken to lie in the yz plane forming angle θ with the y axis. They are arranged parallel for (2×1) and $c(2 \times 2)$, antiparallel along y for $p(2 \times 2)$ and antiparallel along both x and y for $c(4 \times 2)$, so that

$$\mathbf{p}_{ij} = p(0, x_{ij} \cos\theta, -\sin\theta), \tag{3.3}$$

where x_{ij} is 1 for both (2×1) and $c(2\times2)$, $(-1)^i$ for $p(2\times2)$, and $(-1)^{i+j}$ for $c(4\times2)$. The considered cases can be seen in Fig. 3.8.

Substituting Eqs. (3.2) and (3.3) into Eq. (3.1) we get

$$E = \frac{p^2}{a_s^3}\left\{ \sum_{i,j=-\infty}^{\infty} \frac{1}{(i^2 + l^2j^2)^{\frac{3}{2}}} + \sum_{i,j=-\infty}^{\infty} \frac{i^2 - l^2j^2 + (i^2 - 2l^2j^2)x_{ij}}{(i^2 + l^2j^2)^{\frac{5}{2}}} \cos^2\theta \right\} \tag{3.4}$$

For a given reconstruction, energy is a linear function of $\cos^2\theta$, where θ is the angle between the dipole moment and the (100) plane. Apparently, the total electrostatic energy has to be invariant to the substitutions of θ by $-\theta$ or by $\pi - \theta$,

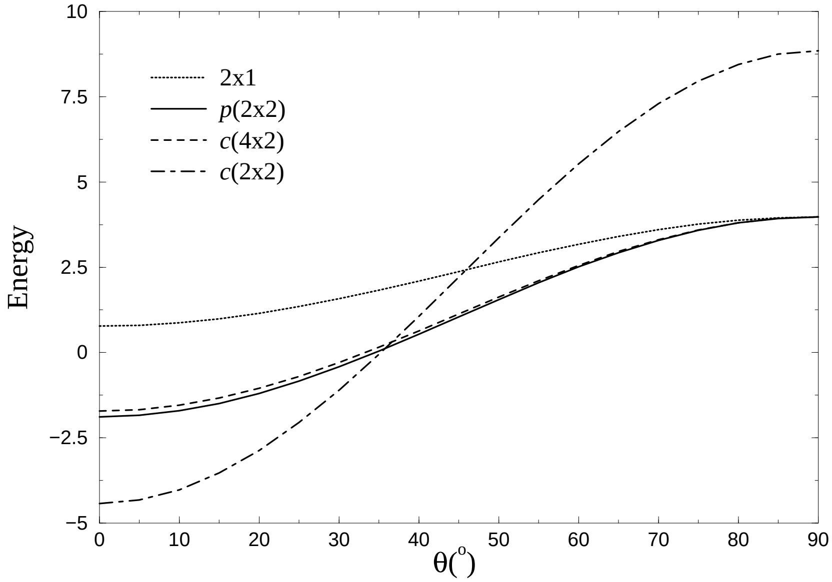

Figure 3.18: Electrostatic energies (in units of p^2/a_s^3) of the various reconstructions of Si(100) as a function of the angle between the dipole moment in the 2×1 cell and the (100) plane.

as they produce a mirror configuration. The angle θ is the only free parameter in this model, as a_s is known and p can only alter the energy scale. In this model we approximate the *whole* (2×1) cell with a point dipole. As was discussed in Sec. 3.5, there are several charge transfer effects around the tilted dimer, and thus θ cannot be assigned to the dimer tilt angle of $\approx 20°$. Indeed, the relative energy differences as obtained by the *ab initio* calclulation are best fitted by taking θ to be about 45°.

We plot the electrostatic energy as a function of θ in Fig. 3.18. For $\theta = 90°$, all three dimer-row reconstructions, (2×1), $p(2 \times 2)$ and $c(4 \times 2)$, have equal energies, as in this case dipoles point towards (100). For the other extreme case, $\theta = 0$, the $c(2 \times 2)$ reconstruction has the lowest energy. This arrangement of dimers is the energetically favorable configuration for up to about 35°. The low electrostatic energy in this reconstruction is most likely the reason for its relatively low energy.

The antiparallel arrangement of dimers in $p(2 \times 2)$ and $c(4 \times 2)$ reconstructions gives an electrostatic energy much lower than 2×1 for the whole range of θ. We can then conclude that the buckling of dimers in Si(100) is a result of dipole-dipole electrostatic interactions. In contrast to the results of the *ab initio* calculation, $p(2 \times 2)$ has slightly lower energy than $c(4 \times 2)$. The fact that $c(4 \times 2)$ is the lowest energy configuration for Si(100) does *not* originate in electrostatics, but is rather a result of chemical interractions between topmost atoms of adjacent dimers or of strain fields associated with each reconstruction.

Chapter 4

C on Si(100) I: Low C content

We study the thermodynamics of C incorporation on Si(100), a system where strain and chemical effects are both important. Our analysis is based on first-principles atomistic calculations to obtain the important lowest energy structures, and a classical effective Hamiltonian which is employed to represent the long-range strain effects and incorporate the thermodynamic aspects. We determine the equilibrium phase diagram in temperature and C chemical potential, which allows us to predict the mesoscopic structure of the system that should be observed under experimentally relevant conditions.

Carbon-enriched silicon systems are the focus of current interest as candidates for a material with tailored electronic properties, which is compatible with well-established silicon technology. The tetravalent nature and large band gap in the diamond structure make carbon an ideal candidate for incorporation in Si. However, the solubility of C in Si under thermodynamic equilibrium is extremely low ($\approx 10^{-5}$) due to the huge mismatch in bond length (35%) and bond energy (60%) between C and Si. Non-equilibrium methods, such as molecular beam epitaxy (MBE), that exploit the higher atomic mobility on surfaces, can be used to overcome this obstacle and enhance solubility [116]. As predicted theoretically by Tersoff [129], C solubility is enhanced by several orders of magnitude near the Si(100) surface, especially in subsurface layers. Osten *et al.* [89] confirmed experimentally this prediction and observed that C atoms diffuse to subsurface layers above a certain temperature. This finding opened new possibilities for growth of C-rich metastable structures.

The enhanced solubility near the surface has important consequences. The large tensile strain associated with C incorporation in Si has proven a very powerful tool in device engineering: a small amount of C can compensate the Ge-induced tension in pseudomorphic SiGe layers [23, 90, 58] , and can also suppress dopant outdiffusion. This idea was recently implemented in a novel heterojunction bipolar transistor [93]. Another interesting effect [11, 81] produced by C incorporation on the Si(100) surface is an unusual change of the surface periodicity after deposition of even a small amount of C ($\approx \frac{1}{8}$of a mono-layer (ML)): the well-known $c(2 \times 4)$ or $p(2 \times 2)$ reconstructions of the pure Si surface change to a $c(4 \times 4)$ pattern. This is clearly visible in several LEED experiments after ethylene exposure [121, 127], or MBE [11].

The microscopic features of C incorporation in Si are rather well understood. Previous work by the authors [61, 60] revealed an oscillatory C profile driven by the competition between two factors: the tendency of C atoms to occupy favorable sites which are determined by the reconstruction strain field, and the preferential arrangement of C atoms at certain distances which minimizes the lattice elastic energy. The profile is characterized by enhancement of C content in the first and third layer, depletion in the second and an exponential reduction from the fourth layer and beyond. The favorable C sites are in the third layer between the surface dimers, being under compressive stress [62, 129] and thus suitable for the smaller-sized C atom. The preferential arrangement of two C atoms in the surface layers is at a third nearest-neighbor position, which is also the lowest-energy configuration in the bulk [116]. The interaction of C atoms in first nearest neighbor position is highly repulsive [61]. It is also unlikely that C-C dimers play an important role in determining the structure of the surface, for several reasons: experiments [11] show that C-C dimers are quite rare in the annealed C-Si(100) surface; when C-C dimers do exist, the intensities of Raman peaks associated with them are an order of magnitude smaller than those associated with isolated C defects [71]; previous *ab initio* calculations by the present authors reveal that a C-C dimer is energetically preferred only in very special situations (like at 1ML C coverage with imposed (2x1) periodicity [61], or in the presence of strain-relieving missing dimers [72]) and even then, the energy of the dimer containing structures is higher than the structures considered in the present study, typically by 1 eV/dimer.

Although the microscopic aspects of C incorporation have been extensively studied and are well understood, a mesoscopic picture of the surface structure that would link the atomistic features to long-range strain effects, and predict structures for different growth conditions more relevant to experiment, is lacking. Here, we present an approach that closes this gap and is able to determine the equilibrium surface phase diagram. It is based on first-principles atomistic studies, incorporating microscopic strain and polarity effects, which are expected to have a dominant role in the understanding of C incorporation in the host Si lattice. The results are linked to a classical effective Hamiltonian in a Monte Carlo scheme that incorporates strain into the thermodynamic aspects of the problem.

4.1 Microscopic Configurations

We considered first all possible atomistic configurations likely to have low energies. Guided by previous work, [129, 61, 60, 72] we can establish a set of rules which should be obeyed by low energy configurations of the C-Si(100) system, namely:

(i) The surface has $c(4 \times 4)$ periodicity.

(ii) C substitutes Si atoms only in the first (surface) or in the third layer.

(iii) There are no C-C nearest neighbors, or second nearest neighbors.

(iv) Third layer C exists only at sites between pairs of surface dimers.

We constructed every possible structure of the C-Si(100) system, consistent with these rules, with 0, 1, 2, 3 and 4 C atoms per $c(4 \times 4)$ unit cell, for neutral systems[1]. The various sites in the $c(4 \times 4)$ unit cell occupied by C in the various configurations are shown in Fig. 4.2. The configurations are named NX, N being the number of C atoms in the $c(4 \times 4)$ unit cell and X an index to distinguish structures of the same N. All possible configurations for C incorporation on Si(100), which are consistent with the rules (i)-(iv), are shown in Fig. 4.1.

---

[1] Charged states are often important for *isolated* point defects. We do not expect such states to be energetically favorable for periodically repeated configurations such as the ones considered here, where the high concentration would raise the Coulomb energy significantly.

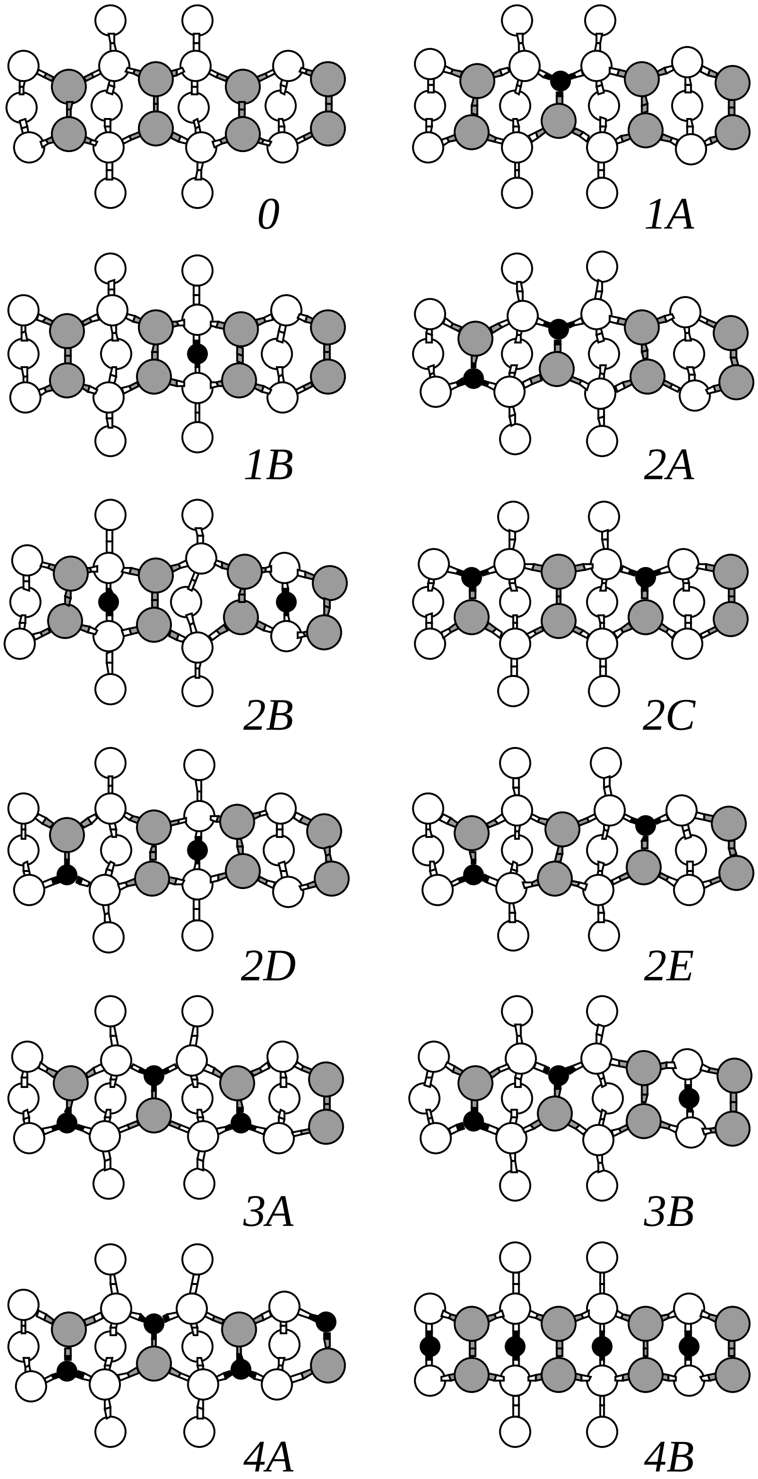

Figure 4.1: Top views of the relaxed geometries for all possible configurations of C-Si(100), consistent with rules (i)-(iv) of the text. Si surface atoms are shown as gray spheres, Si atoms in 2nd and 3rd layers as smaller, white spheres, and C atoms as black spheres.

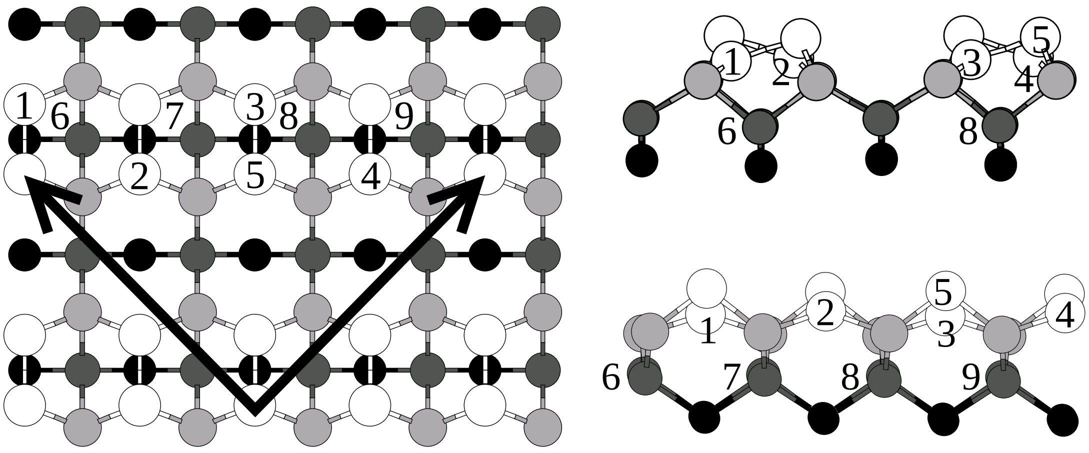

Figure 4.2: Top view (left) and side views (right) of the Si (100) surface. The arrows mark the lattice vectors of the $c(4 \times 4)$ unit cell. The topmost four atomic layers are shown with size (larger) and shading (lighter) indicating proximity to the surface.

4.2 Energetics

To study the energetics and the geometrical features of these configurations, we perform *ab initio* calculations. We use Density-Functional Theory (DFT) in the Local Density Approximation (LDA) [44, 66]. The Kohn-Sham valence electron wavefunctions are expanded to a plane wave basis with a cutoff kinetic energy of 36 Ry. The ionic cores and their interaction with valence electrons were taken into account through the Bachelet-Hamann-Schlüter pseudopotentials [3], in the separable Kleinman-Bylander form [65]. For the exchange-correlation functional we use the results of Ceperley and Alder as they have been parametrized by Perdew and Zunger [13]. The electronic degrees of freedom are relaxed using the Car-Parrinello [12] minimization algorithm.

The system was modeled by a periodic slab geometry consisting of 7 layers of Si plus a terminating layer of H in one side. The bottom Si layer is kept frozen to the bulk positions. Subsequent slabs are separated by roughly 8 Å of vacuum. The Brillouin Zone was sampled by the Γ point only. Atomic positions are relaxed with a conjugate-gradient minimization technique until the magnitude of the calculated Hellman-Feynman forces is smaller than 0.001 Ry/a.u.

The initial geometry for each configuration was the ideal, dimer reconstructed Si(100) with antiparallel arrangement of tilted dimers (configuration 0), with the appropriate Si atoms substituted by C. Other starting geometries were also considered, to ensure that the correct minimum energy structure is found for a given configuration.

Table 4.1: Relative energies for the various configurations considered according to Eq. (4.1) in eV per $c(4 \times 4)$ unit cell. μ_C is taken as the energy of a C atom in diamond. The numbers in square brackets after each configuration name indicate the position of C atoms, according to the numbering scheme of Fig. 4.2.

NX	$E(NX)$	NX	$E(NX)$	NX	$E(NX)$
0	0.00	$2B$ [6,7]	0.81	$3A$ [1,2,3]	1.25
$1A$ [1]	0.19	$2C$ [1,3]	1.06	$3B$ [1,2,9]	1.28
$1B$ [6]	0.08	$2D$ [1,8]	0.49	$4A$ [1,2,3,4]	2.31
$2A$ [1,2]	0.35	$2E$ [1,5]	0.35	$4B$ [6,7,8,9]	10.39

In Table 4.1, we give the energy $E(NX)$ for each configuration NX, relative to the pure Si(100) surface (configuration 0). These energies are defined by:

$$E(NX) = E_{tot}(NX) - N(\mu_C - \mu_{Si}) - E_{tot}(0), \tag{4.1}$$

where $E_{tot}(NX)$ is the calculated total energy of configuration NX, and μ_C, μ_{Si} are the chemical potentials for C and Si atoms, respectively. For Si, the chemical potential is taken to be the energy of the bulk, since this is the natural reservoir for Si atoms due to the presence of steps, terraces, and other surface defects. As a starting point, μ_C is taken to be the energy of a C atom in bulk diamond[2]. We discuss its variation below.

For low concentration of C, one atom per unit cell, which corresponds to $\frac{1}{8}$ ML coverage, the structure with subsurface C ($1B$) has lower energy than the one with a Si-C dimer ($1A$) on the surface. This result is in agreement with experiment: X-ray spectra [121] indicate that for low C deposition, there is almost no C on the surface. A single C atom at a third-layer site relieves the compression due to the surface reconstruction and makes four Si-C bonds while a single C atom on the surface, as part of a dimer, allows the formation of only three SiC bonds. Passing to configurations with more than one subsurface C atom per unit cell, we find that the energy of configuration $2B$ is considerably higher than that of $2A$, $2C$, and $2E$. Apparently, the presence of two subsurface C atoms per unit cell produces a large distortion of the surrounding Si-Si bonds. Thus, for two C atoms in the unit cell ($\frac{1}{4}$ ML coverage), the best situation is to have both C atoms on the surface. For three C atoms per unit cell ($\frac{3}{8}$ ML coverage), we observe an equivalence of surface/subsurface

---

[2] To obtain the chemical potentials, we calculate the energies of C and Si in the diamond structure with the same kinetic energy cutoff and the corresponding k-point grid for the bulk, and use the experimental cohesive energy of diamond, 7.37 eV/atom.

sites: configurations $3A$ and $3B$ have almost the same energy. For the case of four C atoms ($\frac{1}{2}$ ML coverage), there is just one structure ($4A$) consistent with the rules we discussed before. For illustration purposes, we include another configuration, $4B$, containing C atoms in second neighbor positions, which violates rule (iii); its very high energy can be considered as a justification for these rules. We do not go beyond $\frac{1}{2}$ ML coverage because experiments show that this results in disordered structures.

To compare configurations with different C content, we use Eq. (4.1)[3]. This implies that the surface is in equilibrium with a reservoir of C atoms characterized by μ_C. It is generally accepted that C forms small clusters, whose cohesive energies are in the range between -5.5 and -7 eV [52]. In Fig. 4.3(a), we plot the energies of configurations 0, $1B$, $2A$, $3A$ and $4A$ as a function of μ_C. The vertical faint lines denote the transition points at which the preferred structure changes. We observe that the lowest energy structure depends strongly on μ_C and hence on the conditions of C deposition, making it difficult to predict what the actual structure of the system will be. This implies that the equilibrium surface structure might be composed of different configurations at the atomistic level and, consequently, a larger-scale mesoscopic picture is needed. In this picture, the elastic interactions in the boundaries between regions of different C content or atomistic structure will play an important role.

4.3 The Effective Hamiltonian model

To obtain such a mesoscopic description and study the thermodynamics of C incorporation on Si(100), we use an effective Hamiltonian within a Monte Carlo scheme. We first construct a classical, 12-state generalized Potts model. We assume that the surface consists of $c(4 \times 4)$ cells, each of which can exist in any of the lowest energy configurations discussed before. The Hamiltonian is

$$\mathcal{H}_{eff} = \sum_{i=1}^{n} \left[E(c_i) + \frac{1}{2} \sum_{j} \Delta E(c_i, c_j) \right], \tag{4.2}$$

where the summation on i runs over all n cells, and the summation on j over the 8 nearest neighbors of i (the factor of one half takes into account double-counting of the interaction); c_i is the configuration in cell i, and $\Delta E(c_i, c_j)$ is the interaction energy between the neighboring cells c_i and c_j [$\Delta E(c_i, c_i) \equiv 0$]. In order to obtain these interaction energies, we calculated the total energies of all 144 $c(12 \times 12)$ cells consisting of a cell c_i surrounded by 8 c_j cells. These were obtained using Tersoff's

---

[3] Detailed discussion of the use of chemical potentials for energetical comparisons in the grand canonical ensemble can be found in the next Chapter.

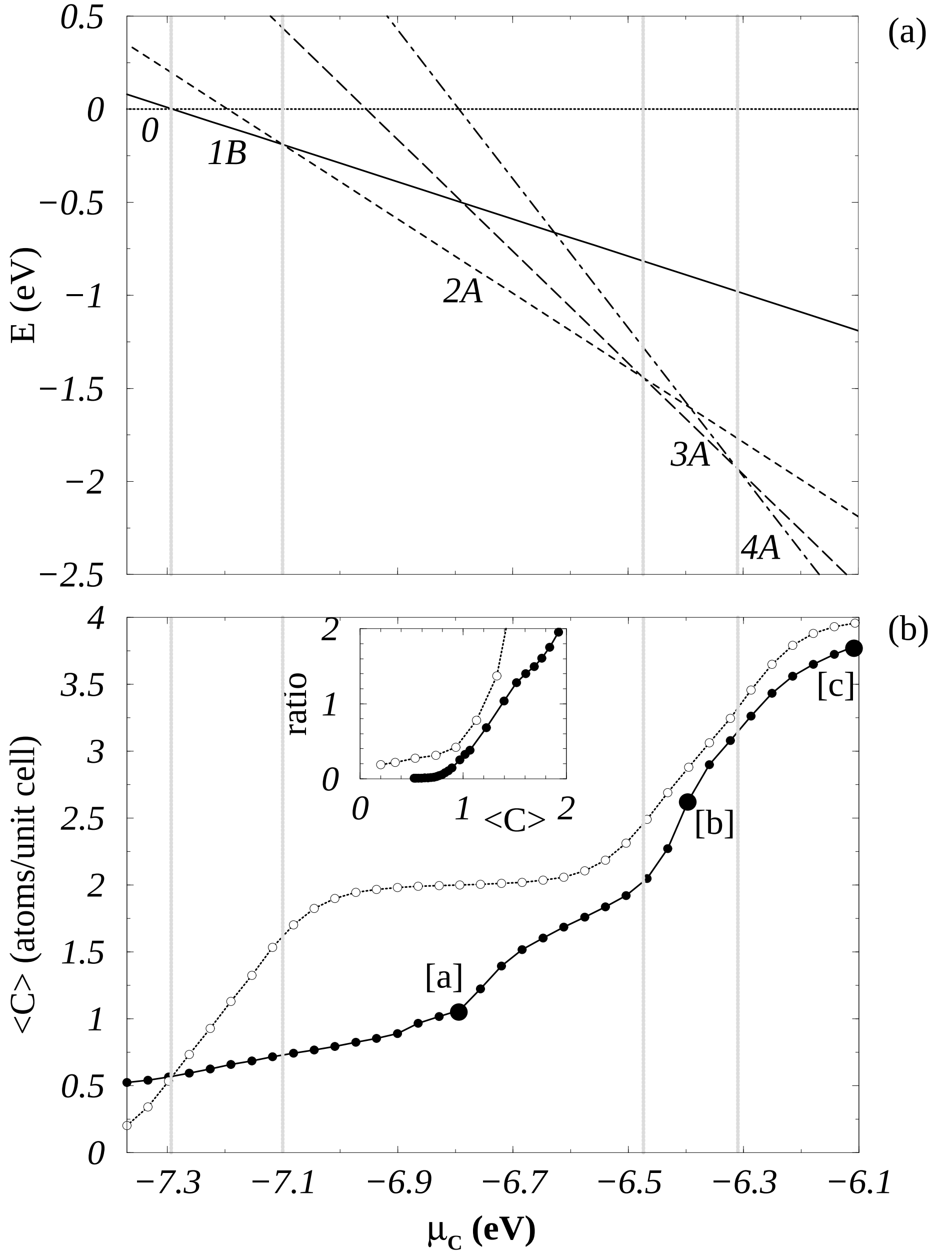

Figure 4.3: (a) The energy of the preferred structure for 1,2,3 and 4 C atoms per unit cell as a function of μ_C, from Eq. (4.1). (b) The average C content of the system as a function of μ_C, at 850K, with (filled symbols) and without (open symbols) elastic strain interactions. The points marked [a], [b] and [c] correspond to the cases shown in Fig. 3. The inset shows the ratio of surface to subsurface C atoms at the same temperature, as a function of the total C content in the unit cell.

empirical potential [128], with a Monte Carlo relaxation method. The key point here is that we are interested in elastic strain interactions between different cells rather than any specific features of their structure; for this type of interaction *between cells* the classical potential employed gives very reasonable results as established by previous studies of similar systems [58, 60].

4.4 Carbon Distribution

Having determined $\mathcal{H}_{eff}$, we performed an equilibrium Monte Carlo study for different values of the temperature and μ_C. We used a 70×70 grid of cells, which was sufficient to get converged averages. For each value of μ_C the system was started from a random configuration at high temperature (1200K) and then was cooled down to room temperature.

In Fig. 4.3(b) we plot the average total C content of the system as a function of μ_C. The zero for μ_C is taken to be the energy of an isolated C atom. For comparison, we plot the same quantity when the elastic strain interactions, $\Delta E(c_i, c_j)$, are set equal to zero. In both cases the average C content of the system increases with increasing μ_C. The difference between the two curves shows the importance of elastic interactions, which, being of the order of 0.1-0.2 eV/ $c(4\times4)$ cell, are more important than the total energy differences in the low μ_C region. This effect weakens as μ_C increases.

An important consideration, with experimentally observable consequences, is the relative amount of surface versus subsurface C atoms as a function of the total C content C_{tot} in the unit cell, shown in the inset of Fig. 4.3(b). For larger total C coverage the ratio increases monotonically, approaching infinity as $C_{tot} \rightarrow 4$. Again, we give the case with $\Delta E(c_i, c_j) = 0$ for comparison. There is a critical coverage of 1.39 C atoms per unit cell, or 0.17 ML, beyond which C prefers mostly surface sites. This critical coverage has a weak temperature dependence: it has a maximum around 850K, and then falls monotonically down to roughly 0.16 ML at 300K and 1100K. The increase of the surface C with increasing total C is not unexpected: although third layer compressed sites seem ideal for the smaller C atom, a large amount of subsurface C would cause large strain and raise the total energy dramatically, as exemplified by the case of configuration $4B$, which we discussed earlier. From Fig. 2(b) we see that the transition from mostly subsurface to mostly surface C content does not coincide with the change from 1 to 2 C atoms per cell, as suggested by our *ab initio* results, indicating that *the elastic strain interactions play a dominant role in the structure of the surface.*

Representative snapshots of the C distribution from the Monte Carlo run at

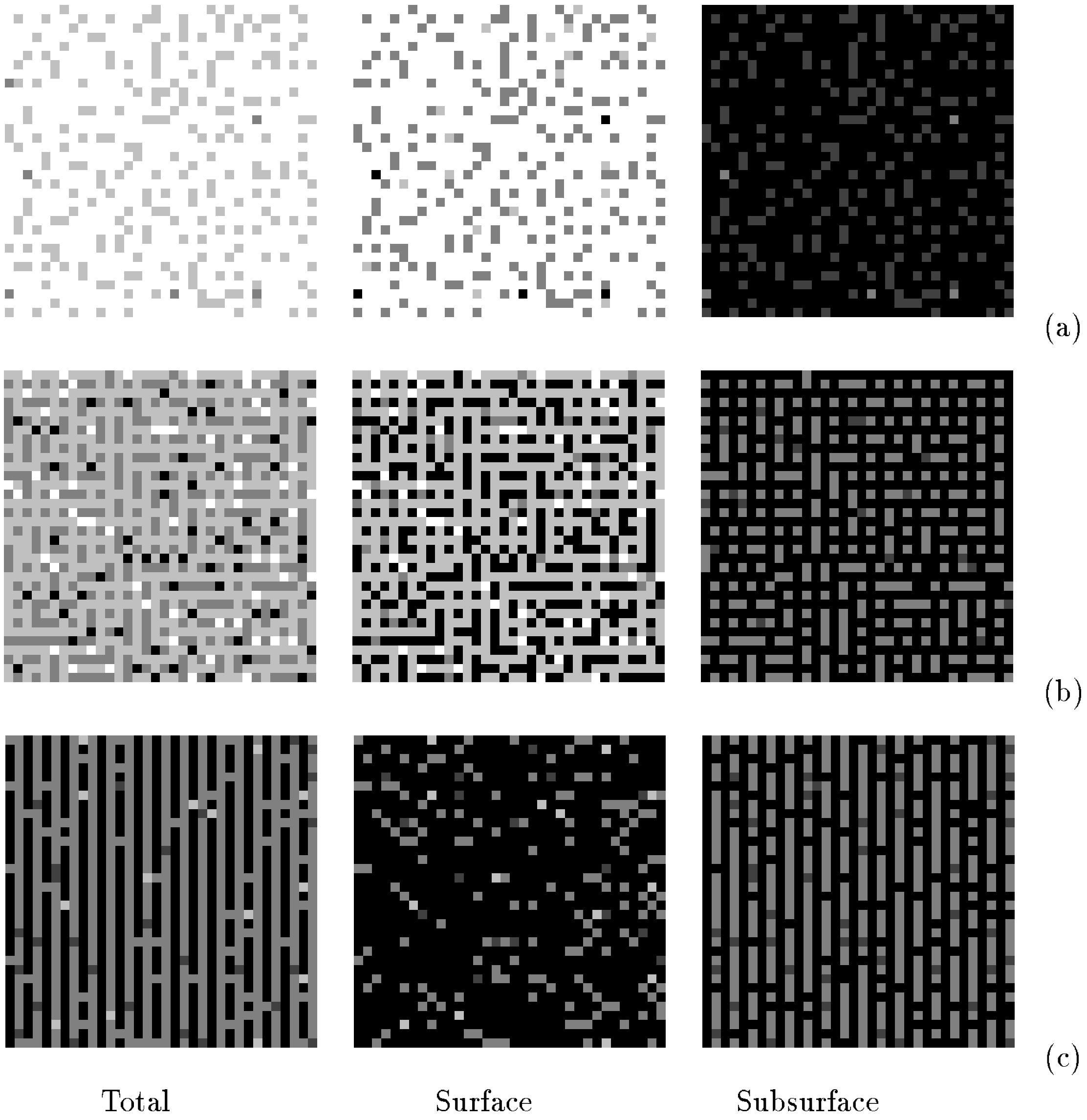

Figure 4.4: Density plot of the C distribution on the surface at T=850K; (a) $\mu_C = -6.1$ eV, (b) $\mu_C = -6.4$ eV, (c) $\mu_C = -6.8$ eV. White corresponds to 4 C atoms, black to 0 C atoms. Each panel represents an area of 38×38 nm^2 and is $\frac{1}{4}$ of our simulation cell.

850K are shown in Fig. 4.4. The three cases correspond to the points marked [a], [b] and [c] in Fig. 4.3(b). An impressive long range order is revealed for the subsurface C (right column of Fig. 4.4). For low μ_C, Fig. 4.4(c), this order appears in the form of alternating rows of similar C content. These consist mostly of unit cells corresponding to 0 and $2B$ structures. Although structure $2B$ has relatively high energy, as shown in Table I, a structure of alternating 0 and $2B$ cells seems to be preferable, giving C the chance to take advantage of the desirable third layer compressed sites. The line-pattern is a result of the strong interactions in that range of μ_C, which forces the $c(4 \times 4)$ cells to have the maximum number of different neighbors, 6 for the row pattern and 4 for a chess pattern. The latter pattern is observed for higher μ_C, Fig. 4.4(b), and is typical for the range of μ_C and temperature corresponding to 1-2 C atoms per unit cell on average (see also Fig 2(b)). In this case, the self-energies of the different configurations dominate over the elastic strain interactions. In the specific example shown in Fig. 4.4(b), the structure consists mostly of $3A$ and $2B$ cells, at a ratio 2:1. This suggests that for conditions corresponding to this range of μ_C, an alternating pattern of surface/subsurface C is preferable. As μ_C increases the energies of the cells become large enough so that the elastic interactions are not that important, and thus the system does not have much to gain by self-organizing. This results in the random pattern shown in Fig. 4.4(a), which consists mainly of $4A$ cells with a few $3B$ cells around them. Again, of the two configurations with three C atoms ($3A$ or $3B$), the one with some subsurface C ($3A$) is preferred when the dominant configuration for these conditions ($4A$) has all its C atoms on the surface.

Finally, we note that while subsurface C shows this interesting ordering behavior, the surface C seems to be randomly distributed as the patterns of the middle column of Fig. 4.4 indicate. The ordered structure appearing in the total distribution of C (left column of Fig. 4.4) is caused by an ordered third-layer C configuration; this is best seen in Fig. 4.4(c). This idea was implicitly suggested by previous experimental work [121, 11]. From our first-principles calculations, we found that the geometrical features of the Si-Si dimers in all 12 cells are essentially the same. Surface C is invisible, or shows up as a missing Si atom, in STM experiments [72]. This implies that one cannot distinguish with standard microscopy pure Si(100) (or Si(100) with vacancies) from a configuration with C in the third layer; the only criterion is the long-range order and the change of the reconstruction.

Chapter 5

C on Si(100) II: High C content

In this chapter we extend the theory of previous chapter to explore configurations of C incorporated on Si(100) at a relatively high C content ($\geq$ 0.5 ML). Such configurations appear near defects, like step edges and missing dimers, and are sometimes responsible for their formation. Our guides for finding the relevant configurations are the experimental STM images. We propose a new configuration of C on Si(100), involving C atoms at second nearest neighbors positions, forming a $\beta-$SiC cluster. This structure is thermally stable and the simulated STM image matches very well the experimental observation. The relative energies and geometrical features of several structures are compared.

C incorporation on Si(100) happens at many cases at conditions far from thermodynamic equilibrium, the most characteristic example being conditions during Molecular Beam Epitaxy (MBE). Although the process is slow enough to ensure that C is substitutional in the Si(100) lattice, there are no warranties for a homogeneous distribution of C. Scanning Tunneling Microscope (STM) images for C-alloyed Si(100) show [72, 73] in these cases some regions with very small C content and some regions where most C is accumulated, forming the characteristic $c(4 \times 4)$ reconstruction. In all cases, a careful optimization of the growth parameters is required to avoid the formation of defects like interstitials or various carbon-related complexes [21, 92].

Knowledge of the carbon-induced atomic rearrangements is necessary to achieve controllable incorporation. Novel phenomena such as spontaneous carbon ordering have been observed by several groups [19, 91, 35]; the most surprising among them is the change of the reconstruction to $c(4 \times 4)$ after C deposition [127, 81, 121, 11, 72].

The microscopic features of C incorporation are rather well understood, and can be summarized in the rules (i)-(iv) of the previous chapter, when C coverage is well below 0.5 Mono Layers (ML). For higher C contents, the structures are expected to involve defects such as missing dimers. In a previous paper [72], a structure with six C atoms per $c(4 \times 4)$ cell, forming a C-C dimer, was found to match the experimental STM image. This structure has an energy more than 2 eV/(unit cell) higher than any of the structures discussed in the previous chapter; its appearance can be attributed to surface kinetics, presence of strain fields due to defects, and C-rich growth conditions.

Here, we present three new structures for C incorporation on Si(100) at high C coverage, and compare their energies and simulated STM images to those obtained by the structure of Leifeld *et al.* [72]. We use *ab initio* Density Functional Theory calculations to obtain the relative energies and simulated STM images of the structures and Monte Carlo simulations to study their stability and thermodynamical properties.

5.1 The configurations

All configurations studied in this work have the $c(4 \times 4)$ periodicity. The configurations are named NX, N being the number of C atoms in the $c(4\times4)$ unit cell and X an index to distinguish structures of the same N. In particular, configurations indexed as A ($5A$ and $6A$) are obtained by substituting the appropriate Si atoms by C in pure Si(100) (configuration $0A$). Configurations indexed as B ($5B$ and $6B$) are obtained by substituting the appropriate Si atoms by C in Si(100) with a

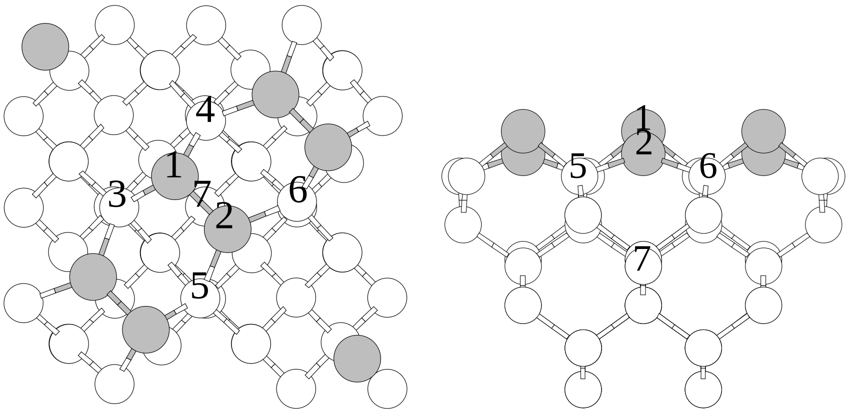

Figure 5.1: Top (left) and side (center, right) views of a $c(4\times 4)$ unit cell of the dimer-reconstructed Si(100). Dimer atoms are shown in gray. The numbers denote sites where C substitutes Si atoms in the configurations discussed in the text.

missing dimer defect (configuration $0A$). The relaxed geometries of the considered configurations are shown in Fig. 5.2.

Configuration $0A$ is the pure, dimer reconstructed Si(100) in the $c(4\times 4)$ periodicity. The dimers are shown in Fig. 5.1 as pairs of large gray spheres. The two atoms forming the dimer do not lie in the same height, i.e the dimer is tilted. Adjacent dimers are tilted in opposite directions, forming a local $p(2\times 2)$ arrangement, which is the lowest energy [1] configuration of the Si(100) surface [107]. $0B$ corresponds to pure Si(100) with an isolated missing dimer defect. The distance between subsequent missing dimers is 15.4 Å, large enough to ensure negligible coupling between defects.

The configurations with 6 C atoms per $c(4\times 4)$ cell ($6A$ and $6B$) contain C atoms at first nearest neighbor positions and a C-C dimer on the surface. The atoms are in positions 1,2,3,4,5 and 6 of Fig. 5.1. The configuration including a missing dimer, $6B$, was proposed by Leifeld *et al.* [72] as a good candidate to account for the observed STM images. C atoms are not expected to be in nearest-neighbor positions in bulk $Si_{1-x}C_x$ alloys [116, 61], and C-C dimers are quite rare in annealed C-Si(100) samples [11]. C-C dimers do exist however, and they seem to be favored by C-rich growth conditions [61] or in the presence of strain-relieving missing dimers. We study here this configuration together with a similar one but with no dimer missing ($6A$).

We propose two new structures for C-alloyed Si(100), with 5 C atoms per unit cell. They are configurations $5A$ and $5B$, with C atoms in positions 3,4,5,6 and 7 of Fig. 5.1. These structures contain C atoms in second-nearest neighbor

---

[1] The $c(4\times 2)$ reconstruction of Si(100) has a slightly lower energy than $p(2\times 2)$; the difference is a few meV's per dimer.

positions, which form a β-SiC cluster below the surface. Formation of SiC clusters during C incorporation on Si(100) has been previously reported [89]. In addition, the structures have a C atom at the fourth layer directly below the surface dimer. This site is under compressive stress due to the reconstruction of Si(100) [62, 129] and is expected to be extremely favorable for C.

5.2 The method

The need for combining different theoretical methods in this study arises from the nature of the properties of interest. In the microscopic level, the large differences in covalent radii (35%), bond enthalpies (35%) and electronegativities (25%) between C and Si, suggest that the strongly distorted bonds and the charge transfer effects excepted in the system establish the necessity for quantum mechanical calculation of the total energies and forces.

From the other hand, the calculation of free energy in a quantum mechanical scheme for large-size systems as the ones under study here is either unfeasible or approximate. For this purpose we employ Monte-Carlo calculations using empirical potentials. This approach allows us not only to calculate the free energy of the system at any temperature, essentially at the accuracy of the empirical potential we chose, but also to explore diffusion of atoms, transformations of the system and possibly phase transitions.

5.2.1 *Ab initio* method

We model the system by a repeated slab geometry, having 7 layers of Si atoms and a terminating H layer at the bottom. The Si layer above the H atoms is kept fixed during the simulation, with the positions of H chosen in order to mimic the bulk Si-Si bonds. The other 6 Si layers are allowed to move. The system has the $c(4 \times 4)$ periodicity with the lattice constant taken to be that of bulk Si. The repeated slabs are separated by $\approx$10Å of vacuum. This choice of supercell has been proven excellent for the description of both pure [107] and C-enriched [109] Si(100).

The *ab initio* calculations were performed using the commercial Vienna *Ab initio* Simulation Package (VASP) [69, 67, 68], based on Density Functional Theory (DFT) [44, 66]. The exchange and correlation energy and potential was calculated using the Generalized Gradient Approximation (GGA) functional of Perdew and Wang [101]. The atomic cores and their interactions with valence electrons were taken into account via the ultra soft Vanderbilt type pseudopotentials [135] as supplied by G. Kresse and J. Hafner [70].

The Brillouin zone of the system was sampled by the Γ point, which is sufficient due to the large size of the unit cell. The wave function was expanded to plane-waves using a cut-off energy of 26 Ry. For fixed ionic positions, the wave functions are calculated using a preconditioned conjugate gradient minimization algorithm, until the total energy is converged up to 10^{-4} eV. In each self-consistency step, the output charge density is mixed with the input one using a Pulay mixing method [102]. The ionic positions are relaxed using a conjugate gradient minimization algorithm, until the difference in the converged total energies before and after each ionic step is smaller than 10^{-3} eV.

The STM images were obtained from the calculated wave functions by means of the Tersoff and Hamann theory [130]. In this scheme the tunneling current is proportional to the local density of states at the microscope tip, integrated in a window of energies from -V to E_F, where V is the voltage between tip and surface, and E_F is the Fermi level of the system. We can thus calculate the tunneling current I as a function of the surface coordinates (x, y) and the tip-surface distance z. To simulate the constant-current mode of the STM, we solve numerically the equation $I(x, y, z) = I_0$ with respect to z, and then draw a contour plot of z as a function of x and y.

It is well known that although the dimers of Si(100) are tilted, with one atom located higher than the other, they appear symmetric at STM images taken at room temperature. The reason is [133] that due to thermal vibration of atoms, dimers flip at a frequency much higher than what STM tip can capture. The room temperature STM image is thus an average over the two possible configurations of each dimer. To make our simulations directly comparable to the observation, we also symmetrize the derived STM images: for each (x, y) point of the surface, we plot the average of the tip height at this point and at the symmetric point with respect to the dimer row.

5.2.2 Monte Carlo method

We perform continuous-space Monte Carlo calculations. The energy of the system is obtained using the multi-component empirical potential of Tersoff [128]. We use the *semi-grand* canonical ensemble, where the total number of atoms is kept fixed, but atoms are allowed to change identity from one species to the other via Ising-type flips [62, 58, 59]. In this work we use a special case of the semi-grand canonical ensemble, where in addition to the total number of atoms, the numbers of Si and C atoms are kept fixed. This method is very efficient in calculating equilibrium composition profiles for complicated systems [60].

At each Monte Carlo step, an atom is displaced randomly from its position, and/or exchanges identity with another atom of the system. The move is accepted or rejected with probability

$$P = e^{-\Delta U/k_B T}, \tag{5.1}$$

according to the Metropolis algorithm [79]. ΔU is the difference between the energies of the system after and before the Monte Carlo step.

To overcome the large diffusion barriers associated with C incorporation, Kelires [58] has introduced a relaxation of the nearest neighbors of the atoms that exchange identities before the energy change ΔU is calculated.

For the MC simulations we model the system by a supercell consisting of four $c(4\times4)$ cells with 7 layers of Si atoms. The bottom layer is fixed to the bulk positions. The lattice vectors parallel to (100) are kept fixed to their values for bulk Si, and the lattice vector perpendicular to (100) is relaxed, allowing the layer separation distance to change in order to minimize the total energy.

5.2.3 Comparison of energies

To compare the energies of the structures, we need to take into account the fact that they contain different number of atoms, that is we need to use the grand canonical ensemble formalism. For this purpose we calculate the grand thermodynamical potential,

$$\Omega(NX) = F_{tot}(NX) - N\mu_C - N_{Si}\mu_{Si}, \tag{5.2}$$

where $F_{tot}(NX)$ is the calculated total free energy of configuration NX, N and N_{Si} is the number of C and Si atoms in configuration NX. μ_C and μ_{Si} are the appropriate chemical potentials for C and Si, respectively. The chemical potentials tune the stoichiometry of the system and are extremely important in the prediction of the favorable structure [55, 56].

We define the relative energies of the cells with respect to $0A$, the pure Si(100),

$$E_r(NX) = \Omega(NX) - \Omega(0A) \tag{5.3}$$

and the formation energy, which is the energy difference between NX and $0X$:

$$E_f(NX) = \Omega(NX) - \Omega(0X). \tag{5.4}$$

The relative energy, $E_r(NX)$, is the amount of energy needed to remove N Si atoms from pure Si(100) (configuration $0A$), put them in bulk Si, and substitute them with C atoms taken from the appropriate reservoir. For the structures labeled B, which contain a missing dimer, $E_r(NX)$ includes the energy cost to remove the

Table 5.1: Relative and formation energies for the various configurations considered according to Eqs. (5.3) and (5.4) in eV per $c(4 \times 4)$ cell. $E_r^{(2)}$ is the free energy difference at 800 K, calculated with the Monte Carlo method. μ_C is taken as the energy of a C atom in diamond. The numbers in the second line after each configuration name indicate the position of C atoms, according to the numbering scheme of Fig. 5.1.

Conf.	$0A$	$0B$	$6A$	$6B$	$5A$	$5B$
C atoms	-	-	[1,2,3,4,5,6]		[3,4,5,6,7]	
$E_r(NX)$	0.00	0.25	7.94	6.99	3.16	3.75
$E_f(NX)$	0.00	0.00	7.94	6.74	3.16	3.51
$E_r^{(2)}(NX)$	0.00	1.39	10.1	8.84	4.02	4.12
$E_f^{(2)}(NX)$	0.00	0.00	10.1	7.45	4.02	2.73

dimer. In contrast, the formation energy, $E_f(NX)$, is the amount of energy required to remove N Si atoms from either pure Si(100) or Si(100) with a missing dimer (configuration $0X$), put them in bulk Si and substitute them with C atoms. In other words, those two energies correspond to the enthalpies of the reactions:

$$(0A) + NC \rightarrow (NX) + (N + 2\delta_{XB})Si - E_r(NX) \tag{5.5}$$

and

$$(0X) + NC \rightarrow (NX) + NSi - E_f(NX). \tag{5.6}$$

The term δ_{XB} is 1 when configuration is labeled B and contains a missing dimer. In those reactions, Si is always in bulk phase, since Si bulk is the natural reservoir for Si atoms. Atoms can always be added to, or taken from bulk Si by means of step evolution. From the other hand, an *a priori* choice for the phase of C (and hence μ_C) is not possible without reference to particular experiment. For this purpose, we calculate the energies of the structures as *a function* of μ_C in the range from 0 (energy of a C atom) to -7.37 eV, the cohesive energy of diamond.

5.3 Structural properties and energetics

The relaxed geometries for all six configurations described in Section 5.1 are shown in Fig. 5.2. Their relative and formation energies are shown in Table 5.1, where μ_C is taken as the energy of a C atom in diamond. The second row of Table 5.1 shows the position of C in the $c(4 \times 4)$ unit cell, according to the numbering

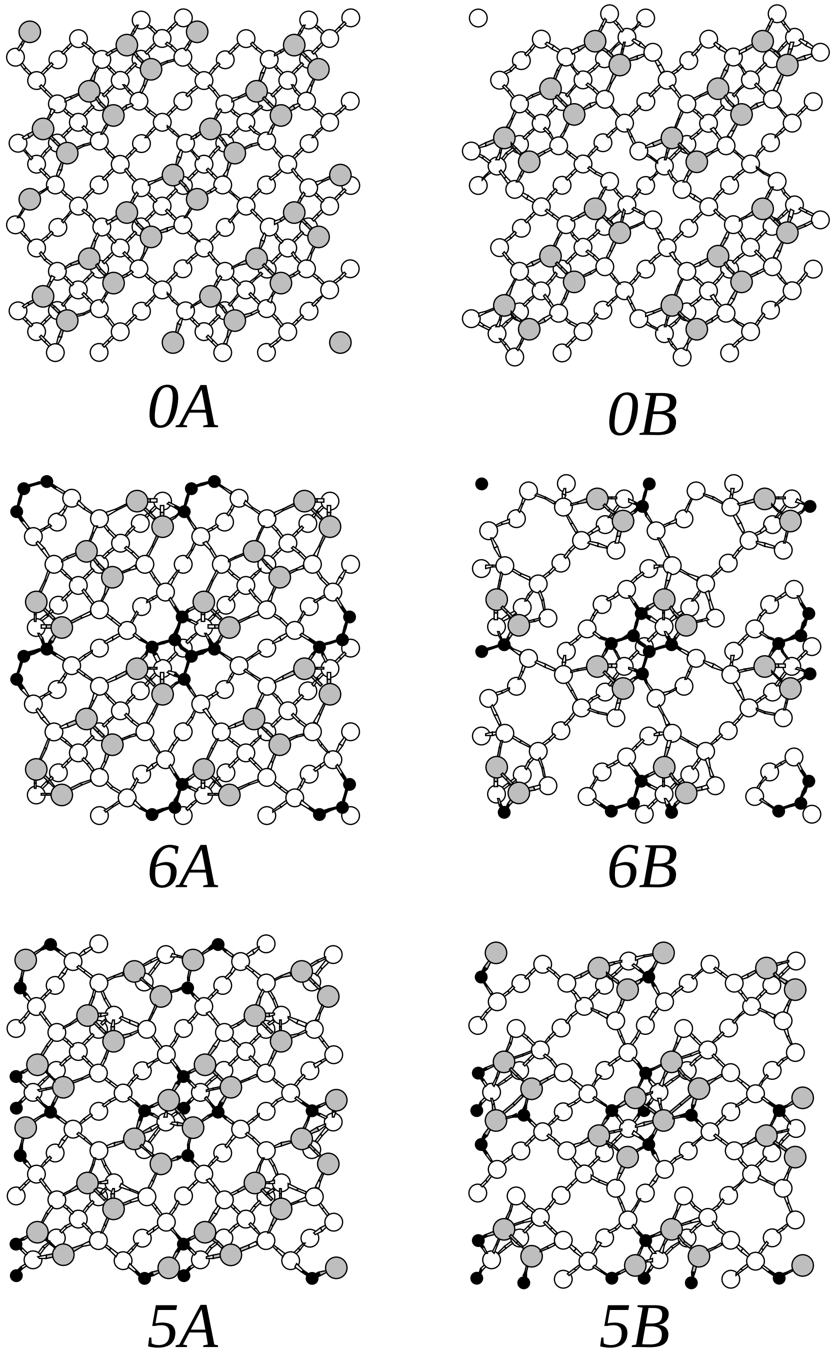

Figure 5.2: Relaxed geometries (top views, topmost four layers shown) of the configurations discussed in the text. A supercell four times the $c(4 \times 4)$ unit cell is shown. The configurations on the right column, marked B contain a dimer vacancy defect. Si surface atoms are shown as grey spheres, Si atoms of the 2nd, 3rd and 4th layer are shown as smaller, white spheres; C atoms are represented by black spheres.

scheme of Fig. 5.1. We first compare the energies of configurations with same C content; we then compare cells of different C content, discussing the dependence of the energies in C chemical potential, given in Fig. 5.3.

In configuration $0B$, the missing dimer is in the center of the frame. The second layer dimer atoms below the dimer form elongated bonds (not drawn in Fig. 5.2) of length 2.73 Å, 16% longer than the bulk bond length of Si (2.35 Å), in agreement with the calculated length of 2.79 Å by Wang *et al.* [139]. The calculated formation energy of the defect, 0.25 eV per missing dimer, is in excellent agreement with calculated values of 0.22 eV [139] and 0.28 eV [110]. The dimers adjacent to the defect have lengths of 2.33 Å, and are slightly longer than the other dimer of the unit cell (2.26 Å). For comparison, the calculated dimer bond length for configuration $0A$ is 2.34 Å. The bonds between the dimer atoms and the second layer atoms are elongated to 2.45 Å on average; they are 2.35 Å on average in $0A$. The dimers next to the defect are parallel to the surface, eliminating the characteristic buckling of the (2×1) reconstruction. The bond angles are also restored close to the tetrahedral value in the missing dimer configuration. There are two competing effects in this configuration: the reduction of dangling bonds from 8 (in $0A$) to 6 per unit cell and the restoration of bond angles, which lowers the total energy, and the distortion of bond lenghts, which raises the total energy. This competition results in the calculated very low energy difference between $0A$ and $0B$.

Configuration $6A$ contains 6 C atoms at first nearest neighbor positions. Two of them form a C-C dimer of length 1.51 Å, slightly shorter than the bulk bond length in diamond of 1.54 Å. The other four dimer atoms are each connected to a C atom of the dimer (bond length 1.58 Å), a Si atom of a Si-Si dimer (bond length 2.01 Å), and two Si atoms of the third layer (bond lengths 2.06/1.97 Å). All C-Si bonds are longer compared to the Si-C bond in $\beta-$SiC, which is 1.89 Å. The Si-Si dimers neighboring the C-C dimer have same length as the dimers on pure Si(100) ($0A$). The other Si-Si dimer is elongated, its length being 2.37 Å. All three dimers of configuration $6A$ are flat.

In $6B$, which is the same as $6A$ with a missing dimer, the C-C dimer is shorter (1.45 Å); at the same time, the angles formed by the C atoms of the dimer are very close to 120°, indicating that the C atoms are both in an sp^2 hybridized state. The bond lengths of a second-layer C atoms with a C atom of the C-C dimer are 1.55 Å long, almost unstretched. The C-Si bonds are also closer to the SiC bond length compared to configuration 6A. Because stretching or bending of the C-C bonds costs more energy than destorting Si-C or Si-Si bonds, the system gives priority to the satisfaction of the C bonds. This results in the twisted dimers shown in Fig. 5.2; the dimers are tilted and have length very close to the dimer length in pure Si(100).

The missing dimer allows for this relaxation to take place, relieving in this way the strain introduced by the large C content of the unit cell. This is the reason for the lower energy of configuration $6B$ compared to $6A$.

Configuration $5A$ contains 5 C atoms at second-nearest neighbor positions, forming a small SiC cluster below a Si-Si dimer. The symmetry of the $c(4 \times 4)$ reconstructed Si(100) has broken, and the dimer above the SiC cluster moves to the left, as shown in the relative panel of Fig. 5.2. As a result, the four dimers of the unit cell have all different lengths. The dimer above the C atoms is tilted and elongated (2.41 Å); the same applies to the dimer that has come close to it (length 2.40 Å). The other dimer connected to C atoms is shorter (2.32 Å), while the fourth dimer, which is not connected to C atoms is flat and 2.38 Ålong.

The C atoms lying between the two dimers that has come close to each other form bonds of lengths betwen 1.82 and 2.00 Å, with angles between 115° and 122°; apparently, they are in an sp^2 hybridized state, forming strong π bonds with the surrounding Si atoms. The arrangement of C atoms is thus qualitatively different from that of bulk SiC, where π bonding is absent. The other C atom in the fifth layer forms four bonds of lengths 1.88, 1.94, 1.94 and 1.99 Å, as close to the bond length in bulk SiC as the system can allow.

In configuration $5B$, obtained from $5A$ by removing a dimer, we observe the same symmetry breaking as in $5A$. The dimer above the C atoms has moved from its symmetrical position, and is again elongated (2.40 Å). The dimer close to it is 2.36 Å long, while the other one is 2.50 Å long. Again, the C atoms in the second layer are close to an sp^2 configuration, but this time the angles have a more broad dispersion from 120°, indicating an intermediate hybridization of C. The other C atom in the fifth layer forms bonds of almost identical lengths and angles as in $5A$. The distance between two Si atoms of the second layer at the dimer vacancy site is 4.83 Å, meaning that no bond has formed.

In contrast to the case with 6 C atoms per unit cell, for 5 C atoms the presence of the missing dimer does not lower the energy of the system. Configuration $5B$ has lower relative energy than $5A$ by 0.59 eV per unit cell. The difference in formation energies is smaller, 0.35 eV per unit cell.

In Fig. 5.3 we plot the relative energies of the considered structures as a function of the C chemical potential, or equivalently, the free energy per C atom of the C reservoir. We observe three changes in the preferred configuration: For low μ_C, where C is strongly bound, $0A$ is the lowest energy structure. For this region of μ_C it is costly energetically to remove C from the reservoir and add it to the sytem. The first transition happens for $\mu_C \approx -6.8$ eV. From this point, configuration $5A$ is the energetically favorable one, up to $\mu_C \approx -3.6$ eV where configuration $6A$ becomes the

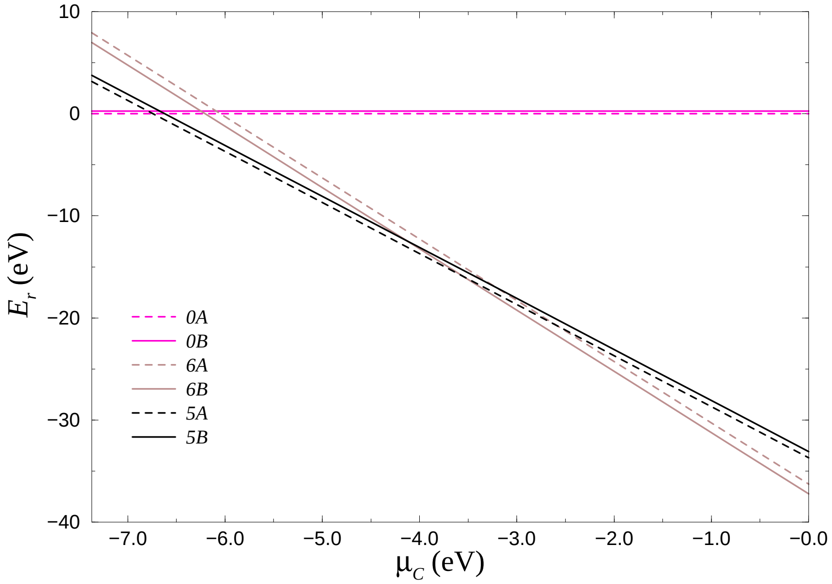

Figure 5.3: Relative energies of the considered structures, according to Eq. (5.3), as a function of the C chemical potential, as derived from the *ab initio* calculation at zero temperature.Energies are given in eV per $c(4 \times 4)$ unit cell.

one having the lowest energy. As we move to lower values of the chemical potential, it becomes easier to remove C atoms from the reservoir, and because C forms stronger bonds than Si, structures with larger C content are favored.

The chemical potential of C is the free energy per atom, relative to a free C atom, in the C reservoir with which the system is in thermal equilibrium. It can be either a solid, which is represented here by diamond, a typical form of solid C, or it can be a gas of C clusters. The latter is most likely the case in chemical vapor deposition (CVD) experiments. Carbon clusters C_n with $4 \leq n \leq 32$ have cohesive energies in the range between -7.1 and -5.2 eV per atom [52], while all structures with $n < 20$ have cohesive energies above -6 eV per atom. So in conditions of ordinary CVD experiments, the configuration $5A$ will be favored. In molecular beam epitaxy (MBE) growth, the C beam can in principle consist of single atoms or very small clusters consisting of two or three C atoms; in such cases, configuration $6B$ is expected to appear.

In order to determine the thermodynamics of the system, we performed finite temperature Monte Carlo simulations by the method described earlier, at 800 K. The calculated free energy differences are shown in Table 5.1. We find exactly the same ordering for the relative energies as in the *ab initio* calculation, which is performed at zero temperature. The relative free energies are slightly higher, which can be interpreted as the structures being less favorable at the elevated temperature. The two transition points discussed before are in the Monte Carlo calculation shifted to approximately -6.5 eV for the transition from $0A$ to $5A$ and -2.5 eV for the transition from $5A$ to $6B$.

5.4 Simulated STM images

To make our simulations readily comparable to experiment, we performed simulations of the STM images arising from each of the configurations studied here, using the Tersoff-Hamann theory as described in Section 5.2.1. The simulated STM images are shown in Fig. 5.4. They are all taken at a bias voltage of -2.5 eV, probing thus the occupied states of the system.

The pure Si(100) configuratons, $0A$ and $0B$ show the characteristic bean-shaped white dots above each dimer. In configuration $0B$, no signal is obtained above the missing dimer, because the topmost atoms in this region are much lower than the dimer atoms, and the tunneling current decreases exponentially with increasing tip-surface distance. This is the reason why some dimers appear brighter than the others, as their center lies higher by approximately 0.1 Å.

The simulated STM image for configuration $6A$ looks very similar to that for $0B$. The black region inside the dimer row corresponds to the C dimer, which is invisible in STM, due to the lower geometrical position and the lower energy of the bonding states of the C-C dimer compared to the Si-Si dimers [63, 72]. The two Si-Si dimers neighboring the C-C dimer are lower than the other one, which appears as a brighter spot. In configuration $6B$ this dimer is missing, so the only atoms appearing in the STM image are those belonging to the two Si-Si dimers. This image is essentially the same as that simulated by Leifeld *et al.* [72].

Configuration $5A$ gives an STM image very similar to that of $6B$. The large bright spot corresponds to the dimer that is not bonded to any C atom (see Fig. 5.2). The other white spot corresponds to the dimer that is bonded to two C atoms. The weak grey spot corresponds to the dimer bonded to four C atoms and lies above the SiC cluster. The fourth dimer of the unit cell, which is brought close to the one above the SiC cluster, does not give any measurable signal.

The simulated STM image for configuration $5B$ is qualitatively different from the others. The two large double spots correspond to second layer atoms, which would be bonded to a dimer, if there was no vacancy. Due to the presence of the vacancy and the strain inrtoduced by C, those atoms have come higher than the dimers (see Fig. 5.2). The other spot between them corresponds to the Si dimer bonded to four C atoms; the other two Si dimers of the unit cell are invisible. There

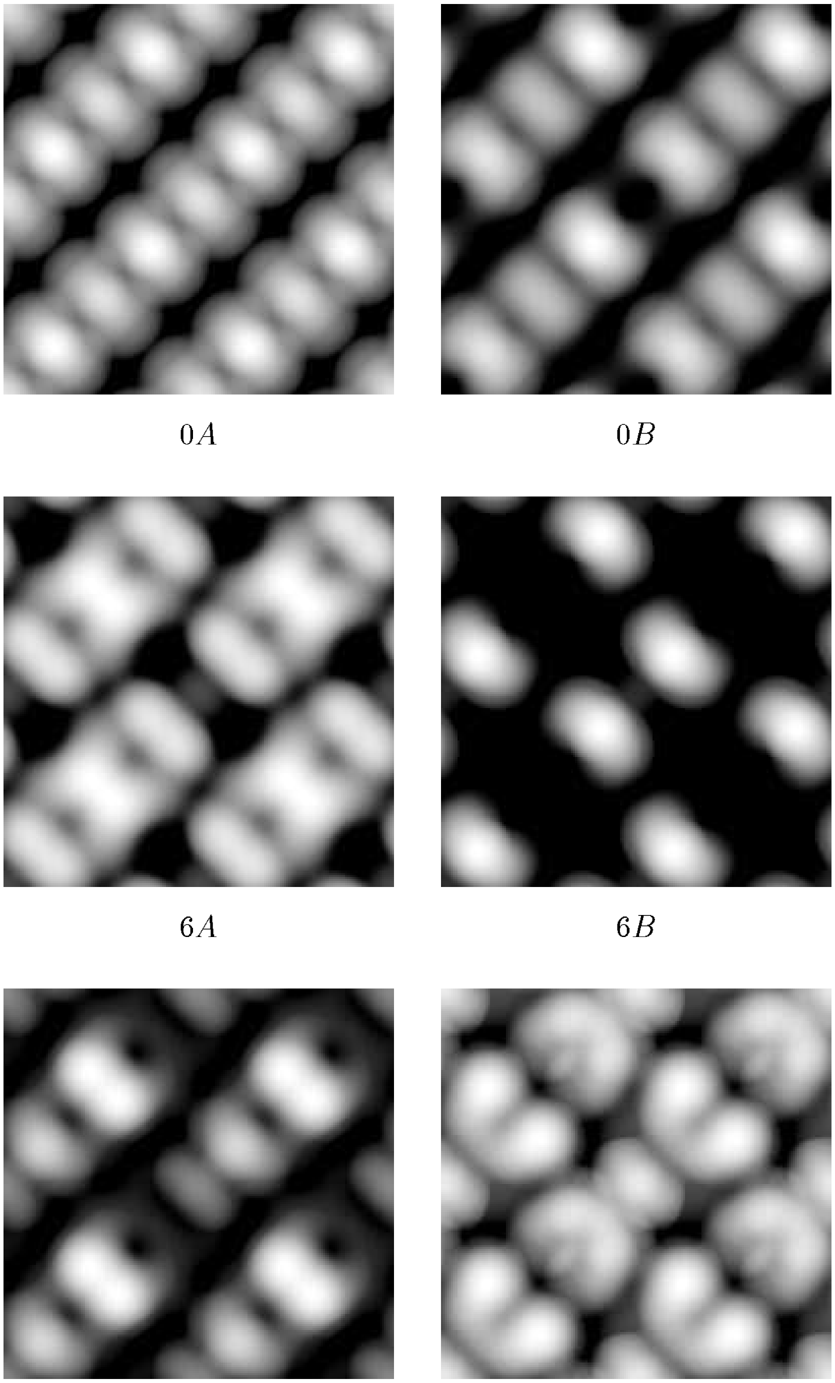

$0A$ $0B$

$6A$ $6B$

$5A$ $5B$

Figure 5.4: Simulated STM images for all configurations of Fig. 5.2. Constant-current mode at a bias voltage of -2.5 V, occupied stades probed.

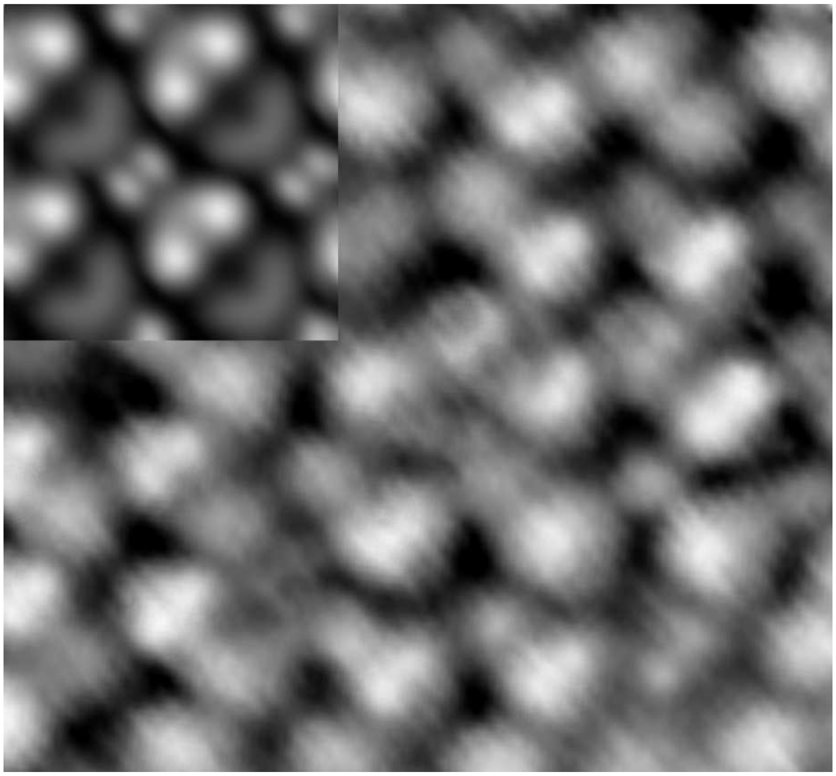

Figure 5.5: High-resolution experimental STM image from C-alloyed Si(100).

is an asymmetry in the four second layer atoms around the vacancy, as two of them are higher than the other two, so one pair of bright spots appears brighter than the other.

An experimental image of the C-alloyed Si(100) is shown in Fig. 5.5. The image is taken by the group of D. Grützmacher and is similar to that published by Leifeld *et al.* [72]. The bias voltage is -2V and the current is 0.2nA. The image contains characteristic pairs of spots arranged in a $c(4 \times 4)$ pattern. Both simulated STM images for $6B$ and $5A$ match this feature. The simulated image for $5A$ has the advantage of capturing the assymetry between the brightness of the two spots. The elongated structure shown in the middle of the picture could be attributed to a $5B$ cell.

In a recent STM experiment published bu Maeng and Kim [78], the observed STM images show both characteristics of our simulated STM images for $6A$ and $6B$; those structures are proposed as those producing the observed image. The relatively high energy difference between the two configurations renders their coexistence questionable. A co-existence of $5A$ and $6B$ would be more consistent with our results.

To make the comparison with experiment more quantitative, we calculate the

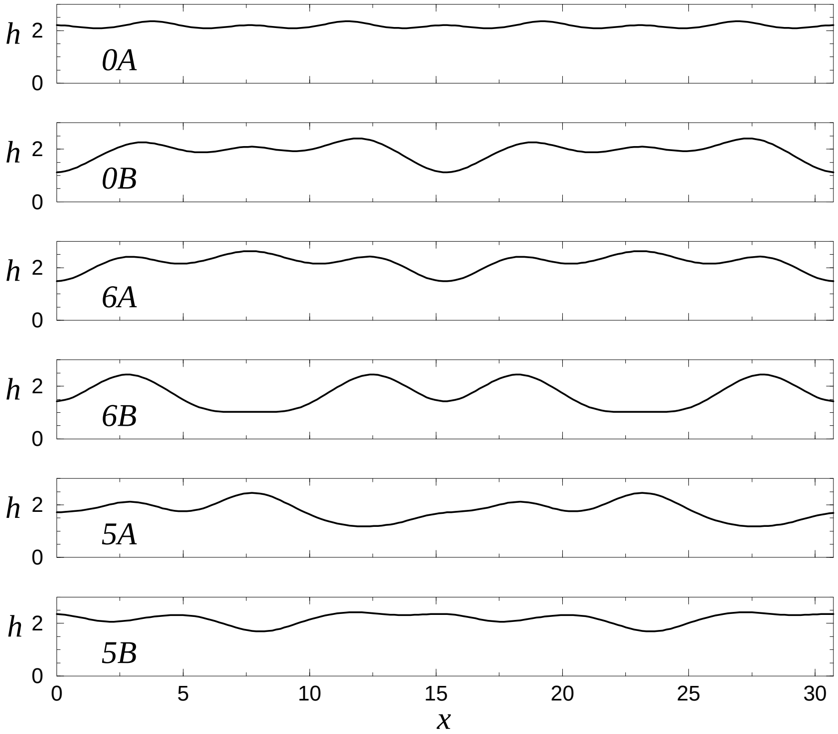

Figure 5.6: Average profiles of the simulated STM images of Fig. 5.4 along the dimer row. x is the distance (in Å) from the lower left corner of each image in Fig. 5.4, and h is the height (in Å) from the topmost atom of the surface.

distances between the pairs of spot in the simulated images. To do this, we first plot a cross-section of the simulated STM image. Fig. 5.6 shows cross-sections of the simulated STM images along the dimer row, averaged over a width of ±1.9Å around the dimer line. We define the intrapair distance as the distance between the two highest maxima in the unit cell, and the interpair distance as the distance between the second peak and the next one, which belongs to the adjacent unit cell. The experimental values for intrapair and interpair distances are 5.9 and 9.6 Å, respectively.

For $0A$, these distances are both 7.72 Å, the distance of two second-nearest neighboring dimers, which equals the lattice separation of the $p(2 \times 2)$ unit cell. In $0A$ the missing dimer has brought the remaining dimers closer, and the intrapair (interpair) distance is 6.9(8.5)Å, respectively.

For $6A$ the calculation is meaningless, as the two less bright spots surrounding the brighter one correspond exactly to the same height. For $6B$, we find an intrapair distance of 5.6 Å and and interpair distance of 9.8Å, values that agree very well with experiment. For $5A$ we find an intrapair distance of 4.8 Å, and an interpair distance of 10.6 Å. In this case the two spots are closer compared to $6B$. Finally, for $5B$ we find a larger separation of spots by 6.9Å and a smaller interpair distance of 8.5Å.

The calculated intrapair distance for the configurations with 5 C atoms per unit cell is smaller than the experimental by 1.1 Å for $5A$ and larger than the experimental by 1.0Å for $5B$. Because those two configurations were found to have formation energies differing by only 0.35 eV per unit cell, coexistence of the two could account for the observed length, since they produce STM images that match better the experimental image than configuration $6B$, which agrees exactly with the observed distances between spots, but does not reproduce the assymetry in their brightness.

5.5 Conclusions

When C is incorporated into Si(100) at high content, structures involving C atoms at first- or second-nearest neighbor positions are necessary to be considered in order to explain the observed STM images. We propose four such configurations here, two of which contain a missing dimer. The energetics show that according to the experimental conditions, the favorable structure will be either one with C atoms at second nearest neighbor positions (configuration $5A$) or one with C atoms at first nearest neighbor positions, involving a C-C dimer and a missing Si dimer (configuration $6B$). The simulated STM images for both configurations look reasonably similar to the observation; a higher resolution experimental SMT image would resolve the conflict.

Chapter 6

Reduction of NO on $MoO_3(010)$

We present density-functional theory pseudopotential calculations for modeling of the intermediate stages of the reduction of NO in the presence of $MoO_3(010)$. In particular, we study the formation of dinitrosyl, which proves to be an important intermediate stage in the catalytic reduction. We find that the replacement of an oxygen of MoO_3 by NO is energetically favorable, and that the system lowers further its energy by the formation of $(NO)_2$. Moreover, the geometry and charge distribution for the adsorbed dinitrosyl indicates a metal-oxide mediated coupling between the two nitrogens and the two oxygens. We discuss the mechanisms for the dinitrosyl formation and the role of the oxide in the reaction.

Reduction of nitric oxide (NO) has been the focus of detailed studies for long time, because of the role of NO as pollutant in the atmosphere. So-called three-way catalysts, based on Rh, Pt or PdO are used in automobile exhausts for this purpose; the activity of such catalysts was found to increase when molybdenum oxides were added [37, 144]. Recently, NO reduction products N_2 and O_2 were proposed to form nondissociatevely from NO via an adsorbed dinitrosyl species, which facilitates N-N coupling [103], as low temperature NO coupling was shown to proceed through a dinitrosyl intermediate [104]. The geometry of the adsorbed dinitrosyl and the mechanism of N-N coupling are though not known.

In this chapter, we perform density-functional theory calculations for various configurations involving nitrosyl and $MoO_3(010)$, including two characteristic configurations for dinitrosyl bound on the surface. First, we review the structure of MoO_3 and describe the method we use for the calculations. We present our results for $MoO_3(010)$ with an O vacancy, a structure with an exposed Mo atom which can adsorb NO molecules, followed by detailed analysis of the configurations involving adsorbed NO and $(NO)_2$. Finally, we discuss the dinitrosyl formation mechanisms and the role of $MoO_3(010)$ as a catalyst for the reduction of NO.

6.1 Molybdenum trioxide

Molybdenum trioxide is a layered material, its layers being weakly bonded via Van der Waals interactions. The space group is Q_h^{16} (bnm), and the lattice is orthorhombic [141] with parameters [142] 3.962, 13.858, and 3.697 Å. Each unit cell contains four MoO_3 units. The lattice coordinates of the atoms are $\pm(x, y, \frac{1}{4})$ and $\pm(\frac{1}{2} - x, \frac{1}{2} + y, \frac{1}{4})$. The values of x and y are [142] (0.086, 0.099) for Mo, and (0.086, 0.250), (0.586, 0.099), (0.586, 0.431) for the three surrounding O atoms.

The MoO_3 crystal is shown in Fig. 6.1. Macroscopically, the material forms "small, thin, lustrous plates, parallel to (010)" [141]. This is revealed in the atomistic structure: It consists of bilayers parallel to the (010) plane, which are bonded through weak electrostatic interactions, rendering (010) to be the easy cleavage plane of the crystal. Each bilayer consists of two sublayers of periodically arranged distorted MoO_6 octahedra. There are three structurally different O atoms. The *asymmetric bridging* oxygen is colinear with two Mo atoms and forms one long and one short bond with them. The *symmetric bridging* oxygen is located between the two sublayers of the bilayer and bonds to two Mo atoms of one sublayer with equal bond lengths and to one Mo atom of the adjacent sublayer with an elongated bond. Finally, the univalent *terminal* oxygen is connected to one Mo atom forming the shortest Mo-O bond in the system. The Mo-O bond lengths in MoO_3 as obtained from several

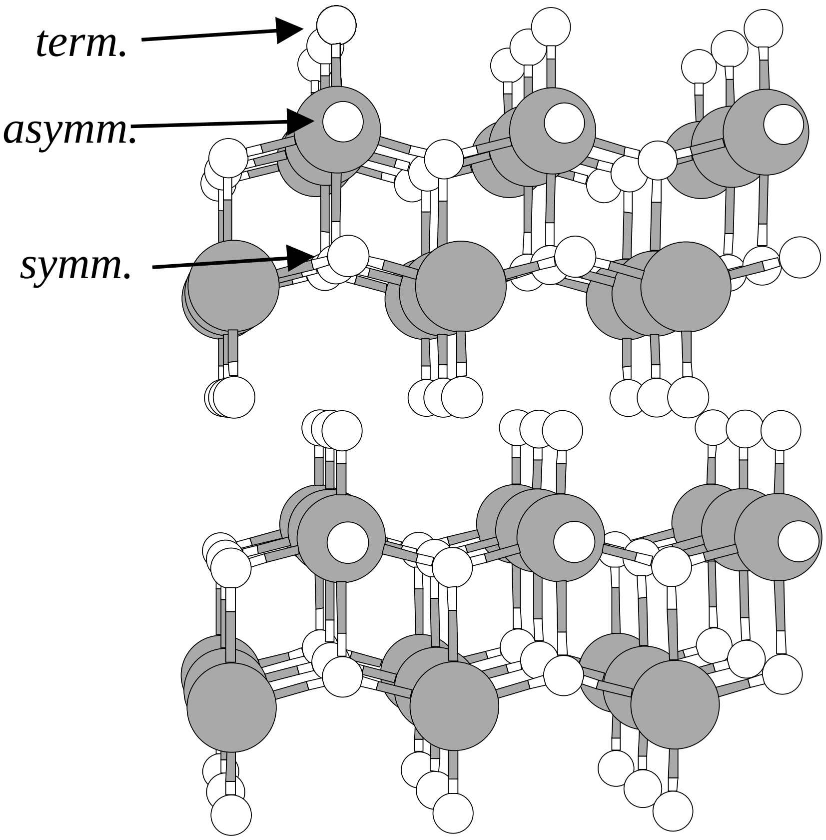

Figure 6.1: Structure of bulk MoO3. Mo atoms are shown in gray, O atoms in white. The three different types of O atoms (terminal, asymmetric bridging, symmetric bridging) are shown.

experimental and theoretical studies are shown in Table 6.1.

6.2 The calculation

All calculations were performed via the High-performance-fortran Adaptive Real-space Electronic Structure (HARES) package [82]. We use Density-Functional Theory (DFT) in the Local Spin Density Approximation (LSDA) [44, 66]. The Kohn-Sham valence electron wavefunctions are represented in a real-space orthogonal grid with a spacing of 0.13 Å, which is equivalent to a cut-off energy of 150 Ry in a plane-wave basis calculation[1]. The ionic cores and their interaction with valence electrons were taken into account through the soft Troullier-Martins [134] pseudopotentials,

---

[1] The effective cut-off for each direction is calculated from $E_C = \frac{\hbar^2\pi^2 n^2}{2m_e L^2}$, where L is the length of the simulation cell and n the number of grid points.

Table 6.1: Bond lengths (in Å) between Mo and O in MoO_3 as calculated in the present work for a single bilayer compared to other single bilayer calculations by Chen *et al.* [16], (a), and Yin *et al.* [145], (b), as well as experimental data obtained from the atomic positions given by Wyckoff [142], (c), and the experimental data by Kihlborg [64] as given in Ref. [16], (d). O_t, O_s and O_a stands for the terminal, symmetric bridging and asymmetric bridging O, respectively.

Bond	Bond Length				
	This work	Theory (a)	Theory (b)	Exp. (c)	Exp. (d)
Mo-O_t	1.77	1.67	1.76	1.82	1.67
Mo-O_s	1.96	1.92	2.02	1.93	1.95
	2.33	2.30	2.28	2.32	2.33
Mo-O_t	1.87	1.76	1.81	1.89	1.73
	2.17	2.19	2.25	2.08	2.25

in the separable Kleinman-Bylander form [65]. The Laplacian is expanded up to second order terms. For the exchange-correlation functional we use the results of Ceperley and Alder as they have been parametrized by Perdew and Zunger [13]. The electronic density was updated during the self-consistent loop using a modified Broyden mixer [48].

The system was modeled by a single bilayer of MoO_3, perpendicular to the (010) direction. This approximation is not expected to affect the results, due to the weak inter-layer coupling. The calculated Mo-O bond lengths for the system are shown in Table 6.1. Our results are in very good agreement with the bonds calculated from the atomic positions of Wyckoff [142] and those obtained from *ab initio* calculations by Yin *et al.* [145]. Moreover, vibrational frequencies calculated within the single bilayer approximation [16] are also in very good agreement with experiment, justifying our choice to use a simplified unit cell. The unit cell used has a (2×2) periodicity. This is sufficient to simulate isolated O vacancies or adsorbed NO, due to the local character of the substrate-adsorbate interaction and the lack of reconstruction effects for this surface.

The Brillouin Zone was sampled by Γ point only, which is enough due to the large size of the unit cell. The atomic degrees of freedom are relaxed with the Broyden-Fletcher-Goldfarb-Shanno (BFGS) method [17, 120] until the Hellman-Feynman forces were smaller than 0.005 a.u. We used symmetries to eliminate some electronic as well as ionic degrees of freedom were appropriate (see below). All the previous parameters have been checked, within either the present or previous works [82, 138], to give well-converged results.

6.3 Terminal O vacancy and NO adsorption

An O vacancy in MoO_3 is formed when a terminal oxygen atom is missing. As discussed in Section 6.1, the terminal O is univalent and forms the shortest Mo-O bond in the bulk material; this bond is also the strongest, as the calculated bond order is 1.93 [80]. It is then expected that the vacancy formation energy will be high. Indeed, our calculation yields 2.95 eV/vacancy, assuming that the O atoms that leave the surface form O_2 molecules (see Table 6.3). By using a (2×2) unit cell, we model a 0.25 ML coverage of vacancies. This coverage is low enough to ensure that the interactions between vacancies are negligible. The formation of vacancy is accompanied by small relaxations of atoms around the missing terminal O. The relaxed geometry is shown in Fig. 6.2(a). The main effect is an inwards displacement of the exposed Mo atom, which results in shrinking the Mo-symmetric oxygen bonds from 1.96 Å to 1.91 Å for O in the same sublayer and from 2.33 Å to 2.11 Å for O in the adjacent sublayer. No evidence for surface reconstruction is observed.

$MoO_3(010)$ with a terminal oxygen vacancy, shown in Fig. 6.2(a), has many characteristics of a good catalytic platform: The exposed Mo atom promises to be chemically active, and it has the ability to bond to more than one adsorbate, since it has lost a double bond. The remaining terminal oxygens around the vacancy form a cage structure that can enhance coupling between the adsorbates. In ideal MoO_3, the calculated [80] population for a terminal O is -0.4 electrons, so the remaining terminal O atoms are expected to repel the adsorbates, creating in this way an implicit attraction between them.

The first step in the catalytic reduction of NO is the adsorption of an NO molecule. We propose the binding configuration shown in Fig. 6.2(b), with NO binding to a Mo atom substituting a terminal O. The binding energy for NO to $MoO_3(010)$ with an oxygen vacancy is 2.98 eV/molecule. The molecule is perpendicular to the surface in the lowest energy geometry, rendering the nitrosyl dissociation on the surface implausible.

The adsorption of NO on MoO_3 with an O vacancy restores the positions of the surrounding atoms very close to their positions in the ideal MoO_3 (010). The energy difference between the $MoO_3(010)$ surface and the same surface with NO substituting a terminal O is -0.03 eV/molecule, assuming that the O atoms leaving the surface form O_2 molecules. The system lowers its total energy by the substitution of terminal O by NO, so this configuration must be an important step in the NO reduction.

The mechanism of the substitution and the formation of gas O_2 is not known, but it seems unlikely that the system passes from the O vacancy configuration, since

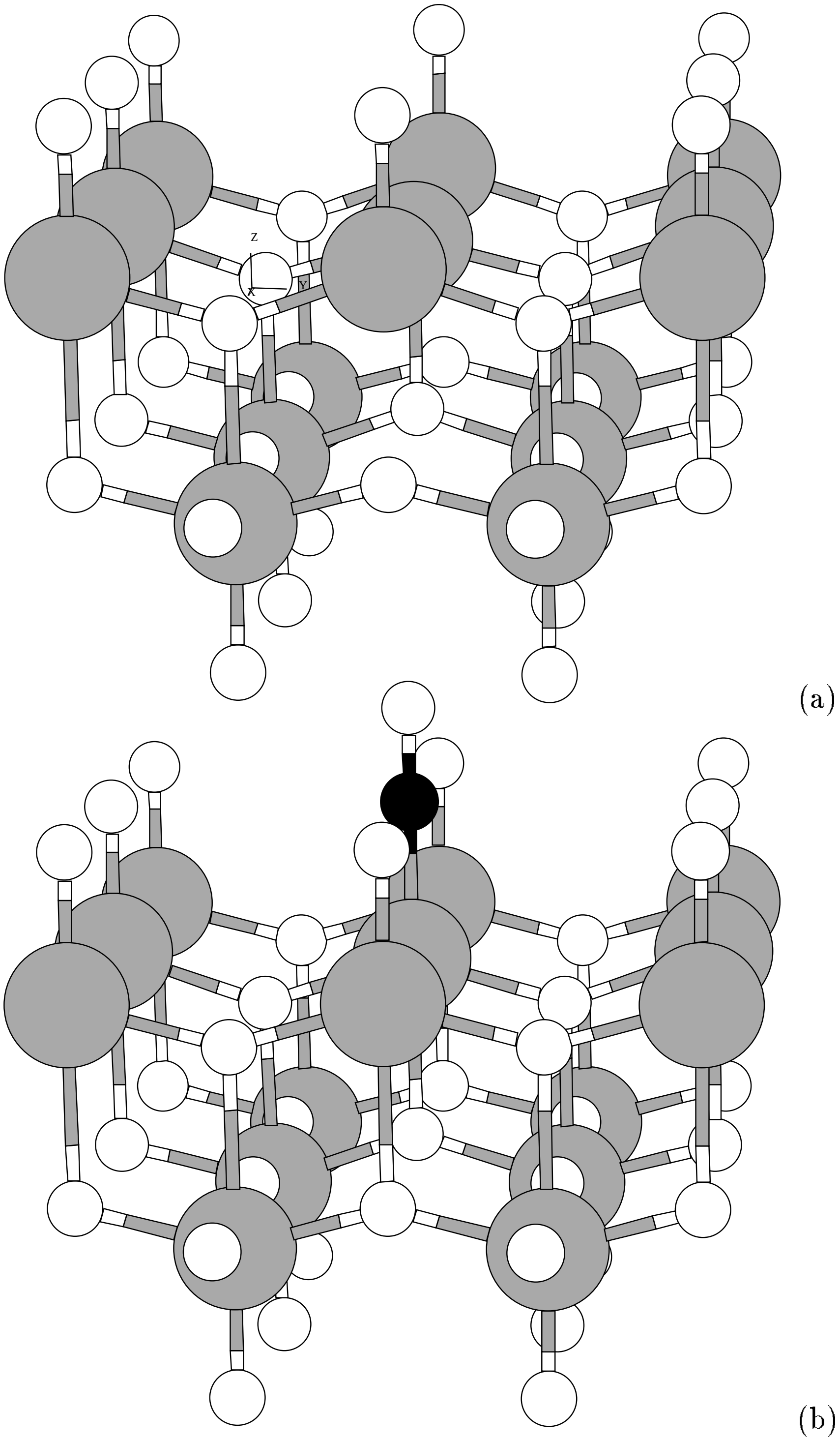

Figure 6.2: Relaxed geometries for MoO$_3$(010) (a) with a terminal O vacancy and (b) with an adsorbed NO molecule. Grey, white and black spheres correspond to Mo, O and N atoms, respectively.

the barrier of 2.95 eV is too high and would forbid the process under ordinary conditions. The transition state for the substitution could involve intermediate formation of NO_2 and/or O_3; in both cases removal of the extra O atom to form O_2 molecule would imply a much lower energy barrier.

In the lowest energy configuration shown in Fig. 6.2(b), the Mo-N bond has a length of 1.91 Å, longer than the Mo-terminal O bond. The N-O bond length is 1.14 Å, slightly shorter than the N-O bond length in a free NO molecule, which is 1.15 Å. The contraction of the NO bond can be attributed to the electrostatic attraction of the adsorbate by the surface. In classical electrodynamics, the attraction force between a point charge q at distance d from a surface is proportional to q^2/d^2. Using the calculated distances between Mo, N and O we find that the observed contraction comes from a 15% difference in the total charge around N and O. This difference can be explained in terms of the 13% electronegativity difference between the two elements (3.04 for N and 3.44 for 0).

6.4 Dinitrosyl chemisorption

To study the energetics of the dinitrosyl adsorption, we consider two characteristic configurations: In the first, the $(NO)_2$ plane is parallel to (001) or the molybdenum - symmetric bridging oxygen planes. In the second configuration, the $(NO)_2$ plane is parallel to (100), or the molybdenum - asymmetric bridging oxygen planes. The relaxed geometries for both configurations are shown in Fig. 6.3.

For the first case, a reflection symmetry with respect to the Mo-asymmetric O plane was imposed, following the experimental results obtained on oxidized Mo(110) [103]. Removal of the reflection plane does not result in further relaxation or significant lowering of the total energy; so in the lowest energy structure the two NO molecules of the dinitrosyl are identical. In contrast, $(NO)_2$ adsorbed parallel to the Mo-asymmetric O plane is found to be strongly asymmetric, with one of the two NO molecules being closer to the Mo center than the other. This is a direct consequence of the asymmetry of the underlying oxygen atoms.

The bond lengths for both configurations, together with the bond lengths of the previously discussed structures are summarized in Table 6.2. For adsorbed dinitrosyl in the Mo-symmetric O plane, the Mo-N bond is 2.00 Å long, 5% longer than in that of a single adsorbed NO. The Mo-N bond is weaker for adsorbed $(NO)_2$ as the bonding electrons of Mo are shared by two N atoms. The N-O bond length is 1.14 Å, identical to that of adsorbed NO. In the second configuration, having dinitrosyl in the Mo-asymmetric O plane, the Mo-N (N-0) bonds have lengths 1.95(1.15) and 2.35(1.13) Å, for NO above the long (2.18 Å) and short (1.90 Å) Mo-asymmetric O

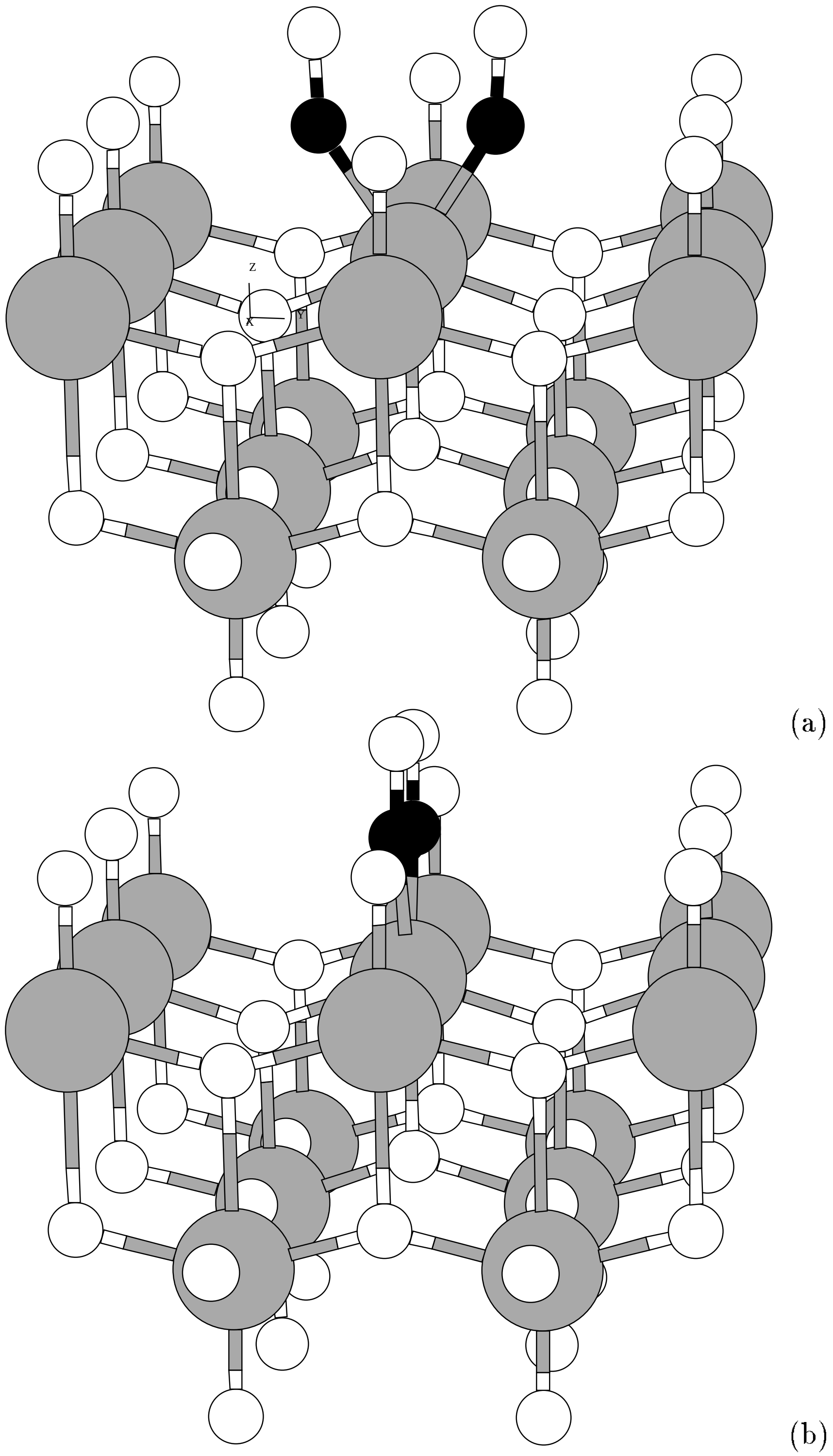

Figure 6.3: Relaxed geometries for dinitrosyl adsorption (a) in the symmetric O plane and (b) in the asymmetric O plane.

Table 6.2: Bond lengths (in Å) for the various structures discussed in the text. O_t, O_s and O_a stands for the terminal, symmetric bridging and asymmetric bridging O, respectively. The Mo-O_s bonds for Mo and O_s belonging at the same or adjacent sublayers, as well as the short and long Mo-O_a bond are shown. (s) and (a) indexes for adsorbed $(NO)_2$ refer to adsorption with the molecule parallel to the symmetric and asymmetric bridging O planes, respectively.

Structure	Mo - O_t	Mo-O_s		Mo-O_a		Mo-N	N-O	N-N
		same	adj.	short	long			
Ideal	1.77	1.96	2.33	1.87	2.17	-	-	-
O vacancy	1.77	1.91	2.11	1.90	2.06	-	-	-
ads. NO	1.77	1.95	2.23	1.86	2.15	1.91	1.14	-
ads. $(NO)_2$(s)	1.78	1.98	2.36	1.89	2.16	2.00	1.14	2.18
ads. $(NO)_2$(a)	1.78	1.96	2.29	1.90	2.18	1.95	1.15	2.21
						2.35	1.13	

bond, respectively. Both N and O of the adsorbed nitrosyls are more strongly bound above the less strongly bonded asymmetric O.

The asymmetric configuration, with $(NO)_2$ parallel to the Mo-asymmetric O plane, has a slightly lower energy than the other, by 0.10 eV per $(NO)_2$ molecule. The binding energy to $MoO_3(010)$ with an oxygen vacancy is 3.80 eV and 3.90 eV per molecule for the symmetric and asymmetric configuration, respectively. The energy gain when $(NO)_2$ substitutes a terminal O of $MoO_3(010)$ with formation of gas O_2 is 0.85 eV and 0.95 eV per molecule for the two configurations. This is an important lowering of the total energy of the system, as it is comparable to the dissociation energy of NO, 1.98 eV per pair of molecules.

The large lowering of the total energy by 0.90 eV on average per molecule for $(NO)_2$ adsorption, compared to 0.03 eV per NO for the NO adsorption, indicates that bonding between the two parts of the dinitrosyl has taken place. This bonding is evident in Fig. 6.4 showing a contour plot of the total electronic density minus a superposition of atomic electronic densities on the dinitrosyl plane, which coincides with the symmetric bridging O plane. The zero value of the density corresponds to the color used at the vacuum region near the top and bottom of the figure. Darker colors indicate negative values, corresponding to regions where charge depletion has happened in favor of the regions marked with lighter color in Fig. 6.4, where extra charge is accumulated. The T-shaped clouds inside the slab correspond to symmetric bridging O atoms, while those at the bottom to terminal O atoms. Small gray spots in the middle of black regions correspond to Mo atoms. The two bright vertical

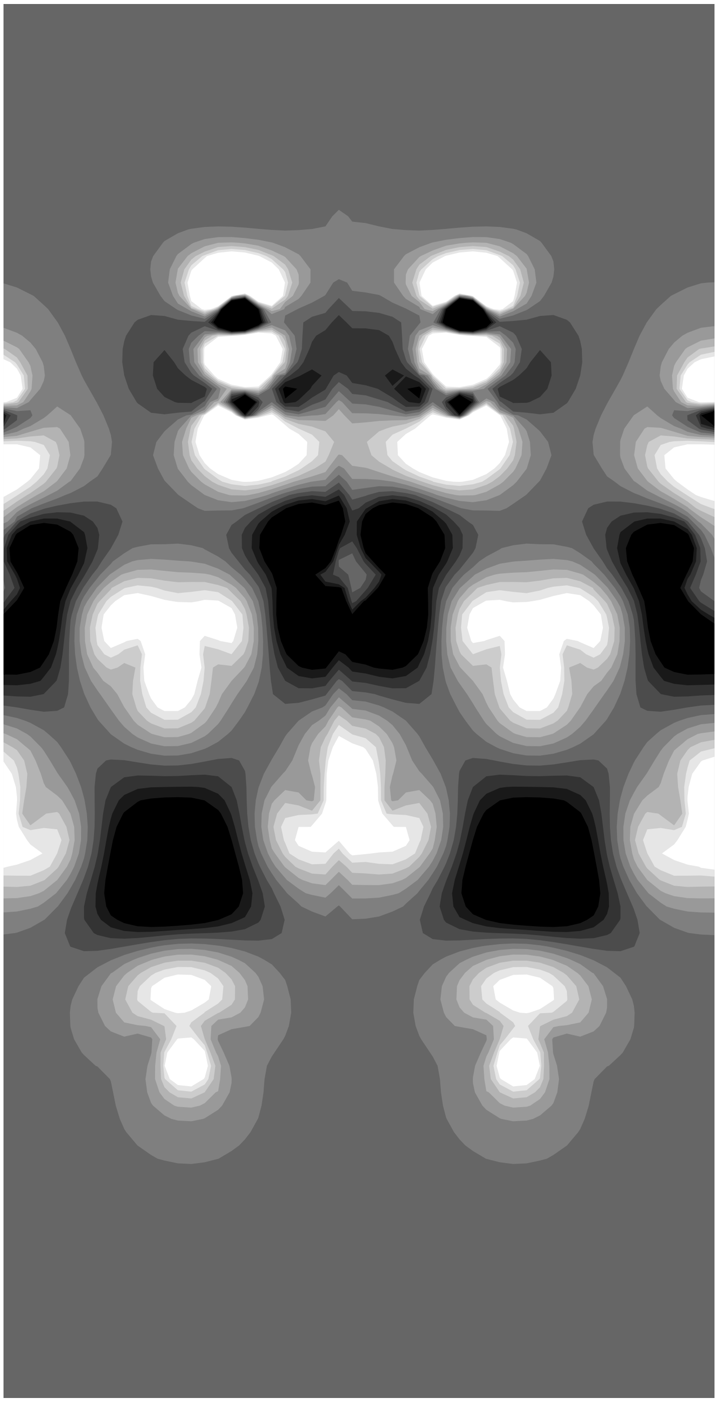

Figure 6.4: Contour plot of total electronic density minus a superposition of valence atomic charge densities in the Mo-N-O plane for adsorbed $(NO)_2$ parallel to the symmetric O plane. Dark gray (as the color near the top and bottom of the figure) corresponds to zero; darker colors correspond to negative values, lighter colors to positive values.

Table 6.3: Energetics of the reactions discussed in the text, as calculated in the present work. $MoO_3(010)_v$ refers to a $MoO_3(010)$ surface with a terminal O vacancy; (g) stands for gas-phase molecule and (a) for adsorbed molecule. The two numbers in the reactions involving adsorbed dinitrosyl refer to the two configurations mentioned in Section 6.4.

$$\begin{gathered}
\underline{\text{Vacancy formation:}} \\
MoO_3(010) \rightarrow MoO_3(010)_v + \tfrac{1}{2}O_2(g)\ -2.95\text{ eV} \\
\underline{\text{NO adsorption:}} \\
MoO_3(010)_v + NO(g) \rightarrow MoO_3(010)_v + NO(a) + 2.98\text{ eV} \\
MoO_3(010) + NO(g) \rightarrow MoO_3(010)_v + NO(a) + \tfrac{1}{2}O_2(g)\ {+0.03}\text{ eV} \\
\underline{(NO)_2\text{ adsorption:}} \\
MoO_3(010)_v + 2NO(g) \rightarrow MoO_3(010)_v + (NO)_2(a) + 3.80/3.90\text{ eV} \\
MoO_3(010)_v + 2NO(g) \rightarrow MoO_3(010)_v + (NO)_2(a) + \tfrac{1}{2}O_2 + 0.85/0.95\text{ eV} \\
\underline{(NO)_2\text{ formation from adsorbed NO:}} \\
2(MoO_3(010)_v + NO(a)) \rightarrow MoO_3(010)_v + (NO)_2(a) + MoO_3(010)_v\ -2.14/2.04\text{ eV} \\
2(MoO_3(010)_v + NO(a)) + \tfrac{1}{2}O_2(g) \rightarrow MoO_3(010)_v + (NO)_2(a) + MoO_3(010) \\
+0.81/0.91\text{ eV} \\
MoO_3(010)_v + NO(a) + NO(g) \rightarrow MoO_3(010)_v + (NO)_2(a) + 0.82/0.92\text{ eV}
\end{gathered}$$

complexes correspond to the two NO molecules. As the electronegativities of the involved elements dictate, charge has moved from the Mo atoms to N and O atoms, with O atoms having slightly more charge concentrated around them compared to N atoms.

We observe an apparent electron exchange between the two N atoms, manifesting the N-N coupling due to the presence of the catalytic surface. A similar, but weaker, coupling exists between the O atoms of the dinitrosyl. The absence of bonding charge between the adsorbed NO atoms and the surrounding terminal atoms implies a repulsion between them and the dinitrosyl. It is this repulsion that leads to the attraction between the N atoms.

The reactions leading to dinitrosyl formation, starting either by gas phase NO or by adsorbed nitrosyl, are summarized in Table 6.3. Although the adsorption of two gas NO molecules to form a dinitrosyl is exothermic by 0.85/0.95 eV/molecule (the two numbers referring to the two characteristic geometries of the dinitrosyl discussed before), the process is expected to have a large energy barrier due to the repulsion of the NO molecules, which, having an electrical dipole moment, would prefer to have an antiparallel configuration. The combination of two adsorbed nitrosyls is also rejected as a mechanism for dinitrosyl formation, as the vacancy left behind makes the process energetically costly. Indeed, as shown in Table 6.3, this reaction is endothermic by more than 2 eV/molecule. The alternative is to fill the O vacancy by an O from the environment. In this case, the dinitrosyl formation is exothermic by 0.81/0.91 eV/molecule. This process, being the opposite of the NO adsorption, would involve the same transition state and consequently requires overcoming of the same energy barrier.

A lower energy barrier, and a slightly higher energy gain, is possible when a gas-phase NO molecule binds to an already adsorbed one (last reaction of Table 6.3). The energy barrier for this case has to be lower than in the previous one, since this process involves no breaking of bonds, while the terminal oxygens of MoO_3 surrounding the adsorbed NO will attract the N atom of the gas-phase NO. The calculated lowest energy, together with the expected low barrier, support the presumption that this is the dominant dinitrosyl formation mechanism.

Combining the previous results, the proposed mechanism for the reduction of NO is the following: A gas NO molecule is exchanged with a $MoO_3(010)$ terminal O, and the system lowers its energy by 0.03 eV. Another NO molecule binds to the already adsorbed one, lowering the energy of the system by about another 0.84 eV. The next step is either desorption of the two O atoms first (as O_2) and the two N atoms then (as N_2), or desorption of one O atom first and then of the N_2O molecule. In both cases, an O atom fills the O vacancy that is left behind so that the catalyst is left unchanged at the end of the process. The final state of the system, with N_2 and O_2 molecules is [74] 1.90 eV lower in energy than the initial state of two NO molecules. The contribution of the catalyst is the lowering of the energy barrier for the reaction, which is translated into raise of the reaction rate.

List of Figures

List of Tables

Bibliography

[1] L. C. Allen, *Electronegativity is the Average One-Electron Energy of the Valence-Shell Electrons in Ground-State Free Atoms*, J. Am. Chem. Soc. **111**, 9003 (1989).

[2] M. Aono, Y. Hou, C. Oshima, and Y. Ishizaw, *Low-Energy Ion Scattering from the Si(001) Surface*, Phys. Rev. Lett. **49**, 567 (1982).

[3] G. B. Bachelet, D. R. Hamann, and M. Schlüter, *Pseudopotentials that work: From H to Pu*, Phys. Rev. B **26**, 4199 (1982).

[4] W. Barvosa-Carter, A. S. Bracker, J. C. Culbertson, B. Z. Nosho, B. V. Shanabrook, L. J. Whitman, H. Kim, N. A. Modine, and E. Kaxiras, *Structure of III-Sb(001) Growth Surfaces: The Role of Heterodimers*, Phys. Rev. Lett. **84**, no. 20, 4649–4652 (2000).

[5] M. Biagini, *Comment on Generalized density functional theory*, J. Phys.: Cond. Mat **8**, 2233 (1996).

[6] G. Binnig, H. Rohrer, C. Gerber, and E. Weibel, *Surface Studies by Scanning Tunneling Microscopy*, Phys. Rev. Lett **49**, 57 (1982).

[7] F. Bloch, Zeits. f. Physik **52**, 555 (1928).

[8] M. Born and R. Oppenheimer, *Zur Quantentheorie der Molekulen*, Ann Phys **84**, 457 (1927).

[9] C. G. Broyden, *A Class of Methods for Solving Nonlinear Simultaneous Equations*, Math. Comp. **19**, 577–593 (1965).

[10] E. L. Bullock, R. Gunnella, L. Patthey, T. Abukawa, S. Kono, C. R. Natoli, and L. S. O. Johansson, *Surface Core-Level Photoelectron Diffraction from Si Dimers at the Si(001)-(2 x 1) Surface*, Phys. Rev. Lett. **74**, 2756 (1995).

[11] R. Butz and H. Lüth, *The surface morphology of Si (100) after carbon deposition*, Surf. Sci **411**, 61–69 (1998).

[12] R. Car and M. Parrinello, *Unified approach for molecular dynamics and density-functional theory*, Phys. Rev. Lett **55**, 2471 (1985).

[13] D. M. Ceperley and B. J. Alder, *Ground State of the Electron Gas by a Stochastic Method*, Phys. Rev. Lett. **45**, 566 (1980).

[14] Y. J. Chabal, S. B. Christman, E. E. Chaban, and M. T. Yin, *Surface state optical absorption on the clean Si(100) surface*, J. Vac. Sci. Technol. A **1**, 1241–1242 (1983).

[15] D. J. Chadi, *Atomic and Electronic Structures of Reconstructed Si(100) Surfaces*, Phys. Rev. Lett. **43**, 43–47 (1979).

[16] M. Chen, U. V. Waghmare, C. M. Friend, and E. Kaxiras, *A density functional study of clean and hydrogen-covered a-MoO_3(010): Electronic structure and surface relaxation*, J. Chem. Phys. **109**, no. 16, 6854–6860 (1998).

[17] N. Chetty, M. Weinert, T. S. Rahman, and J. W. Davenpor, *Vacancies and impurities in aluminum and magnesium*, Phys. Rev. B **52**, 6313 (1995).

[18] N. Choly and E. Kaxiras, *Kinetic energy density functionals for non-periodic systems*, http://arxiv.org/abs/cond-mat/0112040, (2001).

[19] A. Claverie, J. Faure, J. L. Balladore, L. Simon, A. Mesli, L. Kubler, M. Diani, and D. Aubel, *A particular epitaxial $Si_{1-y}C_y$ alloy growth mode on Si(001) evidenced by cross-sectional transmission electron microscopy*, J. Crys. Growth **157**, 420–425 (1995).

[20] J. Cordes and L. Fritsche, *Ground state and excitational properties of atoms*, Z. Phys. D **13**, 345 (1989).

[21] G. Davies and R. C. Newman, *Carbon in mono-crystalline silicon*, Handbook on Semiconductors (S. Mahajan, ed.), vol. 3, Elsevier Science, New York, 1994.

[22] J. Dąbrowski and H. Müssig, *Silicon Surfaces and Formation of Interfaces*, World Scientific, Singapore, 2000.

[23] K. Eberl, S. S. Iyer, J. C. Tsang, M. S. Goorsky, and F. K. Legoues, *The growth and characterization of $Si_{1-y}C_y$ alloys on Si(001) substrate*, J. Vac. Sci. Technol. B **10**, 934–936 (1992).

[24] M. Elstner, T. Frauenheim, E. Kaxiras, G. Seifert, and S. Suhai, *A self-consistent charge density-functional based tight-binding scheme for large biomolecules*, Phys. Stat. Soli. B **217**, 357 (2000).

[25] M. Elstner, D. Porezag, G. Jungnickel, J. Elsner, M. Haugk, T. Frauenheim, S. Suhai, and G. Seifert, *Self-consistent-charge density-functional tight-binding method for simulations of complex materials properties*, Phys. Rev. B **58**, no. 11, 7260–7268 (1998).

[26] R. Felici, I. K. Robinson, C. Ottaviani, P. Imperatori, P. J. Eng, and P. Perfetti, *Room temperature Si(001)-(2×1) reconstruction solved by X-ray diffraction*, Surf. Sci **375**, 55–62 (1997).

[27] L. Fritsche, *Generalized Kohn-Sham theory for electronic excitations in realistic systems*, Phys. Rev. B **33**, 3976 (1986).

[28] L. Fritsche, *Excitations in a generalized density functional theory*, Physica B **172**, 7 (1991).

[29] L. Fritsche, *Excited States and Electron-atom Scattering*, Density Functional Theory (E. K. U. Gross and R. M. Dreizler, eds.), Plenum Press, New York, 1995, pp. 119–147.

[30] L. Fritsche, *Reply to the comment by M Biagini on generalized density functional theory*, J. Phys.: Cond. Mat **8**, 2237–2242 (1996).

[31] L. Fritsche and Y. M. Gu, *Band gaps in a generalized density-functional theory*, Phys. Rev. B **48**, 4250 (1993).

[32] P. Fulde, *Electron Correlations in Molecules and Solids*, Springer-Verlag, Berlin, 1991.

[33] R. Godby, M. Schlüter, and L. Sham, *Accurate Exchange-Correlation Potential for Si and its discontinuity on addition of an electron*, Phys. Rev. Lett **56**, no. 22, 2415–2418 (1986).

[34] R. Godby, M. Schlüter, and L. Sham, *Self-energy operators and exchange-correlation potentials in semiconductors*, Phys. Rev. B **37**, no. 17, 10159–10175 (1988).

[35] C. Guedj, X. Portier, A. Hairie, D. Bouchier, G. Calvarin, B. Piriou, B. Gautier, and J. C. Dupuy, *Carbon self-organization in the ternary* $Si_{1-x-y}Ge_xC_y$ *alloy*, J. Appl. Phys. **83**, no. 10, 5251–5257 (1998).

[36] F. Gygi and A. Baldereschi, *Quasiparticle energies in semiconductors: Self-energy correction to the local-density approximation*, Phys. Rev. Lett **62**, 2160 (1989).

[37] I. Halasz and A. Brenner, *Catalytic reduction of nitric oxide on PdO-*MoO_3/γ*-*Al_2O_3, Appl. Catal. B **2**, no. 1, 131–146 (1993).

[38] D. R. Hamann, M. Schlüter, and C. Chiang, *Norm-Conserving Pseudopotentials*, Phys. Rev. Lett. **43**, no. 20, 1494–1497 (1979).

[39] R. J. Hamers and U. K. Köhler, *Determination of the Local Electronic Structure of Atomic-Sized Defects on Si(001) by Tunneling Spectroscopy*, J. Vac. Sci. Technol. A **7**, 2854 (1989).

[40] W. A. Harrison, *Electronic structure and the properties of Solids*, Dover, New York, 1989.

[41] K. Hata, S. Yasuda, and H. Shigekawa, *Reinterpretation of the scanning tunneling microscopy images of Si(100)-(2×1) dimers*, Phys. Rev. B **60**, 8164–8170 (1999).

[42] L. Hedin, *New method for calculating the one-particle Green's Function with application to the electron gas problem*, Phys. Rev **139**, no. 3A, A796–A823 (1965).

[43] F. J. Himpsel and E. D. Eastman, *Photoemission studies of intrinsic surface states on Si(100)*, J. Vac. Sci. Technol **16**, 1297–1299 (1979).

[44] P. Hohenberg and W. Kohn, *Inhomogeneous Electron Gas*, Phys. Rev. **136**, B864 (1964).

[45] M. Hybertsen and S. Louie, *First-principles theory of quasiparticles: Calculation of Band Gaps in Semiconductors and Insulators*, Phys. Rev. Lett. **55**, no. 13, 1418–1421 (1985).

[46] M. Hybertsen and S. Louie, *Electron correlation in semiconductors and insulators: Band gaps and quasiparticle energies*, Phys. Rev. B **34**, no. 8, 5390–5413 (1986).

[47] K. Inoue, Y. Morikawa, K. Terakura, and M. Nakayama, *Order-disorder phase transition on the Si(001) surface: Critical role of dimer defects*, Phys. Rev. B **49**, 14774 (1994).

[48] M. Jain, L. Kronik, and J. R. Chelikowsky, *On charge density mixers*, to be published.

[49] F. Jensen, *Introduction to Computational Chemistry*, Wiley & sons, Chichester, England, 1999.

[50] L. S. O. Johansson and B. Reihl, Surf. Sci. **269/270**, 810 (1992).

[51] D. D. Johnson, *Modified Broyden's method for accelerating convergence in self-consistent calculations*, Phys. Rev. B **38**, no. 18, 12807–12813 (1988).

[52] R. O. Jones, *Density functional study of carbon clusters* C_{2n} *(*$2 \leq n \leq 16$*). I. Structure and bonding in the neutral clusters*, J. Chem. Phys. **110**, 5189–5200 (1999).

[53] R. O. Jones and O. Gunnarsson, *The density functional formalism, its applications and prospects*, Rev. Mod. Phys. **61**, no. 3, 689–746 (1989).

[54] M. Kawata, C. M. Cortis, and R. A. Friesner, *Efficient recursive implementation of the modified Broyden method and the direct inversion in the iterative subspace method: Acceleration of self-consistent calculations*, J. Chem. Phys. **108**, no. 11, 4426–4438 (1998).

[55] E. Kaxiras, Y. Bar-Yam, J. Joannopoulos, and K. Pandey, *Variable stoichiometry surface reconstruction: new models for GaAs*$(\bar{1}\bar{1}\bar{1})2\times 2$ *and* $\sqrt{19} \times \sqrt{19}$, Phys. Rev. Lett. **57**, no. 1, 106–109 (1986).

[56] E. Kaxiras, K. Pandey, Y. Bar-Yam, and J. Joannopoulos, *Role of chemical potentials in surface reconstruction: A new model and phase transition on GaAs(111)2×2*, Phys. Rev. Lett. **56**, no. 26, 2819–2822 (1986).

[57] E. Kaxiras, *Semiconductor-surface restoration by valence-mending adsorbates: Application to Si(100):S and Si(100):Se*, Phys. Rev. B **43**, no. 8, 6824–6827 (1991).

[58] P. C. Kelires, *Monte Carlo Studies of Ternary Semiconductor Alloys: Application to the* $Si_{1-x-y}Ge_xC_y$ *System*, Phys. Rev. Lett. **75**, 1114 (1995).

[59] P. C. Kelires, *Simulations of Carbon containing semiconductor alloys: Bonding, strain compensation, and surface structure*, Int. J. Mod. Phys. C **9**, no. 2, 357–389 (1998).

[60] P. C. Kelires, *Theoretical investigation of the equilibrium surface structure of* $Si_{1-x-y}Ge_xC_y$, Surf. Sci. **418**, L62–L67 (1998).

[61] P. C. Kelires and E. Kaxiras, *Energetics and Equilibrium Properties of Thin Pseudomorphic* $Si_{1-x}C_x$*(100) Layers in Si*, Phys. Rev. Lett. **78**, 3479–3482 (1997).

[62] P. C. Kelires and J. Tersoff, *Equilibrium alloy properties by direct simulation: Oscillatory segregation at the Si-Ge(100) 2×1 surface*, Phys. Rev. Lett. **63**, 1164 (1989).

[63] P. C. Kelires and E. Kaxiras, *Substitutional carbon impurities in thin silicon films: Equilibrium structure and properties*, J. Vac. Sci. Technol. B **16**, no. 3, 1687–1691 (1998).

[64] L. Kihlborg, Ark. Kemi **21**, 357 (1963).

[65] L. Kleinman and D. M. Bylander, *Efficacious Form for Model Pseudopotentials*, Phys. Rev. Lett. **48**, 1425 (1982).

[66] W. Kohn and L. J. Sham, *Self-Consistent Equations Including Exchange and Correlation Effects*, Phys. Rev. **140**, A1133 (1965).

[67] G. Kresse and J. Furthmüller, Comput. Mat. Sci. **6**, 15–50 (1996).

[68] G. Kresse and J. Furthmüller, *Efficient iterative schemes for ab initio total-energy calculations using a plane-wave basis set*, Phys. Rev. B **54**, 11169–11186 (1996).

[69] G. Kresse and J. Hafner, *Ab initio molecular dynamics for liquid metals*, Phys. Rev. B **47**, 558–561 (1993).

[70] G. Kresse and J. Hafner, *Norm-conserving and ultrasoft pseudopotentials for first-row and transition elements*, J. Phys.: Condens. Matter **6**, 8245 (1994).

[71] E. V. Lavrov, B. B. Nielsen, J. R. Byberg, B. Hourahine, R. Jones, S. Öberg, and P. R. Briddon, *Local vibrational modes of two neighboring substitutional carbon atoms in silicon*, Phys. Rev. B **62**, 158–165 (2000).

[72] O. Leifeld, D. Grützmacher, B. Müller, K. Kern, E. Kaxiras, and P. C. Kelires, *Dimer-pairing in the C-alloyed Si(100)*, Phys. Rev. Lett. **82**, 972 (1999).

[73] O. Leifeld, R. Hartmann, E. Müller, E. Kaxiras, K. Kern, and D. Grützmacher, *Self-organized growth of Ge quantum dots on Si(001) substrates induced by sub-monolayer C coverages*, Nanotechnology **10**, no. 2, 122–126 (1999).

[74] D. R. Lide (ed.), *Handbook of Chemistry and Physics*, CRC Press, Boca Raton, FL, 2000.

[75] K. C. Low and C. K. Ong, *Electronic structure of the Si(100)* $c(4 \times 2)$ *and* $p(2 \times 2)$ *surfaces*, Phys. Rev. B **50**, 5352 (1994).

[76] H. Lüth, *Solid Surfaces, Interfaces and Thin Films*, 4th ed., Springer, Berlin, 2001.

[77] O. Madelung (ed.), *Semiconductors- Basic Data*, Springer, Berlin, 1996.

[78] J. Y. Maeng and S. Kim, *Scanning tunneling microscopy study on c(4×4) structure of Si(100)*, Surf. Sci **482-485**, no. 2, 1445–1450 (2001).

[79] N. Metropolis, A. W. Rosenbluth, M. N. Rosenbluth, A. H. Teller, and E. Teller, J. Chem. Phys. **21**, 1087 (1953).

[80] A. Mihalak, K. Hermann, and M. Witko, *Reactive oxygen sites at* MoO_3 *surfaces: ab initio cluster model studies*, Surf. Sci. **366**, 323–336 (1996).

[81] K. Miki, K.Sakamoto, and T. Sakamoto, *Is the* c(4×4) *reconstruction of Si(001) associated with the presence of carbon?*, Appl. Phys.Lett. **71**, 3266–3268 (1997).

[82] N. A. Modine, G. Zumbach, and E. Kaxiras, *Adaptive-coordinate real-space electronic-structure calculations for atoms, molecules, and solids*, Phys. Rev. B **55**, 10289–10301 (1997).

[83] W. Mönch, *Semiconductor surfaces and interfaces*, 2nd ed., Springer, Berlin, 1995.

[84] W. Mönch, P. Koke, and S. Kruger, *On the electronic structure of clean, 2×1 reconstructed silicon (001) surfaces*, J. Vac. Sci. Technol. **19**, 313–318 (1982).

[85] H. J. Monkhorst and J. D. Pack, *Special points for Brillouin-zone integrations*, Phys. Rev. B **13**, 5188 (1976).

[86] T. A. Niehaus, S. Suhai, F. D. Sala, P. Lugli, M. Elstner, G. Seifert, and T. Frauenheim, *Tight-binding approach to time-dependent density-functional response theory*, Phys. Rev. B **63**, 085108 (2001).

[87] J. E. Northrup, *Electronic structure of Si(100)* $c(4 \times 2)$ *calculated within the GW approximation*, Phys. Rev. B **47**, 10032–10035 (1993).

[88] H. Okada, Y. Fujimoto, K. Endo, K. Hirose, and Y. Mori, *Detailed analysis of scanning tunneling microscopy images of the Si(001) reconstructed surface with buckled dimers*, Phys. Rev. B **63**, 195324 (2001).

[89] H. Osten, M. Methfessel, G. Lippert, and H. Rücker, *Observation of the formation of a carbon-rich surface layer in silicon*, Phys. Rev. B **52**, 12179 (1995).

[90] H. J. Osten, E. Bugiel, and P. Zaumseil, *Growth of an inverse tetragonal distorted SiGe layer on Si(001) by adding small amounts of carbon*, Appl. Phys. Lett. **64**, 3440–3442 (1994).

[91] H. J. Osten, E. Bugiel, and P. Zaumseil, *Self-organization during* $Si_{1-y}C_y$ *alloy layer growth on Si(001) using homogeneous coevaporation*, J. Appl. Phys. **82**, 231–235 (1997).

[92] H. J. Osten, J. Griesche, P. Gaworzewski, and K. D. Bolze, *Influence of interstitial carbon defects on electron transport in strained* $Si_{1-y}C_y$ *layers on Si(001)*, Appl. Phys. Lett. **76**, no. 2, 200–202 (2000).

[93] H. J. Osten, D. Knoll, B. Heinemann, and P. Schley, *Increasing process margin in SiGe heterojunction bipolar technology by adding carbon*, IEEE Trans. Electron Devices **46**, 1910–1912 (1999).

[94] H. Over, J. Wasserfall, W. Ranke, C. Ambiatello, R. Sawitzki, D. Wolf, and W. Moritz, *Surface atomic geometry of Si(001)-(2×1): A low-energy electron-diffraction structure analysis*, Phys. Rev. B **55**, 4731 (1997).

[95] K. C. Pandey, *Reconstruction of Semiconductor Surfaces: Buckling, Ionicity, and* π *-Bonded Chains*, Phys. Rev. Lett. **49**, 223 (1982).

[96] L. Pauling, *The Nature of the Chemical Bond*, Cornell University Press, Ithaca, NY, 1960.

[97] M. C. Payne, M. P. Teter, D. C. Allan, T. A. Arias, and J. D. Joannopoulos, *Iterative minimization techniques for ab initio total-energy calculations: molecular dynamics and conjugate gradients*, Rev. Mod. Phys. **64**, no. 4, 1045–1097 (1992).

[98] J. P. Perdew, K. Burke, and Y. Wang, *Generalized gradient approximation for the exchange-correlation hole of a many-electron system*, Phys. Rev. B **54**, 16533 (1996).

[99] J. P. Perdew and A. Zunger, *Self-interaction correction to density-functional approximations for many-electron systems*, Phys. Rev. B **23**, no. 10, 5048–5079 (1981).

[100] J. P. Perdew and Y. Wang, *Accurate and simple density functional for the electronic exchange energy: Generalized gradient approximation*, Phys. Rev. B **33**, no. 12, 8800–8802 (1986).

[101] J. P. Perdew and Y. Wang, *Accurate and simple analytic representation of the electron-gas correlation energy*, Phys. Rev. B **45**, no. 23, 13244–13249 (1992).

[102] P. Pulay, Chem. Phys. Lett. **73**, 393 (1980).

[103] K. T. Queeney and C. M. Friend, *Dinitrosyl intermediate for* N_2O *formation from reaction of NO on Mo(110)*, J. Chem. Phys. **107**, 6432–6442 (1997).

[104] K. T. Queeney and C. M. Friend, *Conversion of nitrosyls to dinitrosyls during NO adsorption on oxygen-modified* MoO_3*(110)*, Surf. Sci. Lett. **414**, L957–L963 (1998).

[105] A. Ramstad, G. Brocks, and P. J. Kelly, *Theoretical study of the Si(100) surface reconstruction*, Phys. Rev. B **51**, 14504 (1995).

[106] A. M. Rappe, K. M. Rabe, E. Kaxiras, and J. D. Joannopoulos, *Optimized pseudopotentials*, Phys. Rev. B **41**, no. 2, 1227–1230 (1990).

[107] I. N. Remediakis and E. Kaxiras, *Si(100)*, in preparation.

[108] I. N. Remediakis and E. Kaxiras, *Band-structure calculations for semiconductors within generalized-density-functional theory*, Phys. Rev. B **59**, 5536 (1999).

[109] I. N. Remediakis, E. Kaxiras, and P. C. Kelires, *Thermodynamics of C Incorporation on Si(100) from ab initio Calculations*, Phys. Rev. Lett. **86**, no. 20, 4556–4559 (2000).

[110] N. Roberts and R. Needs, Surf. Sci. **236**, 112 (1990).

[111] M. Rohlfing, P. Krüger, and J. Pollmann, *Quasiparticle band-structure calculations for C Si Ge GaAs and SiC usind Gaussian-orbital basis set*, Phys. Rev. B **48**, no. 24, 17791–17805 (1993).

[112] M. Rohlfing, P. Krüger, and J. Pollmann, *Efficient scheme for GW quasiparticle band-structure calculations with applications to bulk Si and to the Si(001)-(2×1) surface*, Phys. Rev. B **52**, no. 3, 1905–1917 (1995).

[113] M. Rohlfing, P. Krüger, and J. Pollmann, *Metallic nature of the symmetric dimer model of Si(001)-(2×1)*, Phys. Rev. B **52**, 13753–13756 (1995).

[114] J. E. Rowe and H. Ibach, *Surface and Bulk Contributions to Ultraviolet Photoemission Spectra of Silicon*, Phys. Rev. Lett. **32**, no. 8, 421–424 (1974).

[115] R.Stumpf and M. Scheffler, Computer Phys. Commun. **79**, 447 (1994).

[116] H. Rücker, M. Methfessel, E. Bugiel, and H. J. Osten, *Strain-stabilized highly concentrated pseudomorphic $Si_{1-x}C_x$ layers in Si*, Phys. Rev. Lett. **72**, 3578 (1994).

[117] R. E. Schlier and H. E. Farnsworth, *Low-Energy electron diffraction studies of cleaned and gas-covered Germanium (100) surfaces*, Semiconductor Surface Physics (R. H. Kingston, ed.), University of Pennsylvania Press, Philadelphia, 1957, pp. 3–21.

[118] R. E. Schlier and H. E. Farnsworth, *Structure and Adsorption Characteristics of Clean Surfaces of Germanium and Silicon*, J. Chem. Phys **30**, 917–926 (1959).

[119] L. J. Sham and M. Schlütter, *Density-functional theory of the band gap*, Phys. Rev. B **32**, 3883–3889 (1989).

[120] D. Shanno and K.-H. Phua, Math. Program. **14**, 149 (1978).

[121] M. L. Shek, *Observations regarding a* $c(4\times4)$ *C-Si(100) surface*, Surf. Sci **414**, 353–362 (1998).

[122] A. I. Shkrebtii, R. D. Felice, C. M. Bertoni, and R. D. Sole, *Ab initio study of structure and dynamics of the Si(100) surface*, Phys. Rev. B **51**, 11201 (1995).

[123] J. Shoemaker, L. W. Burggraf, and M. S. Gordon, *An ab initio cluster study of the structure of the Si(001) surface*, J. Chem. Phys **112**, 2994 (2000).

[124] S. Strite, J. Ruan, Z. Li, A. Salvador, H. Chen, D. J. Smith, W. J. Choyke, and H. Morkos, *An investigation of the properties of cubic GaN grown on GaAs by plasma-assisted molecular-beam epitaxy*, J. Vac. Sci. Technol. B **9**, 1924–1929 (1991).

[125] S. M. Sze, *Semiconductor devices: Physics and Technology*, John Wiley & Sons, New York, 1985.

[126] M. Takahasi, S. Nakatani, Y. Ito, T. Takahashi, X. W. Zhang, and M. Ando, *Surface X-ray diffraction study on the Si(001) 2×1 structure*, Surf. Sci **338**, L846–L850 (1995).

[127] T. Takaoka, T. Takagaki, Y. Igari, and I. Kusunoki, *Observation of* $c(4\times4)$ *LEED pattern induced by reaction of Si(100) surface with* C_2H_4, Surf. Sci. **347**, 105–110 (1996).

[128] J. Tersoff, *Modeling solid-state chemistry: Interatomic potentials for multicomponent systems*, Phys. Rev. B **39**, 5566–5568 (1989).

[129] J. Tersoff, *Enhanced Solubility of Impurities and Enhanced Diffusion near Crystal Surfaces*, Phys. Rev. Lett. **74**, 5080–5083 (1995).

[130] J. Tersoff and D. R. Hamann, *Theory of the scanning tunneling microscope*, Phys. Rev. B **31**, 805 (1985).

[131] J. M. Thijssen, *Computational Physics*, Cambridge University Press, Cambridge, 1999.

[132] H. Tochihara, T. Amakusa, and M. Iwatsuki, *Low-temperature scanning-tunneling-microscopy observations of the Si(001) surface with a low surface-defect density*, Phys. Rev. B **50**, 12262–12265 (1994).

[133] R. M. Tromp, R. J. Hamers, and J. E. Demuth, *Si(001) Dimer structure observed with scanning tunneling microscopy*, Phys. Rev. Lett. **55**, 1303 (1985).

[134] N. Troullier and J. L. Martins, *Efficient pseudopotentials for plane-wave calculations*, Phys. Rev. B **43**, 1993 (1991).

[135] D. Vanderbilt, *Soft self-consistent pseudopotentials in a generalized eigenvalue formalism*, Phys. Rev. B **41**, 7892–7895 (1990).

[136] D. Vanderbilt and S. G. Louie, *Total energies of diamond (111) surface reconstructions by a linear combination of atomic orbitals method*, Phys. Rev. B **30**, no. 10, 6118–6130 (1984).

[137] J. A. Venables, *Introduction to Surface and Thin Film Processes*, Cambridge University Press, Cambridge, 2000.

[138] U. V. Waghmare, H. Kim, I. J. Park, N. Modine, P. Maragakis, and E. Kaxiras, *HARES: an efficient method for first-principles electronic structure calculations of complex systems*, Comp. Phys. Comm. **137**, 341–360 (2001).

[139] J. Wang, T. A. Arias, and J. D. Joannopoulos, *Dimer vacancies and dimer-vacancy complexes on the Si(100) surface*, Phys. Rev. B **47**, 10497–10508 (1993).

[140] R. A. Wolkow, *Direct observation of an increase in buckled dimers on Si(001) at low temperature*, Phys. Rev. Lett **68**, 2636 (1992).

[141] N. Wooster, *Crystal Structure of Molybdenum Trioxide*, Nature **127**, no. 3194, 93 (1931).

[142] R. W. G. Wyckoff, *Crystal structures*, 2nd ed., Interscience Publishers, New York, 1963.

[143] W. S. Yang, F. Jona, and P. M. Marcus, *Atomic structure of Si{001} 2×1*, Phys. Rev. B **28**, 2049 (1983).

[144] H. C. Yao, W. G. Rothschild, and H. S. Gandhi, Stud. Surf. Sci. Catal. **71**, (1984).

[145] X. Yin, H. Han, and A. Miyamoto, *Structure and adsorption properties of* MoO_3*: insights from periodic density functional calculations*, J. Mol. Model. **7**, 207–215 (2001).

[146] T. Yokoyama and K. Takayanagi, *Anomalous flipping motions of buckled dimers on the Si(001) surface at 5 K*, Phys. Rev. B **61**, R5078–R5081 (2000).

[147] X. Zhu and S. Louie, *Quasiparticle bandstructure of thirteen semiconductors and insulators*, Phys. Rev. B **43**, no. 17, 14142–14156 (1991).